ION DESORPTION, DETECTION & DISSOCIATION IN TIME-OF-FLIGHT MASS SPECTROMETRY

by

GARRETT R. WESTMACOTT

A Thesis
Submitted to the Faculty of Graduate Studies
In Partial Fulfilment of the Requirements
for the Degree of

DOCTOR OF PHILOSOPHY

Department of Physics and Astronomy
University of Manitoba
Winnipeg, Manitoba, CANADA

National Library
of Canada

Acquisitions and
Bibliographic Services

395 Wellington Street
Ottawa ON K1A 0N4
Canada

Bibliothèque nationale
du Canada

Acquisitions et
services bibliographiques

395, rue Wellington
Ottawa ON K1A 0N4
Canada

Your file Votre référence

Our file Notre référence

0-612-32035-9

Canada

THE UNIVERSITY OF MANITOBA

FACULTY OF GRADUATE STUDIES

*****

COPYRIGHT PERMISSION PAGE

ION DESORPTION, DETECTION & DISSOCIATION IN TIME-OF-FLIGHT MASS SPECTROMETRY

BY

GARRETT R. WESTMACOTT

A Thesis/Practicum submitted to the Faculty of Graduate Studies of The University of Manitoba in partial fulfillment of the requirements of the degree of

DOCTOR OF PHILOSOPHY

ACKNOWLEDGMENTS

I would like to thank my advisor, Dr. Werner Ens, for guiding the research projects described in this thesis, and for his valuable advice and instruction in the experiments. I would also like to thank Dr. Ken Standing for his overall guidance and support. Both Dr. Werner Ens and Dr. Ken Standing have taught me many of the subtleties of doing research, and, more importantly, have shown me that science research extends beyond the lab work. It has been a privilege and a pleasure working with them.

Dr. Hélène Perrault and Dr. George Tabisz, also on my advisory committee, have both been helpful with their constructive comments and suggestions regarding my research and thesis.

I am grateful to John Martens and Anatoli Verentchikov who helped me with my research in the beginning, and to Nancy Poppe-Schreimer who offered lots of helpful guidance during my early years in the lab. I also acknowledge Igor Chernushevich, Jie Zhou, Alexandre Loboda, Meciej Bromirski and Marek Znamirowski for all their suggestions and comments.

I thank my colleagues Andrew Krutchinsky, Ragnar Dworschak and Mark McComb who, in their own unique and distinctly different ways, added to my educational experience and the enjoyment of a long period of study.

Victor Spicer deserves a special thanks for all the valuable help he has given me over the past six years. If something breaks, he helps fix it. If parts are needed, he helps build or find them. If a recipe for a dinner date is required, he always has interesting suggestions.

Also, I am grateful to Gilles Roy who has taught me, that in the frustrations of working with equipment, to "Relax!" More importantly, he taught me to always ask questions and never be embarrassed to say, "I don't get it!" I have learned more about physics research from him than I could have ever learned in the classroom. He has also graciously loaned me a lot of equipment over the years.

Finally and most importantly, I want to acknowledge my parents Rod and Carolyn (also known as Dad and Mom). This work is as much their achievement as it is mine because it is their unconditional love and support that made it all possible. I have spent a mere six years working on this thesis but they have spent 28 years as my parents and there is no degree or title high enough that could honour them. All I can say to them is, "Thank you, and I love and respect you both very much." If anything, this thesis testifies to my parents' success at being great and loving parents. I dedicate this thesis to them.

ABSTRACT

The results of several fundamental experiments on desorption/ionization and fragmentation in time-of-flight mass spectrometry are described.

The yield of desorption of secondary molecular ions of valine was determined as a function of primary ion mass with a tandem time-of-flight mass spectrometer. The primary ions consisted of alkali metals Li^+, Na^+, K^+, Rb^+ and Cs^+ with impact energy on the valine target ranging between 3.5 and 10keV. The yield measurements for both negative and positive molecular valine ions were found to correspond to the cube of nuclear stopping power, and low mass ions, like H^- and C^- were found to scale linearly with the nuclear stopping power.

Secondary-ion and secondary-electron emission yields from surfaces bombarded with large molecular ions were measured in a tandem time-of-flight mass spectrometer. The primary ions were produced by matrix-assisted laser desorption/ionization and ranged in mass from 6000u to 110 000u, and in energy from 5 to 25keV. The yields were measured for surfaces of stainless steel and CsI. For a given energy, the secondary electron yield decreases rapidly for increasing mass but remains greater than ~10%; in contrast, the efficiency of secondary ion production remains close to unity. For high velocities, the electron yield is significantly higher for the CsI surface, but for velocities corresponding to less than ~0.4eV/u, the emission is rather insensitive to the surface.

An alternative method for the analysis of metastable-ions in a reflecting time-of-flight instrument is demonstrated. Post-source decay analysis usually involves collecting fragment ion spectra in segments, decreasing the mirror voltage for each segment. The present method leaves the mirror voltage fixed and increases the accelerating voltage to acquire each segment. The central advantage is that the mass calibration depends sensitively on the mirror voltage but only weakly on the accelerating voltage. The method of post source decay analysis is also demonstrated with precursor ion selection using a Bradbury-Nielsen ion gate.

Finally, the forth experiment involves measuring molecular ion yields as a function of laser fluence for matrix-assisted laser desorption/ionization. This experiment was done on two different instruments. One is a linear time-of-flight mass spectrometer where both analog and pulse-counting detection methods are used and compared. The second instrument is an orthogonal-injection time-of-flight instrument with collisional cooling and pulse-counting detection. It is an improvement relative to the linear instrument because it ensures single-ion counting. The results for both instruments and detection methods were consistent. The ion yield versus laser fluence was found to have a steep slope on a log-log plot (between 6 and 9) for a range of fluence covering almost an order of magnitude. Also no evidence was oberved for an ion desorption threshold at low laser fluence ($\sim 10 J/m^2$).

TABLE OF CONTENTS

CHAPTER 1

IN THE BEGINNING

A Brief Introduction to Desorption/Ionization Methods used in Mass Spectrometry

Almost a hundred years ago, J. J. Thomson built the first mass spectrometer [1] and was able to separate the isotopes of neon, masses 20 and 22, using a magnetic field. About 30 years after Thomson, around 1940, with the introduction of electron impact ionization (EI) [2,3] of gas samples, mass spectrometry had evolved to give well-defined and reproducible mass spectra of complex mixtures of hydrocarbons. From this time, up until the present, one general goal in the development of organic mass spectrometry (MS) has been to investigate ions of larger and larger mass. The requirement of volatilization of samples for such ionization methods as EI causes problems when the sample molecules are involatile or thermolabile, that is, the temperature at which they evaporate is higher than that at which they decompose. Organic compounds are too involatile either because their molecular mass is too large or because they are highly polar, as is the case for peptides and proteins.

One of the most successful methods to produce large molecular ions is by bombarding a solid surface, covered with organic molecules, with ions or photons. The story of the development of desorption/ionization methods for large involatile organic molecules really begins with particle induced desorption. The application of particle bombardment to produce molecular ions from nonvolatile organic material (directly from the condensed phase) was first reported in 1974 by Macfarlane and Torgerson [4,5] using fission fragments from ^{252}Cf, that is, using high-energy particles of mass ~100u and energy of ~100MeV. Early experiments produced molecular ions desorbed from bulk samples of

biomolecules with molecular mass close to 2000u [6]. The technique was named plasma desorption mass spectrometry (PDMS) because of the plasma associated with a fission fragment as it interacts with matter.

Over the next ten years, the mass range was extended and resolution improved in PDMS by depositing the samples on various type of substrates. In 1984 molecular ions of mass greater than 20 000u were observed with a conducting target foil [7], and by 1989, Jonsson *et al* [8] had dramatically improved the mass spectra and mass range using proteins absorbed onto the polymer substrate nitrocellulose. Subsequently, intact molecular ions have been desorbed up to about 45 000u in mass.

Production of ions by fission fragment bombardment couples naturally with time-of-flight mass spectrometry (TOF-MS). Since the introduction of the TOF principle for mass separation of a pulsed ion packet in 1946 [9], the use TOF mass spectrometry has been limited by relatively poor resolution in comparison to other mass spectrometers like, for example, sector instruments. However PDMS avoids two of the problems previously associated with the limited resolution of TOF-MS. Firstly, from the fission process, one of the recoiling fragments may be used to give a well defined start signal (start time), with the acceleration field of the TOF-MS instrument at a high, stable DC potential, instead of being pulsed. Secondly, the ions are ejected from a solid equipotential surface; thus the energy and spatial spread is much smaller than for traditional gaseous ion sources.

Soon after the discovery of PDMS, another form of particle-induced desorption using low energy ion bombardment emerged; this is most relevant to Chapter 2 of this thesis. The use of low-energy ion bombardment for desorption of organic molecules was pioneered by Benninghoven in 1976 [10] and was regarded as an unexpected development of static secondary ion mass spectrometry (SIMS) where primary ion impact energies are around a few keV with low ion currents ($\sim$nA/cm^2). The low primary ion currents, in turn, produced low secondary ion currents which decreases even further for increasing sizes of molecular ions. Thus, Benninghoven, using a sector-field instrument, was limited in mass range to biomolecules of a few hundred u because of the transmission losses and losses due to scanning the mass spectrum.

An increase in the observable mass range of SIMS was achieved by coupling

SIMS to a TOF instrument, taking advantage of the high sensitivity and mass range of TOF-MS, as had been demonstrated with PDMS. In 1981 Chait and Standing [11] developed a low-energy pulsed ion gun with 5keV Cs+ ions which induced desorption of molecular ions of mass around 1300u [12]. The highest mass polypeptide observed with this technique, using nitrocellulose as a substrate, is about 14 000u [13].

In 1982, an increase in the observable mass range in SIMS was also finally achieved on sector-field instruments by using samples dissolved in a viscous liquid like glycerol [14], and using primary ion currents typical of dynamic SIMS (currents greater than $\sim 10^{-5}$ A/cm^2), and orders of magnitude higher than in static SIMS. Because the beam consisted of neutral particles [15,16], this technique was named fast atom bombardment (FAB). It is well suited for coupling to existing sector-field and quadrupole spectrometers because of the neutral primary beam and because it provides sustainable secondary ion currents by the renewal of the liquid matrix surface. Typically FAB analysis is used up to a mass-range of a few thousand u [17,18].

The final desorption method to be discussed, and which is most relevant to this thesis, involves using a pulsed laser beam as opposed to particle bombardment. In 1976, the use of nanosecond pulsed laser, together with TOF-MS, was first used to study biological material [19]. The early work on laser desorption mass spectrometry (LDMS) was reviewed in detail by Conzemius and Capellen in 1980 [20] and more recent laser desorption work has been reviewed by Hillenkamp in 1983 and 1985 [21,22].

For about ten years following this development, the application of laser desorption (LD) to biomolecules was restricted to molecules that absorbed light at the wavelength of the laser, thus limiting sample masses to below ~1000u [23]. However, in 1988, Karas and Hillenkamp found that by mixing the analyte with a suitable organic matrix (the first being nicotinic acid), and then illuminating the dried mixture with a laser pulse it is possible to produce intact molecular ions of heavy (~66 000u) and nonvolatile proteins [24,25]. Up to the present time, this method has rapidly grown with the discovery of new matrices [26,27], extending the method to other classes of samples (for example, glycopeptides, carbohydrates and nucleotides), with masses up around 300 000u [28] routinely being analysed. This technique is referred to as matrix-assisted laser-desorption/ionization, or

MALDI.

At about the same time that MALDI was introduced, another method of producing gas-phase ions from large molecules was developed. In electrospray ionization "ESI" gas-phase ions are produced in atmosphere directly from solution by an electric field applied at the tip of a capillary. The ions are introduced to the mass spectrometer through a small orifice or a capillary separated from vacuum by a few stages of differential pumping. In contrast to MALDI, in which low charge states are produced (typically < 3) ESI produces a distribution of highly charged molecular ions with an average of one positive charge per kDa for denatured proteins. Compared to MALDI, ESI is more sensitive to contaminants and produces more complex spectra. On the other hand, since a mass spectrometer measures the ratio m/z, a modest m/z-range quadrupole mass filter, well-suited to a continuous ion source, can be used to measure large proteins. ESI is mentioned for completeness but the experiments described here do not involve this ionization technique directly.

These latter two ionization methods (MALDI and ESI) have revolutionized mass spectrometry of large molecules. These methods have increased the mass range for some classes of compound (notably proteins) into the range of several hundred u, making mass spectrometry a realistic alternative to chemical methods of molecular weight determination such as gel electropheresis.

CHAPTER 2

STOPPING POWER

Desorption of Organic Ions by Low Energy Ion Bombardment; Is it Caused by Nuclear or Electronic Stopping?

2.1 Introduction

The surprising observation that large intact molecular ions can be ejected from labile organic material by bombardment with energetic particles led to a dramatic increase in the mass range accessible to analytical mass spectrometry. Particle bombardment in two distinctly different energy ranges has been routinely used to produce ions for mass spectral analysis. The bombarding particles may have energy in the ~100MeV range (PDMS) or in the ~10keV range (SIMS and FAB). An extensive review of experimental investigations into the fundamentals of the desorption of thermally labile molecular ions by low-energy (~keV) particle bombardment of organic solids or liquids, with some comparisons to high-energy bombardment is available [1]. Although MALDI and electrospray ionization have now largely replaced particle bombardment for mass spectrometry of biomolecules, the study of desorption phenomena has relevance to the general study of interactions of particle beams with matter. Moreover, the use of clusters of large molecules as bombarding particles in plasma induced desorption has shown considerably promising results.

When measuring effects of primary ion characteristics on secondary ion yields, the stopping power (dE/dx), the energy loss per travelled path length, is an obvious parameter

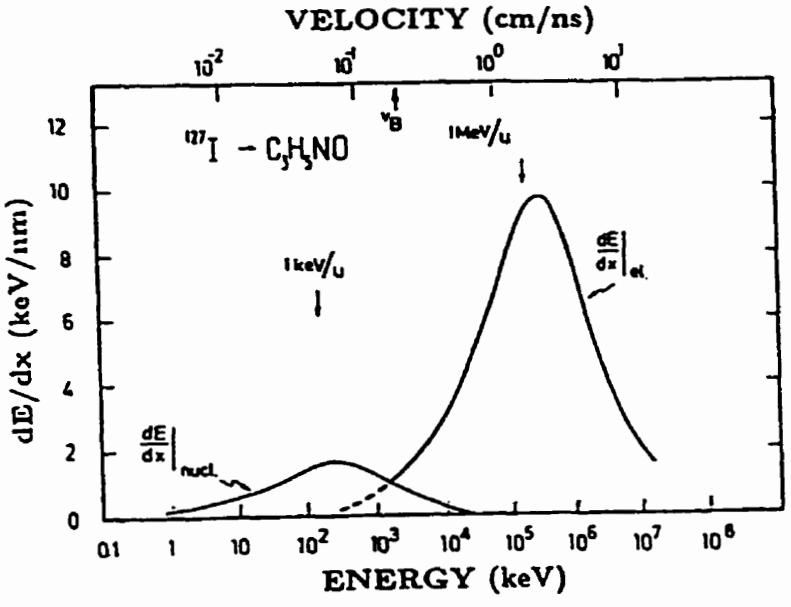

Figure 2-1: Nuclear and electronic stopping powers for ^{127}I ions incident on a protein model solid C_3H_5NO with density 1 g/cm^3 [2].

to consider since it directly depends on both mass and energy of the projectile. The stopping power, shown as a function of incident energy in Figure 2-1, has two components, *nuclear stopping* (elastic collisions with target atoms), and *electronic stopping* (energy transfer to the atomic electrons). For high energy projectiles, above the Bohr velocity ($v_B = 0.22$cm/ns, the velocity of an electron in its ground state in a hydrogen atom), the energy loss in the target occurs predominantly by electronic stopping (inelastic ion-electron collisions). For low energy projectiles, below the Bohr velocity v_B, the energy loss is predominantly by nuclear stopping. In this regime, the incident particle has a velocity lower than typical valence electron velocities in the solid and thus the electrons have time to adjust their orbitals resulting in elastic collisions between the screened atomic nuclei.

Figure 2-2 shows sample spectra of leucine enkephalin (555u), bovine insulin (5733u) and PSP (pancreatic spaholytic peptide, 11711u) produced by high- and low-energy ion bombardment [1,3]. The mass spectra for the two bombarding energies were

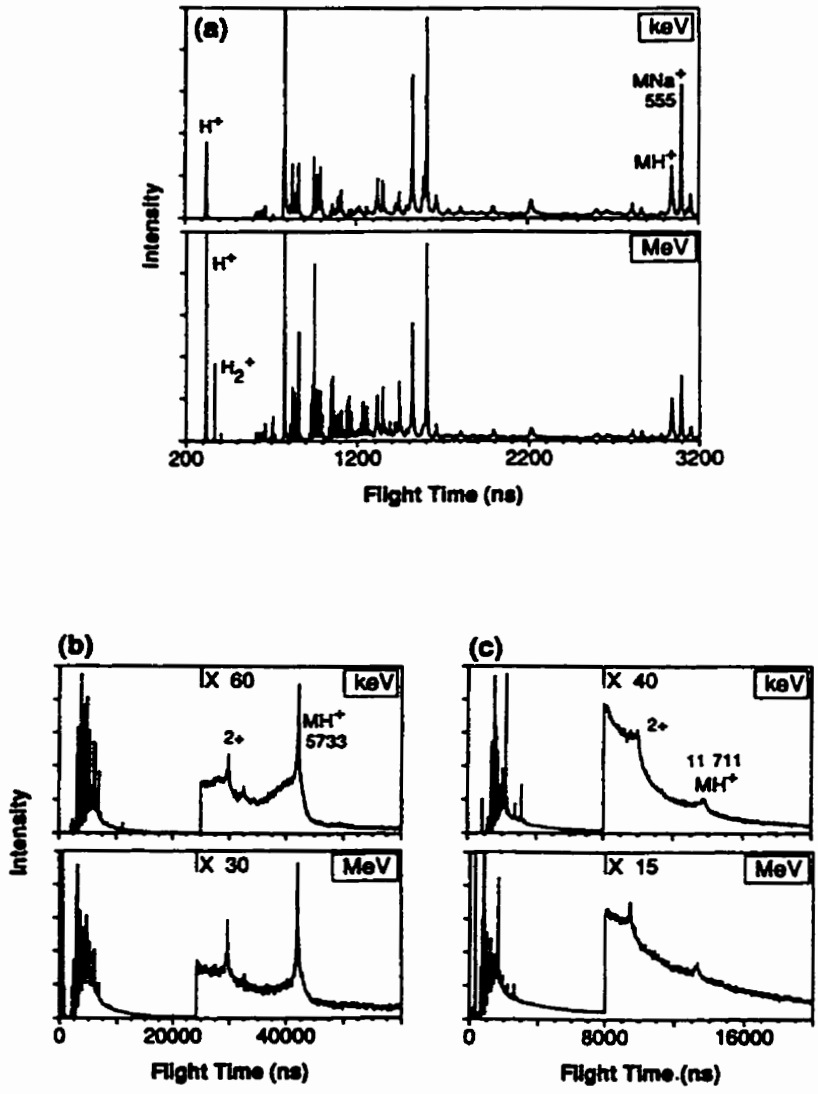

Figure 2-2: Positive ion TOF mass spectra of (a) leucine enkephalin (555u), (b) bovine insulin (5733u) and (c) PSP (11711u). The keV spectra were produced by 18keV Cs^+ ion bombardment and the MeV, ^{252}Cf fission fragment bombardment. The spectra were acquired in the same spectrometer from the same target, without interrupting the vacuum between measurements [3].

acquired in the same linear time-of-flight (TOF) mass spectrometer using the same target without interrupting the vacuum between measurements. The main feature to note in the spectra is the similarity of the relative intensities of the sample related ions desorbed by the two bombarding energies; even the background (from metastable decay of the molecular ion) is almost identical in Figure 2-2b and c. The similarity is remarkable considering that the primary projectiles lose energy by two distinctly different mechanisms, nuclear or electronic stopping, as shown Figure 2-1.

It is well established that for high-energy particle bombardment, the electronic stopping power is responsible for the observed molecular ion desorption [1,4]. At low-energy particle bombardment, although the *energy loss* is predominantly by nuclear stopping, it is not yet clearly established whether it is the nuclear or electronic stopping mechanism that is responsible for the *desorption* of molecular ions. The remarkable similarity of the spectra produced by the two bombarding energies shown in Figure 2-2 suggest that the low-energy tail of the electronic stopping power may also be responsible for the desorption of the molecular ion by keV particle bombardment.

In contrast to the similarity of the spectra for the molecular ions produced by the two bombarding energies shown in Figure 2-2, Figure 2-3 shows a pronounced contrast in the relative intensity of atomic ions like H^-, C^-, O^- and F^- which are characteristic of nuclear sputtering compared to more complex ions like CN^- and the peak at mass 42u (probably CNO^-) which are associated with electronic sputtering as well [5].

Systematic molecular ion yield measurements for low energy ion bombardment are scarce. For keV ion bombardment, Standing *et al* at Manitoba measured the molecular ion yield, $[M+H]^+$, of alanine as a function of primary ion impact energy [6]. The primary ions were positive alkali ions with impact energies ranging between 1 and 14keV. Their results, re-plotted in [1], are shown in Figure 2-4. The authors concluded, based on the strong mass dependence, that the nuclear stopping is mainly responsible for desorption of the molecular ion (except for the primary ion Li^+ where both the nuclear and electronic stopping appear to contribute).

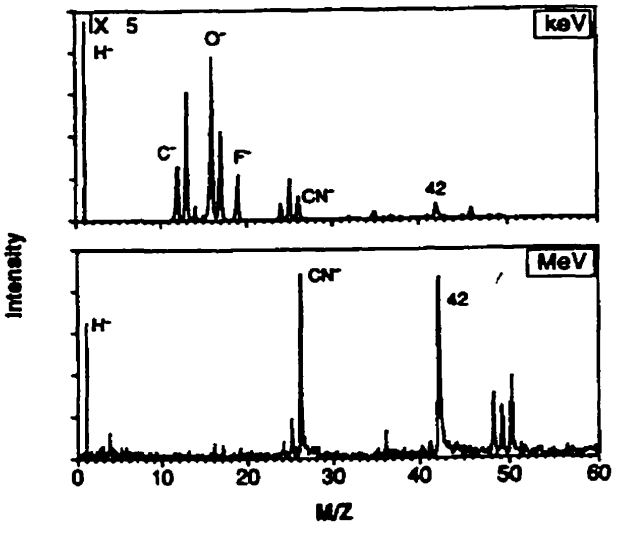

Figure 2-3: The low-mass range of negative ions TOF mass spectra of leucine enkephalin obtained with 18keV Cs+ bombardment (upper) and with fission fragments (lower) [3].

Also in 1982 Albers *et al* [7] measured yields of $[M+H]^+$ ions from a valine target as a function of the velocity of the primary ^{16}O and ^{32}S ions, as shown in Figure 2-5, which were obtained with a slightly higher range of primary-ion velocity than used by the Manitoba group. Their results indicate that the nuclear stopping is more effective for desorption even when its magnitude is smaller than that of the electronic stopping.

More recently, Hunt *et al* [5] performed a similar experiment using negative valine molecular ions desorbed from Xe^+, Kr^+ and Ar^+ ion bombardment in a similar velocity region as Albers experiment, with energy ranging between 400keV and 3.5MeV. In this velocity domain, the nuclear and electronic stopping have approximately the same magnitude but opposite slopes. Their results, shown in Figure 2-6, provide convincing evidence that in this energy range, electronic stopping is mainly responsible for the desorption of negative molecular ions of valine, this seems to be in direct contrast to the results of Albers *et al* [7] and also seems to contradict the results of Standing *et al* [6].

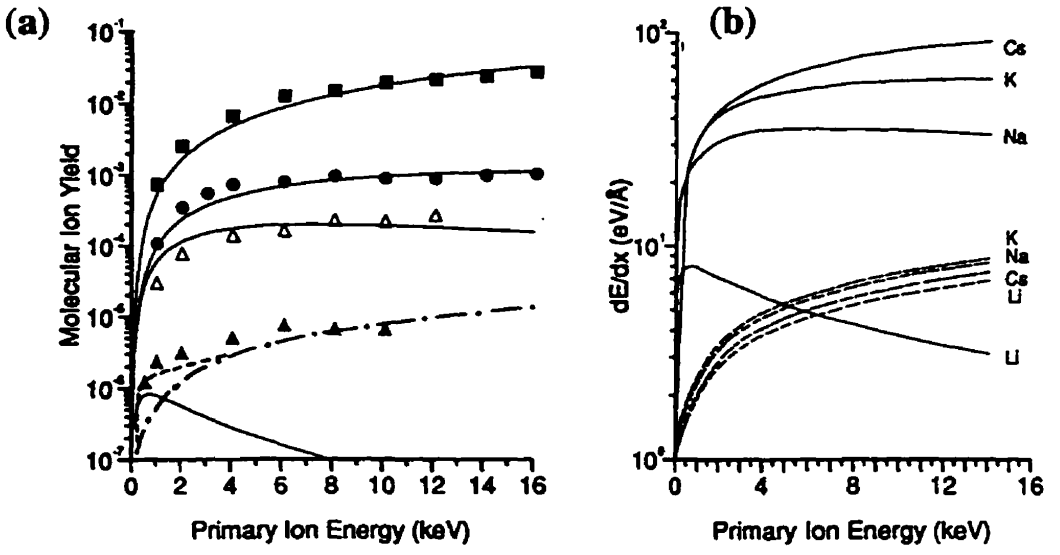

Figure 2-4: (a) Yields of $[M+H]^+$ secondary ions from alanine produced by Cs+ (■), K+ (●), Na+ (Δ), and Li+ (▲) primary ions [1,6]. The solid curves in (a) are proportional to $(dE/dx)_n^3$ with separate normalization for each projectile. The dot-dashed curve is proportional to $(dE/dx)_e^2$ for Li and the dashed curve is a linear combination of $(dE/dx)_n^3$ and $(dE/dx)_e^2$. (b) Calculations of the nuclear (solid curves) and electronic (dashed curves) stopping powers.

However, as suggested in [1], the stopping power (either nuclear or electronic) may not be the only (or even the main) parameter that determines the yield of molecular ions, and the dependence may well be different at substantially different velocities. The stopping power contribution to the desorption of the molecular ions for the two different experiments [5,6] are not necessarily inconsistent, as they are in different energy domains and molecular ions of opposite charge were used. Both experiments demonstrated that electronic stopping is more effective for desorption when the magnitude of the nuclear and electronic stopping powers are the same, but the Manitoba results seem to suggest that for SIMS conditions, when nuclear stopping dominates, it is the nuclear stopping that is largely responsible for desorption of the molecular ion. However the Manitoba group had difficulties in normalizing their yield data for different alkali ions, which is rather critical

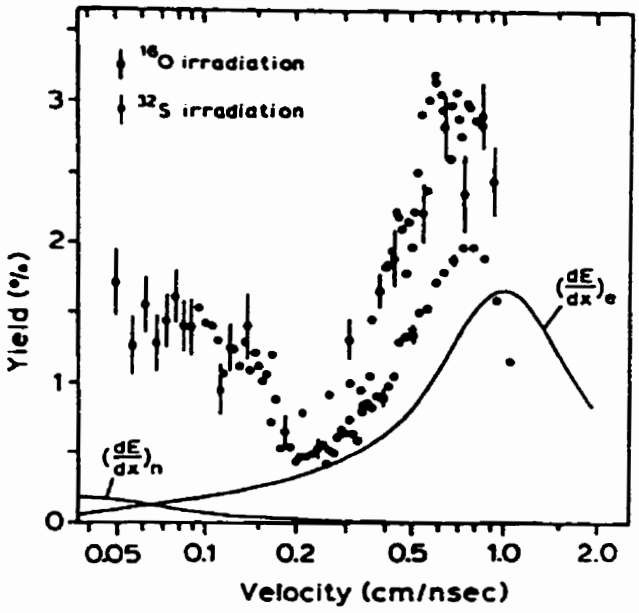

Figure 2-5: Yields of [M+H]+ ions from a valine target as a function of the velocity of the primary 16O and 32S ions. Curves corresponding to the electronic and nuclear stopping powers are also shown [7].

since their conclusion was based on the molecular ion yield dependence as a function of alkali ion mass.

To resolve any possible discrepancies which could arise from the polarity of the molecular ion or the normalization difficulties of previous measurements, this present experiment measures the desorption yield of the negative valine molecular ion as a function of projectile mass for different energies in the region 3-10 keV using an improved method of normalization.

2.2 Experimental

In the present experiment, a tandem time-of-flight mass spectrometer, shown schematically in Figure 2-7a, is used to measure the yield for secondary molecular ions from

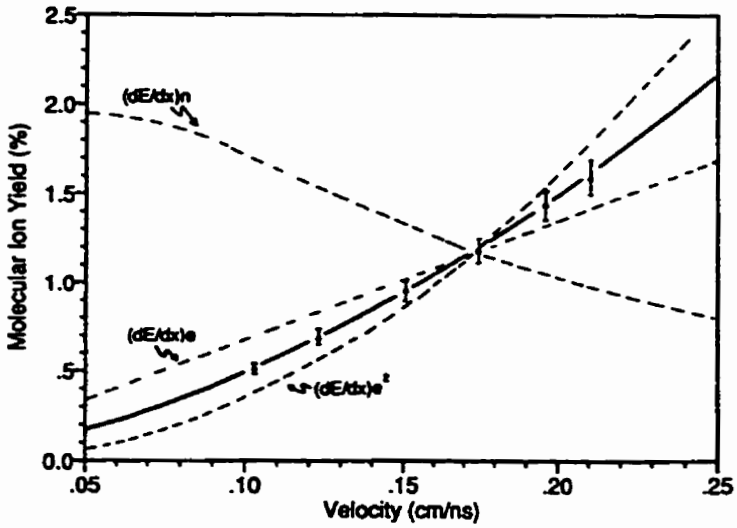

Figure 2-6: Yield of $[M\text{-}H]^-$ ions from valine as a function of the velocity of incident Xe^+ ions. The dashed lines are calculations of $(dE/dx)_n$, $(dE/dx)_e$ and $(dE/dx)_e^2$ arbitrarily normalized to one of the data points [5].

valine as a function of primary ion mass and energy. Primary ions are produced at target 1 (Li^+, Na^+, K^+, Rb^+, and Cs^+) by laser desorption from a high-repetition rate excimer laser (HE-460-HR-B: Lumonics Inc., Kanata, Ontario, Canada). The laser uses XeCl (wavelength 308nm) and is run at 300Hz. It is incident on target 1 at 70° to the normal. The optics set up are similar to that shown in Figure 3-2 on page 40.

The desorbed primary ions are accelerated through a single grounded grid (90% transmission) placed 1cm in front of target 1, then travel down a primary, field-free flight tube (~70cm) to strike target 2, an etched silver annular disc. The beam is collimated by a small iris placed about 5cm in front of the target. The impact energy of the primary ions ranges between 3.5 and 10keV. A small fraction f of the primary alkali ions pass through a small hole in the centre of target 2 (2mm dia.), through two more 90% transmission gounded grids, and, after –2.5kV post-acceleration, are detected in a chevron microchannel plate detector shown in Figure 2-7b. Amplified signals from the microchannel plates

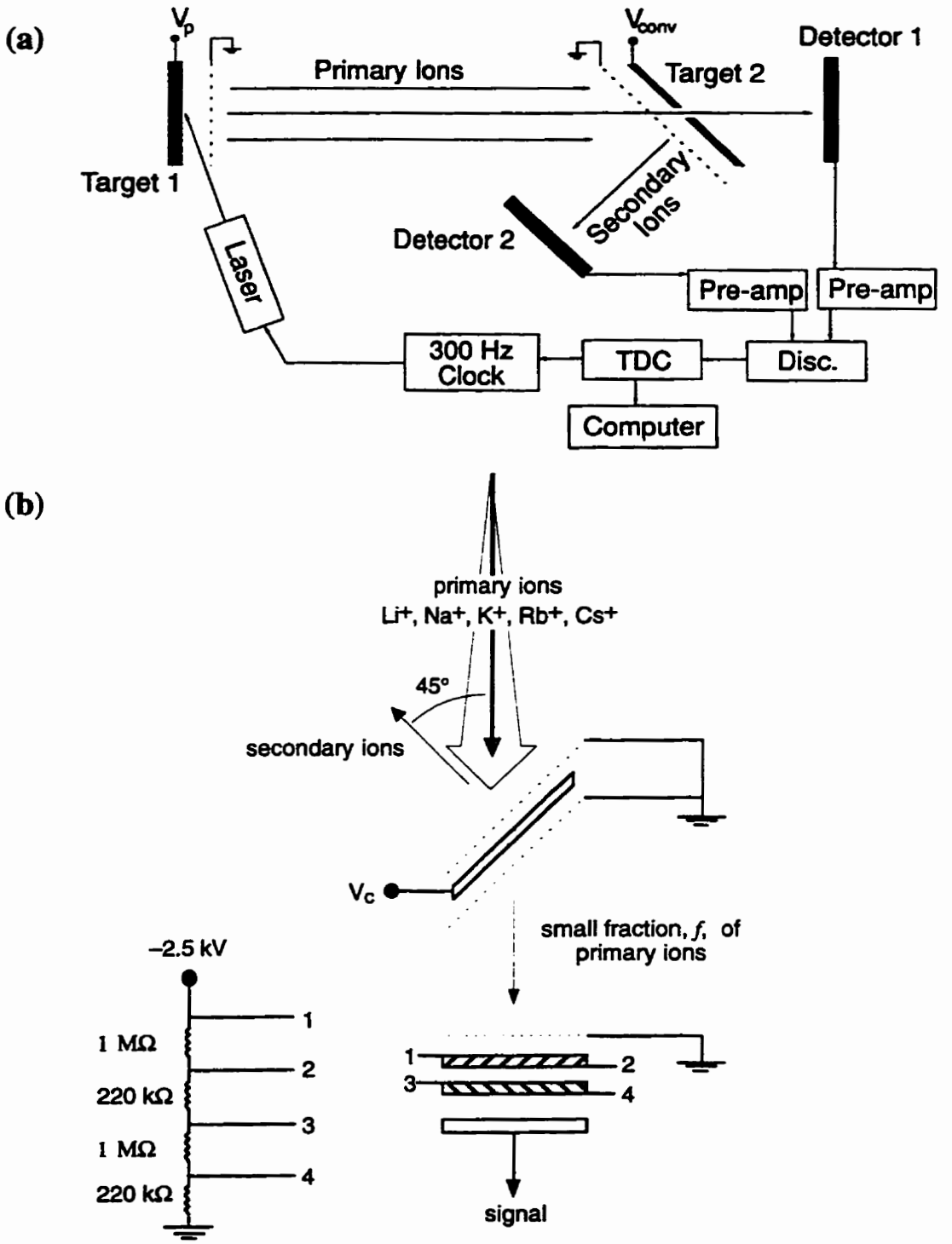

Figure 2-7: (a) Schematic diagram of the experimental arrangement and (b) an enlargement of the target 2 and primary ion detector.

are fed into a 255-stop time-to-digital converter (TDC) (CTN-M2: Institut de Physique Nucléaire, Orsay, France) connected by a custom interface to an Atari TT030 computer for data storage and analysis.

A mixture of alkali ions was deposited onto the target 1 with concentrations such that the primary ion yield for each alkali ion was approximately the same. Secondary ions and electrons produced at the surface of target 2 by the impinging alkali ions are accelerated into another flight tube (~20cm) at 135° to the first. The ions are detected in a 4cm diameter microchannel plate detector, after passing through two more 90% transmission grounded grids. The valine was deposited onto target 2 (~1 cm^2) from 160µl of ~20g/l in water and allowed to air-dry giving about 10^{19} molecules per cm^2.

Sample spectra of the primary ions and secondary ions and electrons are shown in Figure 2-8 with target 2 at –2kV. The secondary ions from the primary alkali ions overlap with each other, so it is necessary to select a single alkali ion with the set of deflection plates. The plates (not shown in Figure 2-7a) are normally at 500V but are pulsed to ground for a few hundred nanoseconds to allow straight passage for the selected alkali ion species, while all other ions (at different velocities and hence times) are deflected away from target 2. The deflection plates are about 22cm in front of target 1, about 3cm long, with about 1cm gap between the plates.

An example of the spectra of negative secondary ions obtained with Cs^+ bombardment is shown in Figure 2-9 (with target 2 at –500V), and of positive secondary ions obtained with K^+ bombardment in Figure 2-10 (with target 2 at +500V). In the secondary ion spectra shown in Figure 2-9 and 2-10, the electrons are removed by placing a large permanent magnet near the second flight tube. This reduces any contributions (extra peaks) from spurious electrons from collisions between the primary ions and other objects like grids or flight tube walls.

The secondary ion yield Y of desorption is defined as the number of secondary ions (of valine, for example) desorbed per incident primary ion. If f is the fraction of primary ions that pass through the small hole in the iris, then the total number of ions that strike

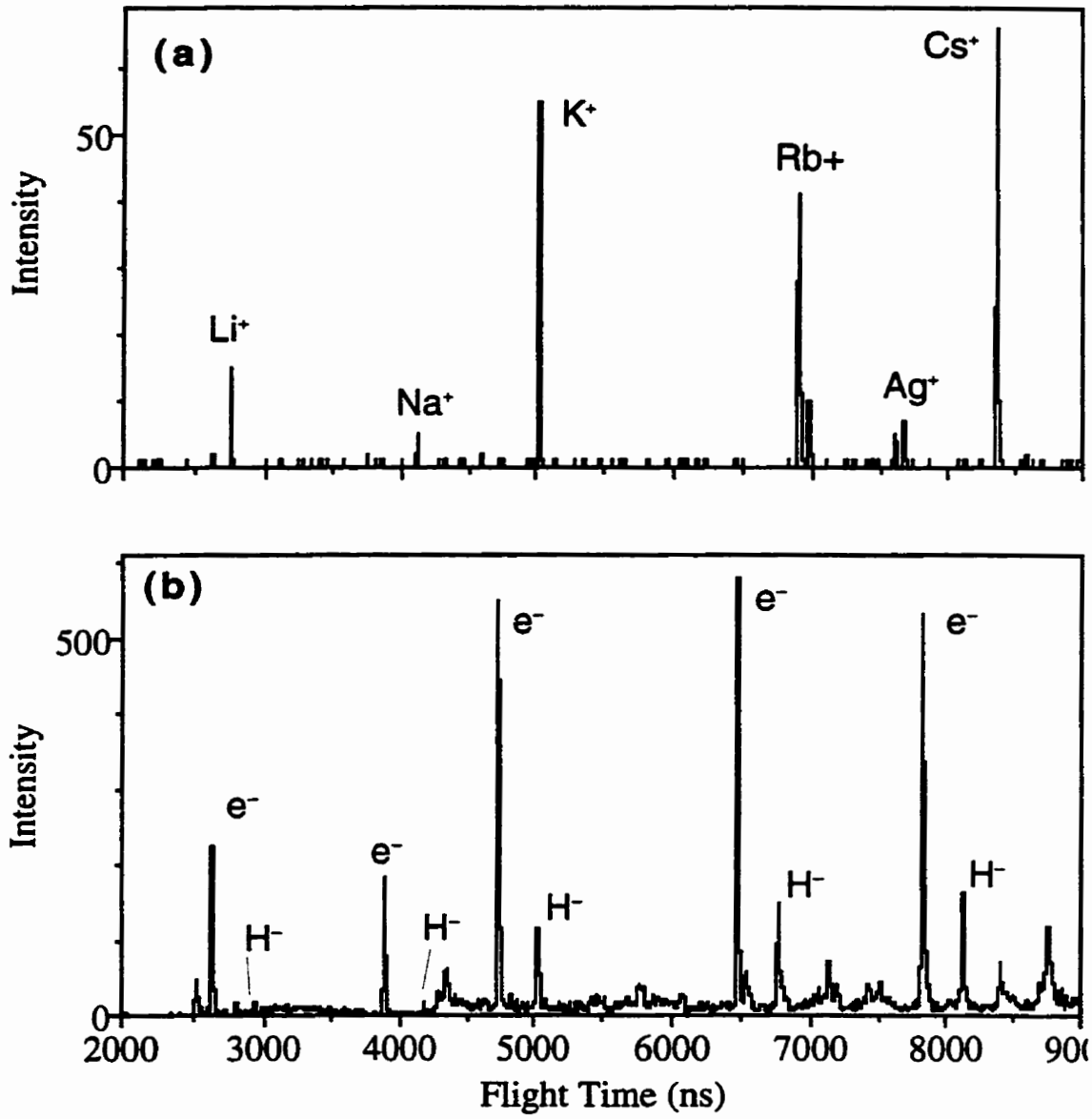

Figure 2-8: Sample spectra with target 1 at accelerating potential 4kV and target 2 at –2kV. (a) Primary ion spectrum (detector 1). (b) Negative secondary ions (detector 2).

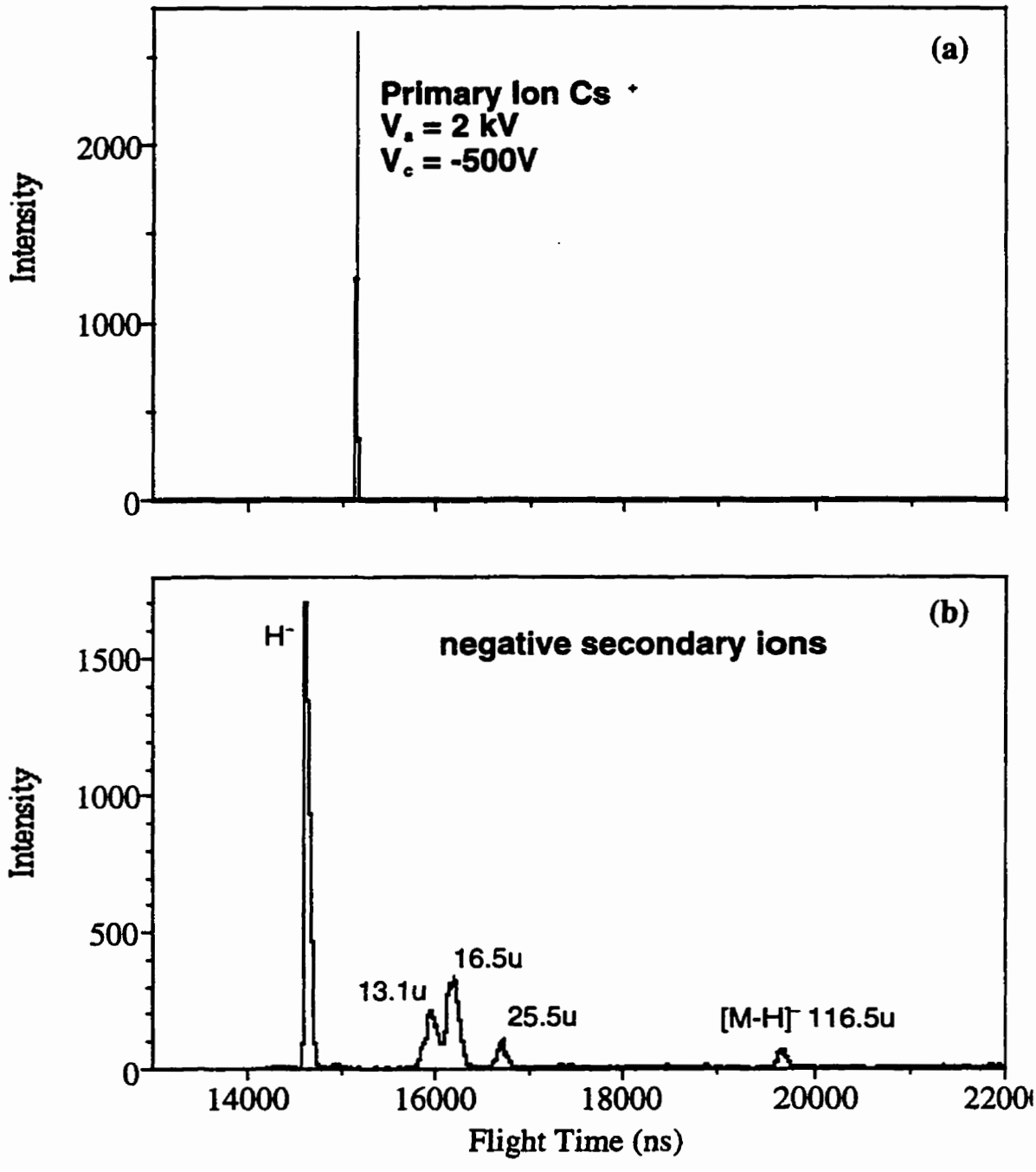

Figure 2-9: (a) Primary ion spectrum of Cs^+ using detector 1. The integrated intensity of the peak gives N_{PI}. (b) Negative secondary ions produced at target 2. Peaks were integrated to obtain N_{SI}.

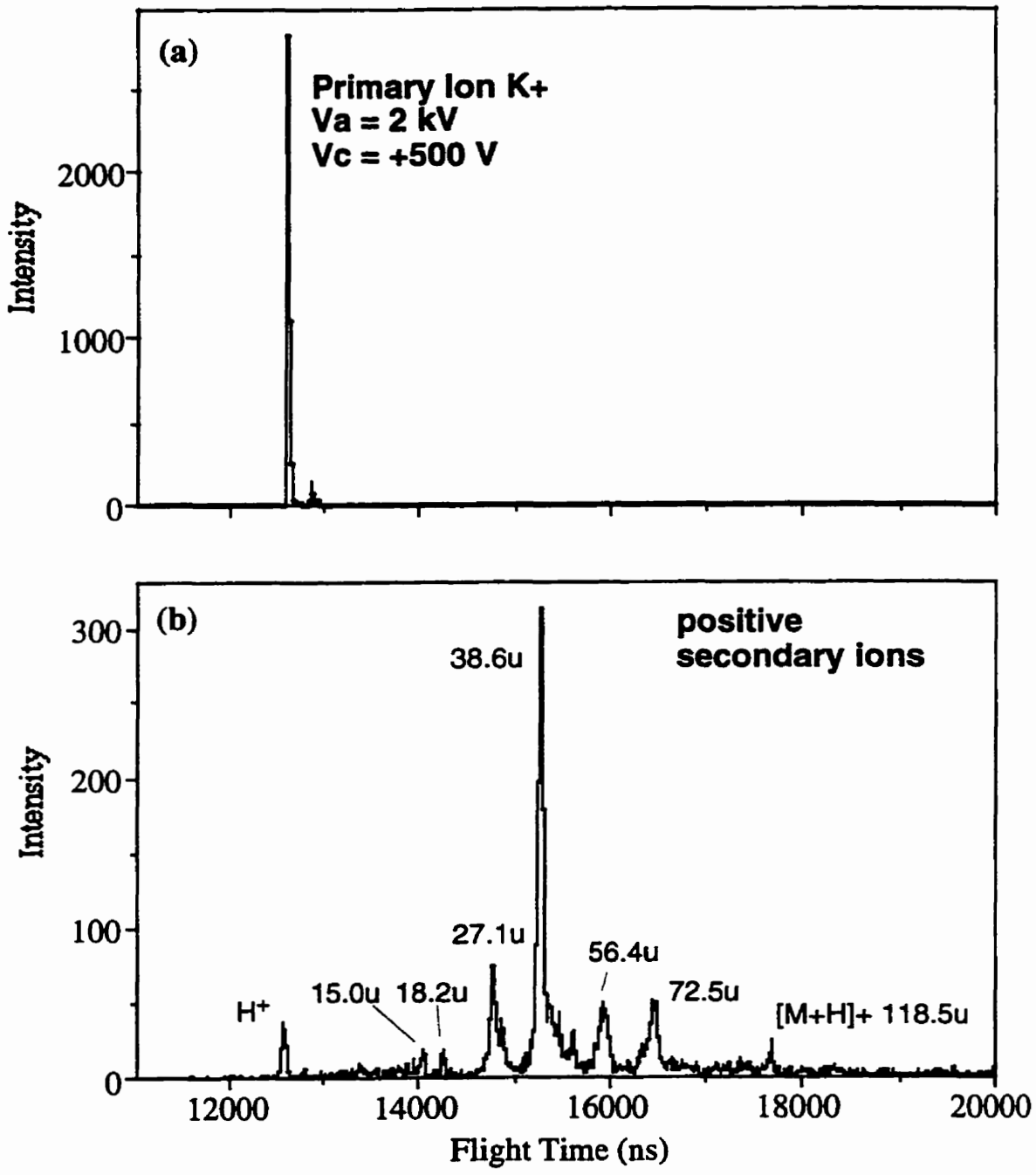

Figure 2-10: (a) Primary ion spectrum of K^+ using detector 1.The integrated intensity of the peak gives N_{PI}. (b) Positive secondary ions produced at target 2. Individual peaks where integrated to obtain N_{SI}

target 2 N_2 is given by

$$N_2 = N_{PI}\left(\frac{1}{f} - 1\right)$$

where N_{PI} is the number of primary ions detected behind target 2 (in detector 1) and N_{PI}/f is the total number of primary ions. Thus, the yield is given by

$$\begin{aligned} Y &= \frac{N_{SI}}{N_2} \\ &= \frac{N_{SI}}{N_{PI}}\left(\frac{f}{1-f}\right) \approx \frac{N_{SI}}{N_{PI}} f \end{aligned} \tag{2-1}$$

where N_{SI} is the number of secondary ions detected in the second flight tube, and $f \ll 1$. It is known that for the energy and primary ion mass range in the experiment, that the electron yield is on the order of one [8]. Thus, the constant of proportionality f was estimated by scaling our measured secondary electron yields to previously measured yields, giving $f = 1/30$. Note that the yields quoted in this work are the absolute yields, though the accuracy is limited by the determination of the constant of proportionality f.

2.3 Stopping Power Calculation

Calculations of the nuclear stopping power for alkali metals incident on valine were made using the Lindhard theory [9] as modified by Wilson et al. [10]. They developed an analytical expression for the nuclear stopping power $(dE/dx)_n$ in terms of a reduced energy ε and a reduced nuclear stopping power $S_n(\varepsilon)$ by using the follow definitions:

$$\left(\frac{dE}{dx}\right)_n = \pi a^2 \gamma N (E/\varepsilon) S_n(\varepsilon) \tag{2-2}$$

for which

$$\varepsilon = \frac{a M_2 E}{k Z_1 Z_2 e^2 (M_1 + M_2)} \tag{2-3}$$

where E is the kinetic energy of the incident projectile, $\gamma = 4M_1M_2/(M_1 + M_2)^2$ is the centre-of-mass transformation unit, $k = 8.99\times10^9 \mathrm{Nm^2/C^2}$ is the Coulomb constant, N is

the atomic density of the target, Z_1 and Z_2 are the atomic numbers of the projectile and target atoms, respectively, M_1 and M_2 are the masses of the projectile and target atoms, respectively, a is a screening length given in terms of the Bohr radius $a_o = 0.529\text{Å}$

$$a = \frac{0.8853 a_o}{(Z_1^{1/2} + Z_2^{1/2})^{2/3}} \tag{2-4}$$

and $S_n(\varepsilon)$ is expressed by

$$S_n(\varepsilon) = \frac{A \ln(B\varepsilon)}{B\varepsilon - (B\varepsilon)^{-C}} \tag{2-5}$$

The constants $A = 0.56258$, $B = 1.1776$ and $C = 0.62680$ were taken from the "average" values quoted in [10]. They determined the constants by fitting Eq. (2-5) to their numerical $S_n(\varepsilon)$ results which came from using an universal interatomic potential function derived from averaging over a representative set of eight neutral atom interactions using free-electron potentials for each.

The electronic stopping power in the velocity region for this experiment ($v < -v_o$, where $v_o \approx 2.2\times10^6\text{m/s}$ is the Bohr velocity), was determined by Lindhard and Scharff [11] to be

$$\left(\frac{dE}{dx}\right)_e = NS_e \tag{2-6}$$

where N is the atomic density and the electronic cross section S_e is given by

$$S_e = Z_1^{1/6} 8\pi k e^2 a_o \left(\frac{Z_1 Z_2}{(Z_1^{2/3} + Z_2^{2/3})^{3/2}}\right)\frac{v}{v_o} \tag{2-7}$$

assuming a Thomas-Fermi model of the atom. The same definitions for the other variables are used as above with the nuclear stopping power.

The total stopping power for valine ($C_5H_{11}NO_2$, atomic weight $A = 117.15\text{u}$) was calculated by adding the contributions from the individual atoms. The density ρ of the sample was assumed to be $1\,\text{g/cm}^3$ and the atomic density N_i of each atomic constituent was calculated by

$$N_i = \left(\frac{\rho}{A} N_a 10^6\right)\left(\frac{n_i A_i}{A}\right) \quad (2\text{-}8)$$

where the first bracketed term is the atomic density N of the target (in atoms/m^3 using Avogadro's constant N_a), n_i is the number of each atomic constituent (e.g., 5 carbon atoms), A_i is the atomic weight each atom and A is the molecular weight of valine. The second term represents the fractional contribution of each atomic constituent, such that

$$N = \sum_i N_i$$

where the summation is over each unique atom (four of them in valine). The computer program used to calculate the total nuclear and electron stopping for valine is given in the Appendix.

2.4 Results and Discussion

All the yield measurements are presented as a function of primary ion mass. The advantage of plotting the yields as a function of mass (instead of energy) is the distinct difference in the mass dependence of the electronic and nuclear stopping power. From Li^+ to Cs^+ the nuclear stopping increases rapidly, whereas the electronic stopping is approximately constant.

The molecular ion yield for valine, both $[M–H]^-$ and $[M+H]^+$, is shown in Figure 2-11. The solid curves are calculated from Eqns. (2-2) and (2-6) with the black line given by $(dE/dx)_n^3/K_n$ and the dashed line, $(dE/dx)_e^2/K_e$, where K_n and K_e are normalization parameters. For small molecules like valine, and for velocities below the maximum in nuclear stopping power, it has been previously shown that the yield scales rather closely with $(dE/dx)_e^2$ [12], which is plotted for comparison purposes. The yield data in Figure 2-11 shows a reasonable fit to $(dE/dx)_n^3/K_n$ which is consistent with previous yield measurements [1] plotted versus bombarding energy. The parameterization of the yields with $(dE/dx)_n^3$ is simply an empirical fit to indicate a correlation. All curves are normalized separately for each energy but the normalizations are all within a factor of ~2

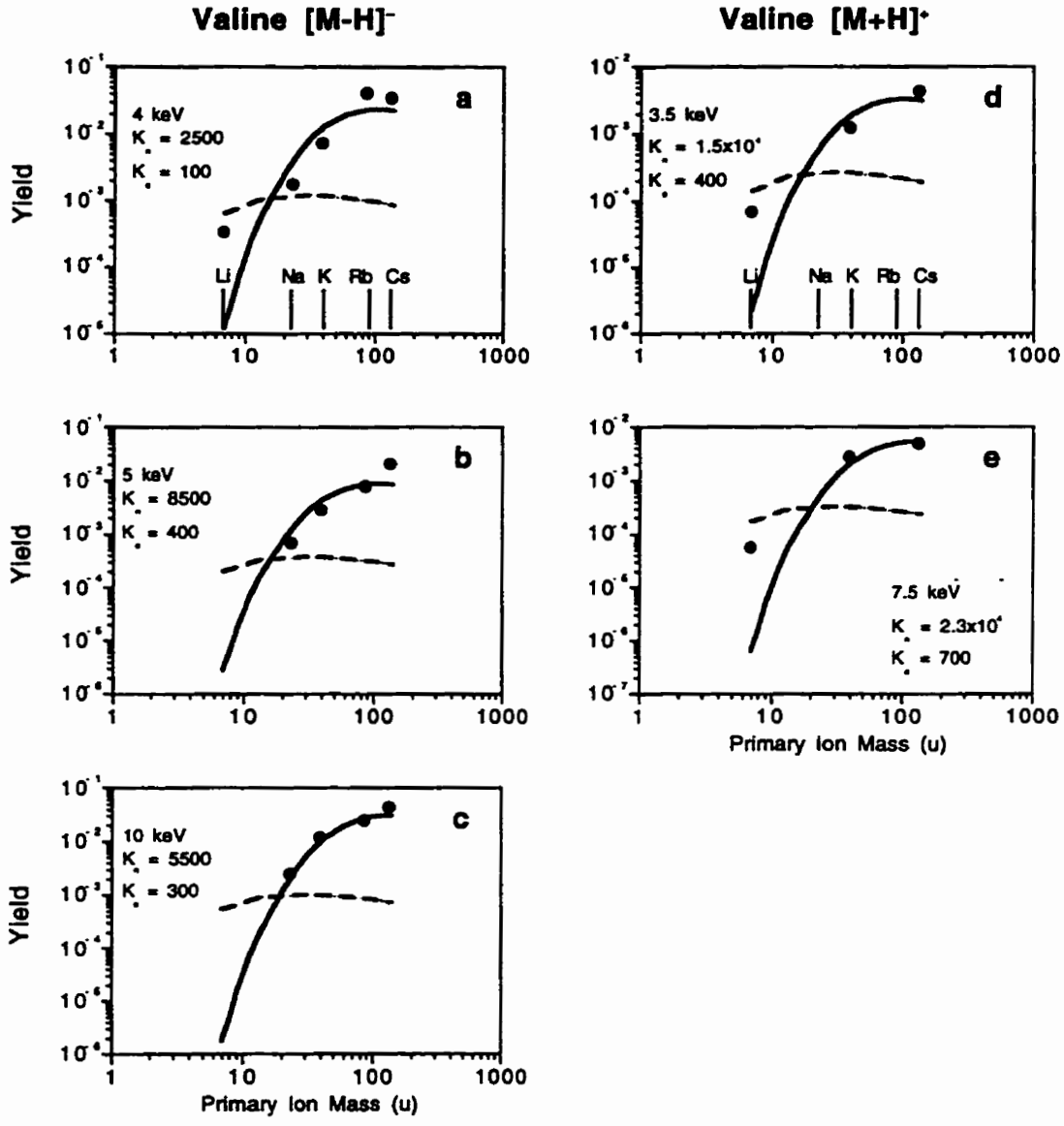

Figure 2-11: The yield of valine molecular ions as a function of primary ion mass. The impact energy of the primary ions is indicated on each graph. (a-c) $[M–H]^-$ yield. (d-e) $[M+H]^+$ yield. In each of the graphs the black line corresponds to the nuclear stopping, $(dE/dx)_n^3/K_n$, and the dashed line, electronic stopping, $(dE/dx)_e^2/K_e$ where K_n and K_e are the normalizations.

of the average. The normalization differs for different energies because of slight differences in the experimental conditions caused by, for example, opening the instrument to atmosphere to change samples and changes in the impact angle due to change in the kinetic energy of the primary ions.

In the case of the Li^+ projectile in Figure 2-11(a, d and e), the yield is an order of magnitude larger than that predicted by the nuclear stopping, suggesting a contribution from electronic stopping. The behaviour of the Li^+ projectile has been shown to be described better by the electronic stopping than by the nuclear stopping [13]; however, a linear combination of $(dE/dx)_n^3$ and $(dE/dx)_e^2$ gives a still better fit [1] which is consistent with the yields shown in Figure 2-11. The results suggest that when the magnitude of the nuclear and electronic stopping are comparable in this velocity range (see Figure 2-4b), electronic is more effective, but for the projectiles typically used in SIMS, where nuclear stopping is strongly dominant, it is the nuclear stopping that accounts for the observed molecular ion yields for both $[M-H]^-$ and $[M+H]^+$.

The validity of our approach can be demonstrated by examining the yield dependence of H^- ions, H^+ ions and electrons. It is well known that the H^+ and electron yields are correlated strongly with electronic stopping [14] and that H^- is correlated with nuclear stopping [3]. The different correlations for H^+ and H^- are evident in the mass spectra for MeV and keV ion bombardment shown in Figure 2-2a which shows a much higher relative yield of H^+ in the MeV spectra, and in Figure 2-3 which shows a much higher relative yield of H^- in the keV spectra. Figure 2-12 shows the yield data for desorbed H^+ and electrons. In contrast to the desorption of molecular ions where the yield increases by more than an order of magnitude from Na^+ to Cs^+, the e^- and H^+ yields are nearly constant as a function of mass. The black curve given by $(dE/dx)_e^2/K_e$ and the dashed curve, $(dE/dx)_n^3/K_n$, where K_n and K_e are normalization parameters given for each graph. The yields clearly follow the curve predicted by the electronic stopping power.

Figure 2-13(a–c) shows the results for H^- which is more characteristic of nuclear stopping [3]. The black bold line in the graphs is given by

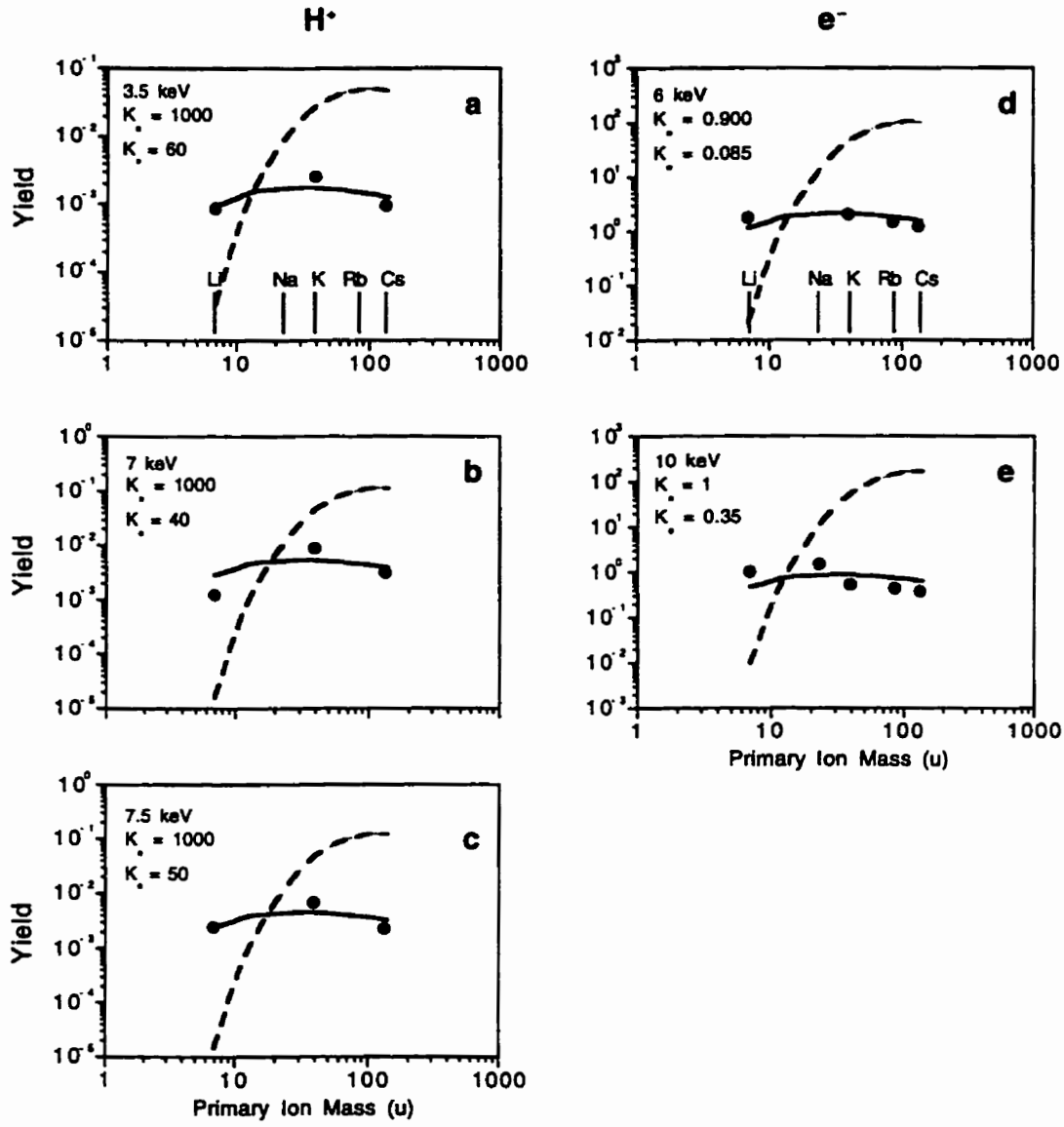

Figure 2-12: The yield of secondary H^+ (a-c) and secondary electron (d,e) as a function of primary ion mass. The impact energy of the primary ions is indicated on each graph. In each of the graphs the dashed line corresponds to the nuclear stopping, $(dE/dx)_n^3/K_n$, and the black line, electronic stopping, $(dE/dx)_e^2/K_e$ where K_n and K_e are the normalizations.

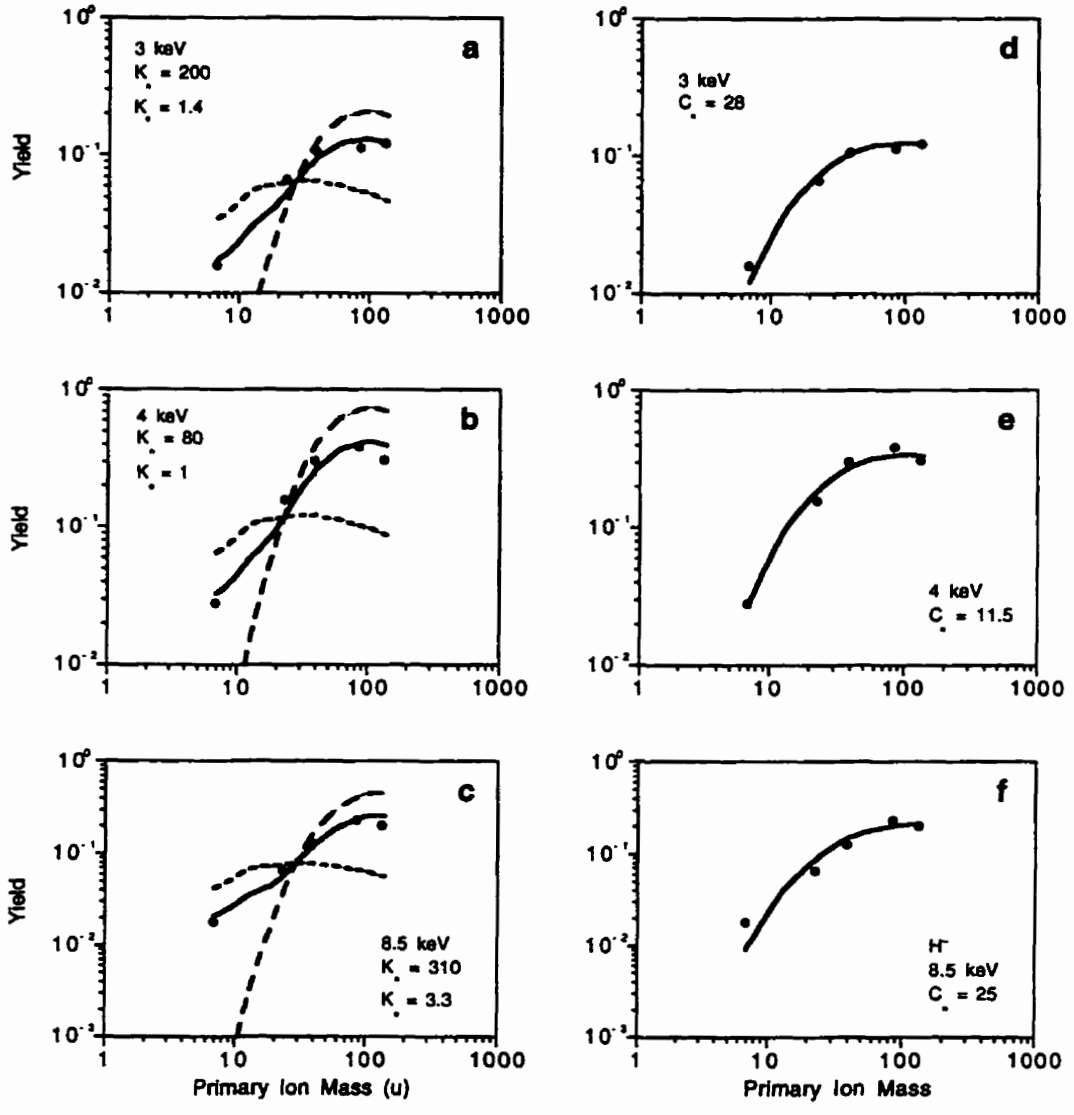

Figure 2-13: The yield of secondary H^- as a function of primary ion mass. The impact energy of the primary ions is indicated on each graph. (a–c) The solid line is a linear combination of $(dE/dx)_n^3$ and $(dE/dx)_e^2$; it is the average of the long-dashed line (the nuclear stopping term) and the short-dashed line (the electronic stopping term). (d–f) The solid lines are the nuclear stopping power $(dE/dx)_n$ just scaled by a constant. See text for details.

$$\left(\frac{dE}{dx}\right)_{avg} = \frac{1}{2}\left[\frac{1}{K_n}\left(\frac{dE}{dx}\right)_n^3 + \frac{1}{K_e}\left(\frac{dE}{dx}\right)_e^2\right]$$

where K_n and K_e are normalization constants, and the long-dashed and short-dash curves are the individual $(dE/dx)_n^3/K_n$ and $(dE/dx)_e^2/K_e$, respectively. However the same data also demonstrates a linear dependence on the nuclear stopping power, as is shown in Figure 2-13(d–f). This same linear dependence on $(dE/dx)_n$ observed with the H^- yield is also observed for other atomic ions like C^-, O^- and F^- as is shown in Figure 2-14. This is not surprising since these ions, like the H^- ion, appear in Figure 2-3 to be characteristic of nuclear stopping.

As mentioned above, the parameterization of the yields in Figure 2-11 and 2-13 with $(dE/dx)_n^3$ is simply an empirical fit to indicate a correlation. Recent results of Yen *et al* [15,16] show a quadratic dependence on the total stopping power which is not inconsistent with our parameterization. In any case, the results indicate that simple linear cascades do not likely make a significant contribution to the desorption yield of *molecular ions* because they predict a linear dependence on the energy loss; such a linear dependence is observed for the desorption of negative *atomic* ions as shown in Figure 2-13(d–f) and Figure 2-14. A high density bulk interaction such as a thermal spike or a pressure pulse are more likely to give such a steep dependence as $(dE/dx)_n^3$ [17]. The desorption of complex molecular ions are likely to be the result of secondary processes after the energy has dissipated in the solid. On the other hand, atomic ions like H^-, O^- and C^- are more likely to result from simple knock-on sputtering interactions which result in a linear dependence on $(dE/dx)_n$.

Also our results show that at low energy, when nuclear stopping is dominant, it is clearly the nuclear stopping that is responsible for the desorption of the molecular ion. In the velocity range of this experiment, our results show no polarity dependence, that is, both $[M+H]^+$ and $[M-H]^-$ are correlated with the nuclear stopping power. At higher velocities, though, where the electronic and nuclear stopping have similar magnitudes such as for Li^+ and in the experiment of Hunt *et al* [5] (see Figure 2-4 on page 16), the electronic

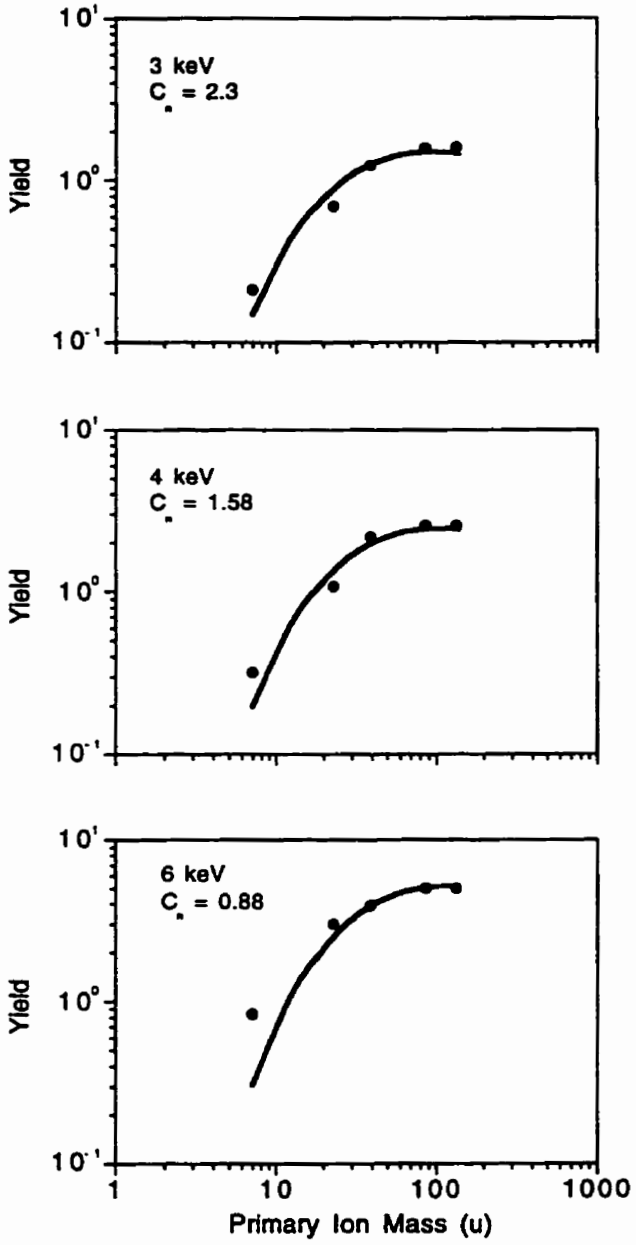

Figure 2-14: Yield of low mass ions ranging from C^- to F^-. The solid curve is nuclear stopping power $(dE/dx)_n$ scaled by some constant C_n. Impact energy of primary ions is indicated in each graph. The yield data is the integration of the peaks ranging from C^- to F^-showing a collective linear dependence on $(dE/dx)_n$.

stopping appears to be more effective in desorbing the molecular ion. However, it is more difficult to reconcile the results of Albers *et al* [7] (shown in Figure 2-5 on page 17) with those of Hunt *et al.* The experiment of Albers *et al* indicates that the nuclear stopping is more effective for desorption even when its magnitude is smaller than the electronic stopping. The discrepancy here may be related to the polarity of the molecular ions which was different in the two experiments but from our results this appears to be unlikely. Still, significantly different dependence of the valine $[M+H]^+$ and $[M-H]^-$ yields on primary-ion velocity have been observed by Becker *et al* [4] in a somewhat higher velocity range.

2.5 Conclusion

The results clearly demonstrate that for projectiles which lose energy mainly by nuclear stopping, it is the nuclear stopping that accounts *also* for the molecular ion yield, regardless of the polarity of the molecular ion. The electron and H^+ yields, on the other hand, correspond to the electronic stopping power. In the cases when the molecular ion was desorbed with a Li^+ projectile, where electronic and nuclear stopping have comparable magnitudes, the yield exceeded that predicted by the $(dE/dx)_n$ curve, suggesting that electronic stopping also plays a role.

CHAPTER 3

SECONDARY EMISSION

Secondary Ion and Electron Yield Measurements for Surfaces Bombarded with Large Molecular Ions

3.1 Introduction

With the steady increase in the accessible mass range in mass spectrometry, detection of large molecular ions has become an important problem. Detection of molecular ions in mass spectrometry is usually accomplished through a collision of the ion of interest with a surface. Either the secondary electrons or secondary ions produced in this collision are accelerated to produce a cascade, eventually amplifying the signal to a detectable level.

It is well established that as the velocity of the incident ion decreases, the secondary electron and ion yields decrease, resulting in lower detection efficiency. For example, the electron emission yield from Cu induced by bombardment with large water clusters (up to 60 000u), is reported to have a "threshold" velocity of about 18km/s corresponding to an energy per unit mass of about 1.7eV/u [1]. A similar threshold velocity was reported for insulin (5733u) incident on Cu [2]. For water clusters incident on an aluminium oxide surface there is an apparent threshold of 10km/s (0.5eV/u) [3].

From these results, a rather low detection efficiency might be expected for molecular ions with energy below about 1eV/u, if electron emission facilitates detection. In spite of this apparent low efficiency, large molecular ions have been routinely detected at con-

siderably lower velocities than 1 eV/u using secondary emission detectors. In particular, in matrix-assisted laser desorption/ionization (MALDI) the accessible molecular weight range is typically regarded as at least ~300 000u, with an accelerating voltage of 30kV. This corresponds to an energy per unit mass of ~0.1 eV/u, five times lower than the lowest threshold energy mentioned above.

The nature and the yield of the secondary particles emitted by large molecular ions are of central importance in time-of-flight mass spectrometry, the most common technique for examining ions produced by MALDI. Detectors designed to use secondary electron emission have better time resolution than detectors that rely on secondary ion emission [4–6] because of the multiple ion species and the large transit times of ions compared to electrons, an important consideration in time-of-flight (TOF) measurements. From this point of view it is preferable to use secondary electrons for detection. On the other hand, the sensitivity and the mass range depend on the emission yield of the secondary particles so it seems reasonable to use the secondary particles with the highest yield.

It has been clearly demonstrated that for incident ions below ~2eV/u the secondary ion emission yield is larger than the electron yield [4–8], suggesting an advantage in using ion emission for detection. In fact, secondary ion emission is mainly responsible for the detection of large molecular ions (mentioned above) in some detector geometries [4]. However, if the electron emission efficiency is still greater than or near unity over the mass range of interest, then a lower electron yield can be compensated by a higher multiplier or amplifier gain and sensitivity is not compromised. It is therefore important to determine the absolute electron yield for large molecules incident on detector surfaces, but much less work has been done in this area, especially at low velocities.

Many detailed measurements have been made of electron emission induced by atomic ions or relatively small polyatomic ions incident on clean, well-characterized surfaces [9,10], including measurements of kinetic emission for projectile velocities as low as 12km/s [11]. There is also a body of work on electron emission from the impact of cosmic dust at velocities lower than those considered here [12]. However, it is not obvious how

the results of either regime apply to the situation examined here: detection of very high molecular mass ions (~100ku) at low velocities (~5km/s) in the modest vacuum typical of commercial mass spectrometers.

Two main excitation mechanisms contribute to electron emission induced by particles, kinetic electron emission and potential electron emission. In *kinetic electron emission* (KEE) electrons are excited as a consequence of the atomic motion of the projectile [13]. The kinetic energy and mass of projectile are the most important quantities, whereas its chemical configuration, charge state and electronic, vibrational or rotational state are not usually of concern. This assumption is only valid at relatively high impact velocities. For KEE a threshold impact velocity exists. Let U be the minimum energy required to free an electron from the solid; then for KEE, $E_{cm} > U$, where E_{cm} is the kinetic energy in the centre-of-mass frame. Note that for a metal $U = \phi$, the work function.

Potential electron emission (PEE) results from the conversion of internal energy ε brought by a positively charged projectile, through two-electron, Auger processes [14-16]. The important quantities effecting the emission are the internal properties such as charge state and particle species (different particle species have different ionization energies, and hence different internal potential energies). The energy released in the Auger process, $\varepsilon - U$, has to exceed U (i.e. $\varepsilon > 2U$). Unlike KEE, for PEE to occur, it does not require a minimum velocity (however it may be limited by the finite approach time of the ion to the surface).

These two mechanisms are separable: when $E_{cm} < U$, and $\varepsilon > 2U$, only PEE can occur. On the other hand, if $E_{cm} > U$ and $\varepsilon < 2U$, only KEE can occur. The electron emission yield for singly-charged molecular ions incident on conversion surfaces that have been exposed to atmosphere is usually interpreted in the context of kinetic electron emission, since the relation $\varepsilon > 2U$ is not generally satisfied for the adsorbed molecules [12].

As described above, for KEE, a minimum energy must be transferred to a target electron to cause emission, and this energy corresponds to a threshold velocity for a given projectile-target combination. For incident atomic ions two extreme values can be identi-

fied for the threshold velocity depending on the mechanism assumed for the energy transfer [12], binary ion-electron collisions or binary atomic collisions. For collisions between the incident ion and the fastest free electrons, velocities higher than 150km/s are required for emission from metals, consistent with extrapolation of the experimental results for light projectiles [17]. However, if some of the momentum of the projectile is transferred to a target atom or the lattice, in *atomic* collisions, much lower thresholds are possible. The lowest possible threshold, determined by conservation of energy, corresponds to all the kinetic energy being transferred to the target electron. For an oxygen projectile (the largest abundant atom in organic molecules) incident on a low work-function surface ($\phi \approx 2.6\text{eV}$), this corresponds to about 5km/s or 0.13eV/u [12]. The situation becomes more complicated with polyatomic projectiles, where multiple collisions could clearly reduce the threshold further; obviously conservation of energy is not a limit if the total energy of the projectile is ~30keV.

Because the energy transferred to a target electron must exceed its binding energy, it is reasonable that most empirical or theoretical characterizations of kinetic electron emission have threshold velocity as a parameter. Such descriptions lead to extraction of threshold values from data acquired at higher velocities, without direct evidence of a true threshold. For example, in binary atomic collisions, the extrapolated value of the threshold velocity is ~45km/s for gas-covered, electron multiplier surfaces [18], roughly independent of the type of bombarding ions. However, if a different mechanism dominates for velocities near or below the extrapolated "threshold", the term is inappropriate. As early as 1958, measurements of kinetic electron emission for atomic ions on metals have been reported for velocities down to 15km/s, a factor of 3 lower than the extrapolated threshold [19]. Similar results have been reported more recently [11,20] for velocities as low as 12km/s [11]. The emission probability in these experiments was very low ($\leq 10^{-4}$) and the measurements were limited by experimental sensitivity and not by an obvious threshold velocity. The measurements of Beuhler and Friedman [1,3] using large water clusters, are in the same velocity range, but because of the large polyatomic projectiles, contribution to

"molecular effects" in KEE, the emission efficiency was greatly enhanced. Indeed, values of electron yield less than one electron per incident cluster could not be measured by their method. The interpretation of the lowest velocity for which a yield higher than 1 is observed, as a threshold velocity is therefore rather arbitrary. There is a clear need to determine the behaviour of the electron yield at lower velocities typically encountered in detecting MALDI ions.

The expectation from previous work was that the electron yield would vanish at low velocities [1-3], and that seems to be consistent with some of the measurements of the ratio of the electron-to-ion yields [4]. However our previous measurements of the electron-to-ion ratio indicate clearly that the electron signal does not vanish, at least for energy per mass unit as low as 0.25eV/u (7km/s) [5,8]. For this velocity, the ratio is ~0.10 and only weakly dependent on mass. These earlier measurements give no information on absolute yield, but measurements made at Orsay [6] for 18keV albumin (0.3eV/u) incident on CsI give an absolute secondary ion yield >1 and an electron-to-ion ratio of about 0.06.

In this experiment, using single-ion counting methods and a coincidence technique similar in principle to the method used by the Orsay group [6], we measure the absolute emission efficiency of secondary electrons and secondary ions as a function of the velocity and mass of the molecular ions incident on different surfaces for velocities down to 3.5km/s (0.06eV/u). Our primary interest is to determine the feasibility of using the secondary electrons for detection of high mass, low velocity molecular ions. In particular, for a given accelerating voltage, how does the efficiency of electron emission depend on mass, and what loss of efficiency (if any) must be tolerated to take advantage of the better time resolution accessible with detectors that use electron emission?

3.2 Experimental

3.2.1 Instrumentation

The experimental arrangement shown in Figure 3-1 is similar to the arrangement described previously [5,8] with a few modifications. The molecular ions produced at the

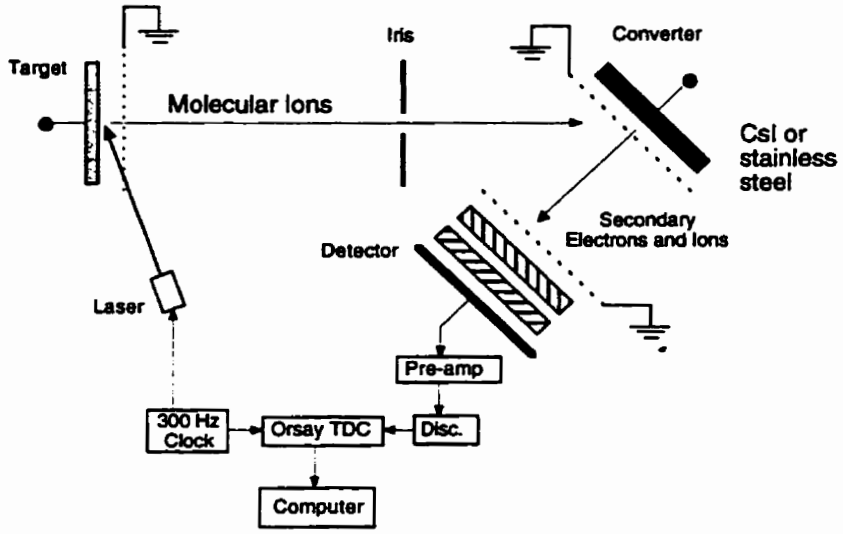

Figure 3-1: Schematic diagram of the experiment. The relevant dimensions and voltages are given in the text.

target by MALDI are accelerated into a primary flight tube (~83 cm long), pass through a small adjustable iris (~55 cm from the target) and strike a conversion plate (converter) at 45°. Secondary electrons and ions produced at the converter are accelerated into a second flight tube (~18cm long) and are then detected in a 4cm diameter microchannel plate detector. Amplified signals from the microchannel plates are fed into a 255-stop time-to-digital converter (TDC) (model CTN-M2, Institut de Physique Nucleaire, Orsay, France) connected by a custom interface to an Atari TT030 computer for data storage and analysis. Although single-ion counting methods have limitations, it is easier to interpret the data quantitatively than when a transient recorder is used.

The primary ions were produced by laser pulses of width 10–20 ns from a high repetition rate excimer laser (HE-460-HR-B: Lumonics Inc., Kanata, ON, Canada) incident on the target at 70°. (The optics are shown in Figure 3-2.) Triggered by a digital delay generator (9650 EG&G PARC), the laser was typically operated at 300 Hz with XeCl (308 nm). The power density was between 10^6 and 10^7 W/cm^2, controlled by a circular gradient neutral density disk. The beam focus was manually rastered across the target with a dis-

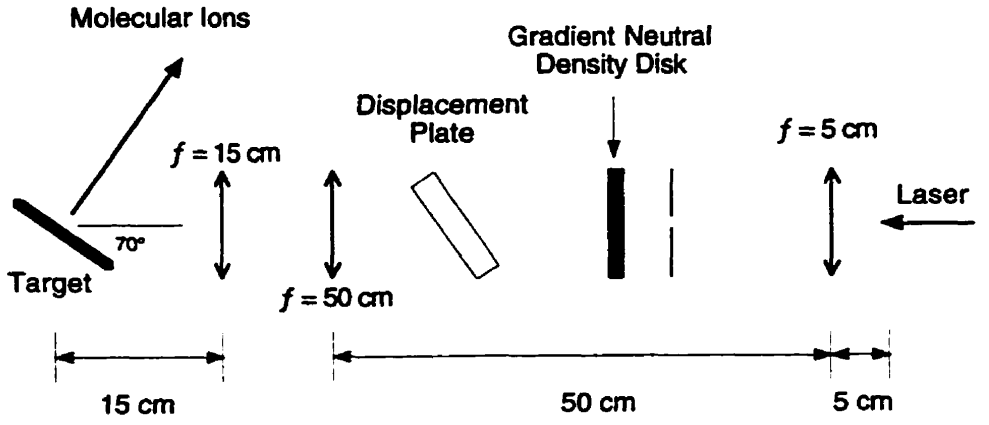

Figure 3-2: Optics for focusing laser on to target samples.

placement plate.

Primary ions were produced from standard samples of insulin (5733u), trypsin (~23 540u), human transferrin (~79 500u) and ß-galactosidase (~113 600u). These peptides were prepared according to the usual procedure for matrix-assisted laser desorption [5] using sinapinic acid as a matrix. "Primary" ions produced by the laser were accelerated across a potential difference V_a (typically between 5–25kV) applied between the target and a grounded 90% transmission grid. The accelerated primary ions passed through a small iris with adjustable size, positioned about 55 cm from the target. The aperture size could be varied from zero (completely closed) to ~5mm^2, allowing control of the primary ion transmission to the converter; usually it was set so that the probability of transmitting one ion per laser pulse was much less than unity.

Secondary ions and electrons were produced at the converter from surfaces of stainless steel and CsI; a few measurements were also made with CuBe. The stainless steel surface was cleaned in an ultrasonic bath in acetone, and rinsed with methanol. CsI surfaces were prepared by evaporation onto a clean stainless steel disk under a vacuum of ~100mTorr. The surfaces were then transported (at atmosphere) into the spectrometer which is subsequently pumped to ~1×10^{-6} Torr.

Secondary ions were accelerated between the converter at –100V and a grounded grid (95% transmission). A high transmission grid and low voltage were used to minimize

the production of spurious electrons [5,6,8]. To avoid detector saturation from the intense secondary electron signal created by the low-mass, primary ions from the matrix, the extraction voltage was pulsed from a small positive voltage to the −100V accelerating voltage at some appropriate delay time after the laser pulse.

The front plate of the detector was held at +2kV to provide post-acceleration for the low energy (100 eV) ions and electrons. A grounded 95% transmission grid about 1cm in front of the detector maintained zero field in the flight tube. A schematic diagram of the detector is shown in Figure 3-3.

A magnetic field produced by a coil wound around the detector was used to improve secondary electron transmission which is rather sensitive to stray magnetic fields, e.g., the earth's magnetic field. This applied field, which causes electrons to spiral into the detector, was increased empirically until the transmission saturated at a value about 40% higher than with zero applied field. The measured field strength for the optimum (6A through 100 turns) was ~10G near the detector and ~3G near the converter.

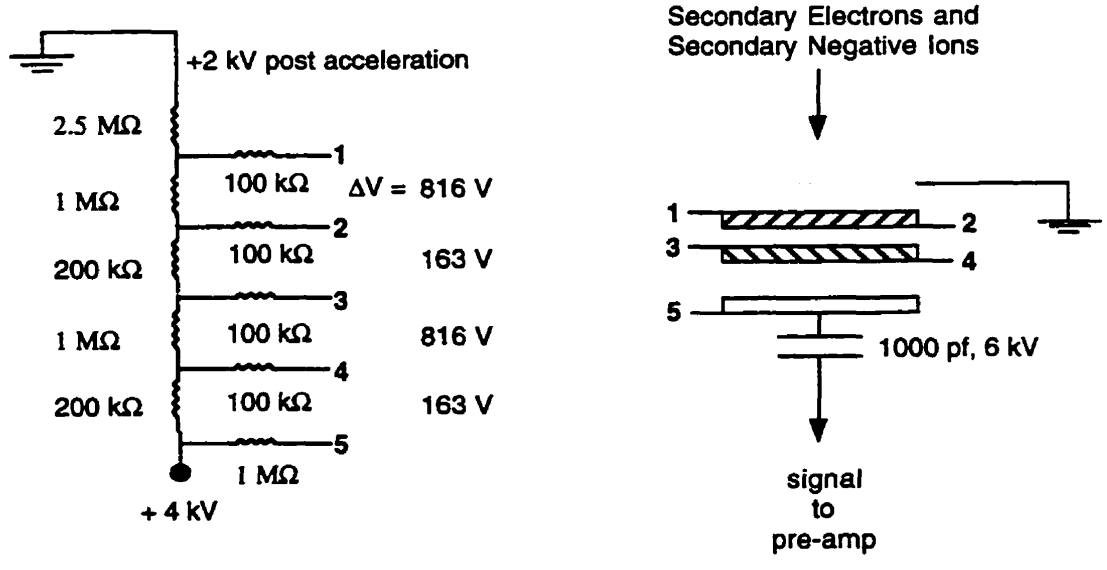

Figure 3-3: Secondary electron and secondary ion detector.

3.2.2 The Coincidence Method

When a large number of molecular ions N_o are incident on a solid surface (the converter), the number of secondary electrons ejected N_e is given by

$$N_e = \gamma_e N_o$$

where γ_e is the *secondary electron emission coefficient*. Similarly for the secondary ions:

$$N_i = \gamma_i N_o$$

Ideally, our aim is to determine the secondary electron and ion coefficients as a function of mass and velocity for different surfaces.

Assuming the electron multiplicity follows a Poisson distribution [21], the probability for ejecting exactly n electrons from a *single* primary ion impact is

$$P_e(n) = \frac{\gamma_e^{\,n}}{n!}\exp(-\gamma_e)$$

The validity of Poisson statistics has not been rigorously demonstrated for low velocity projectiles where $\gamma < 1$, but the assumption is reasonable based on results at higher velocities where $\gamma > 1$ [21].

The *electron emission efficiency* ε_e corresponds to the probability for ejecting *one or more* electrons for a *single* primary ion impact. Thus,

$$\begin{aligned} \varepsilon_e &\equiv 1 - P_e(0) \\ &= 1 - \exp(-\gamma_e) \end{aligned} \tag{3-1}$$

where $P_e(0)$ is the probability that no electrons are emitted. Similarly, the secondary *ion emission efficiency* is defined as

$$\varepsilon_i \equiv 1 - P_i(0) \tag{3-2}$$

where $P_i(0)$ is the probability that no ions are emitted, which may or may not be Poisson distributed. Note that ε_e represents the *probability* that a *single* primary ion is detected by electron emission. Whereas the electron coefficient γ_e can take any positive value, the efficiency ε_e is necessarily less than (or equal to) unity because an incident primary ion produces at most one pulse in a single-ion counting system regardless of the number of

electrons ejected. Thus, ε_e is a measurable quantity with single-ion counting. Similarly for ε_i.

After N events where exactly *one* primary ion hits the surface, the measured number of secondary electrons, n_e, and secondary ions, n_i, is given by

$$n_e = \varepsilon_e N \tag{3-3}$$

$$n_i = \varepsilon_i N \tag{3-4}$$

Thus, if one *or more* electrons are ejected at the same time, then it will only count as one measured event due to the single-ion counting with the TDC. The same is true with the ejected ions.

The number of events in which *both* an electron and an ion are ejected (in coincidence) is given by

$$n_{ei} = \varepsilon_e \varepsilon_i N \tag{3-5}$$

assuming that there is no correlation between the electrons and negative ions. Combining Eqn. (3-5), the coincidence relation, with Eqns. (3-3) and (3-4) gives

$$\varepsilon_e = \frac{n_{ei}}{n_i} \tag{3-6}$$

$$\varepsilon_i = \frac{n_{ei}}{n_e} \tag{3-7}$$

where n_e, n_i and n_{ei} are all measurable quantities with single-ion counting.

Finally, the electron emission coefficient γ_e, can be calculated from Eqn. (3-1):

$$\gamma_e = -\ln(1-\varepsilon_e) \tag{3-8}$$

Taking into account electron transmission, T, of the instrument, Eqn. (3-8) becomes

$$\gamma_e = -\ln(1-\varepsilon_e)/T \tag{3-9}$$

where $\gamma_e T$ is the total number of electrons that reach the detector. In this experiment the electron transmission is mainly limited by the grids ($T = 0.95^2$); the path of the ejected electrons is otherwise well contained as there is a short secondary flight tube and a magnetic field to axially confine the electrons. In addition, there is a large (+2kV) post accel-

eration on the detector and the detector is run in saturation mode so its efficiency is close to unity.

For experimental data with appreciable associated uncertainties, this conversion is only reliable for efficiencies considerably less than unity. As the efficiency approaches unity, the corresponding uncertainty in γ_e, $\Delta\gamma_e$, becomes more and more magnified, as

$$\Delta\gamma_e = \Delta\varepsilon_e\left(\frac{d\gamma_e}{d\varepsilon_e}\right)$$

$$= \frac{\Delta\varepsilon_e}{1-\varepsilon_e}$$

For this reason, although the emission coefficients are more fundamental, the data in this experiment are first presented as efficiencies. This is, in any case, the relevant figure-of-merit in determining the molecular weight range of the technique, particularly when single-ion counting is used. Only the probability that an ion will produce one or more secondary electrons (or ions) is important in determining whether it will be detected or not. The actual number of electrons that are produced only influences the necessary gain of the amplification electronics. (The emission coefficient is of course relevant to the relative intensity of different peaks when a transient recorder is used, and is therefore related to mass discrimination.)

Random Correlations

The equations above are valid under the condition that only one or zero primary ions strike the surface of the converter for every successful laser desorption event. Random correlations occur when two primary ions strike the converter, distorting the results. To experimentally control the number of primary ions hitting the converter, an iris (mentioned above) is placed between the MALDI ion source and the converter. The aperture is set small enough so that the probability for transmission of a single primary ion is much smaller than unity to minimize the number of random correlations.

To determine the extent of the random contributions, correlations with a second

primary ion projectile (usually the doubly charged molecular ion) are also monitored. If the number of events where both the singly-charged (A) and doubly-charged (B) primary ions pass through the iris (AB or BA) is kept very low, then the number of events where two singly-charged (AA) or two doubly-charged (BB) primary ions pass through the iris is lower by a factor of two assuming all four possibilities have equal probability. Typically the probability for a singly and doubly charged ion to be detected in the same event is less than 5%. Thus reasonable accuracy can be expected for efficiencies $> -10\%$.

Data Acquisition

The measured time intervals from each laser shot are analysed and sorted by the data acquisition software and two spectra are recorded. The first spectrum is the full spectrum; it is simply a histogram of all the recorded time intervals between the laser pulse and the detection of secondary ions and electrons. An example of such a full spectrum is shown in Figure 3-4a. The second spectrum (Figure 3-4b) is a coincidence spectrum; it is a histogram of the recorded time intervals from selected events in which at least one measured time interval falls within a certain, pre-defined time window.

To measure n_{ei}, a time-window is set with the software around the electron peak from the primary ion of interest, and if an electron is counted within this window for a given laser shot, then the measured stop times for that event are recorded separately in a coincidence spectrum, as in Figure 3-4b. Thus, after several (hundred) laser shots, the number of ions counted, n_i, in the coincidence spectrum is, in fact, the number of events, n_{ei}, where both electrons and ions were ejected. The efficiencies ε_e and ε_i (for any single secondary ion species) can then be calculated from the two spectra using Eqns. (3-6) and (3-7); the values of n_e and n_i are obtained from the full spectrum, Figure 3-4a.

To improve the statistics and because individual ion species are not resolved, it was necessary to integrate the intensity for all ion species which range in mass from about 1 u to 125 u for the quantities of n_i and n_{ei}. However, the development of Eqns. (3-6) and (3-7) assumes that multiple secondary ions from the same primary ion are counted as a *single*

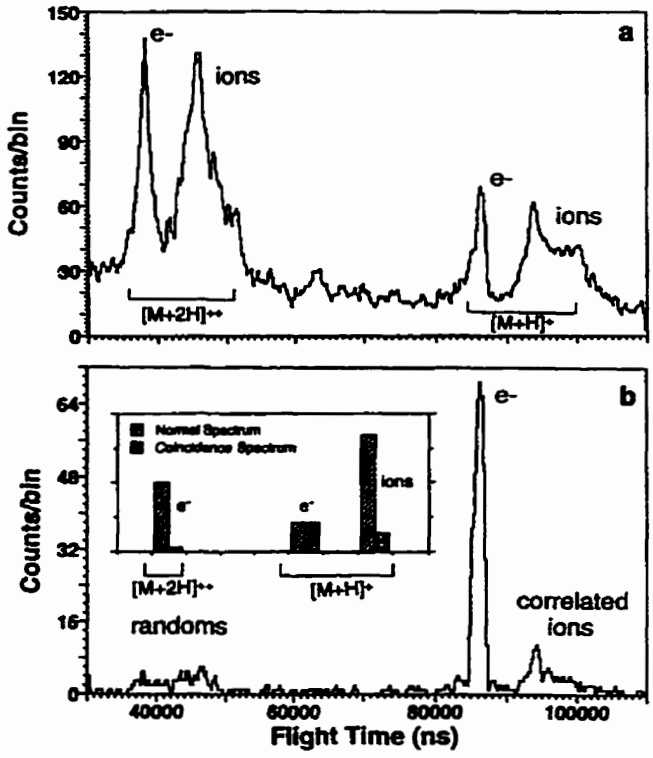

Figure 3-4: (a) TOF spectrum of secondary ions and secondary electrons produced at a stainless steel surface by bombardment with singly- and doubly-charged molecular ions of human transferrin (79 500u) at 10 and 20keV, respectively. (b) Coincidence spectrum recorded with a time window around the secondary electron peak for incident [M+H]+. The inset shows the integrated counts for the indicated peaks, showing the degree of random coincidences form different incident projectiles.

pulse. This is the case for secondary ions of the same species but not usually for secondary ions of different species. To maintain the validity of Eqns. (3-6) and (3-7), an additional constraint was applied using the software so that at most one ion within the selected range was registered for a given event; in effect the deadtime was increased in a selected time range. Thus n_i and n_{ei} represent the total number of events in which at least one secondary ion is detected in the selected range of 1u to 125u, in other words, all ions between 1u and 125u are treated a single peak in the mass spectrum.

3.3 Results & Discussion

The determination of the secondary electron and ion emission efficiency using the coincidence technique is illustrated for incident molecular ions of human transferrin (79 500u) at 10keV (0.13eV/u). Figure 3-4a shows the full spectrum of the secondary ions and electrons ejected by collisions of the $[M+H]^+$ and $[M+2H]^{2+}$ ions with the converter. Figure 3-4b is the coincidence spectrum recorded with a time window around the secondary electron peak for $[M+H]^+$. The number of counts from $[M+2H]^{2+}$ in the coincidence spectrum compared to the full spectrum indicates the degree of random correlations, in this case less than 3%. On the other hand, the percentage of the ions from the [M+H]+ ion in correlation with the electrons from the same primary ion is about 16%. Thus 16% of the events in which an ion is observed also produce an electron, that is, $\varepsilon_e = n_{ei}/n_i = 0.16$, where n_{ei} is the yield of the secondary ions in the coincident spectrum (between 87 and 102ms). The data also indicate that in 64% of the events in which an electron is observed, an ion is also observed, that is $\varepsilon_i = n_{ei}/n_e = 0.64$.

Figure 3-5 shows the secondary electron efficiency as a function of energy per unit mass for insulin, trypsin, transferrin and β-galactosidase incident on a CsI surface and a stainless steel (SS) surface. The data have been corrected for known losses due to grids, using Eqns. (3-1) and (3-9) giving

$$\begin{aligned}\varepsilon_e &= 1-(1-\varepsilon_e(\text{measured}))^{1/T} \\ &= 1-(1-(n_{ei}/n_i))^{1/T}\end{aligned}$$

in which the geometrical transmission was taken as T; other possible losses have not been accounted for. For both surfaces, the electron efficiency decreases with decreasing velocity for a given mass, and for a given velocity, the efficiency increases for larger masses. The SS plot in Figure 3-5 also shows that the secondary electron yields are very similar for both the singly-charged and doubly-charged molecular ions of transferrin at the same velocity.

The efficiency for ion emission for the same projectiles and surfaces is shown in

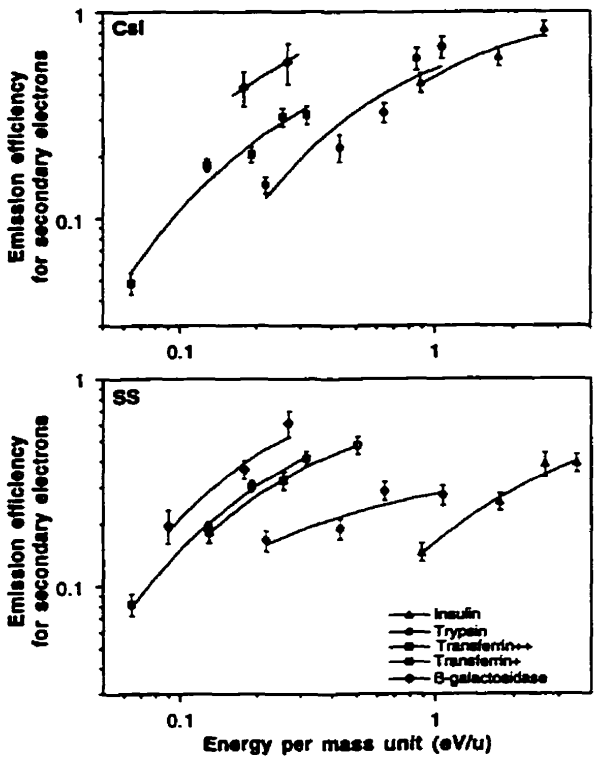

Figure 3-5: Efficiency of secondary electrons emission ε_e for various incident projectiles on a CsI surface and a stainless steel (SS) surface. The efficiency was corrected for known losses due to grids. The error bars represent statistical uncertainty. The curves are fits of the derived electron coefficient (using Eqn. (3-9)) to a velocity dependence given by $\gamma_e = \gamma_o \exp(-v_c/v)$.

Figure 3-6. As has been reported before [6], the efficiency is close to unity even for low velocities, where it is considerably higher than the electron efficiency.

It is useful to separate the influence of the mass and the velocity in the electron emission data. If the average number of ejected electrons, γ_e, is simply proportional to the primary ion mass, i.e. to the number of atoms in the molecule, then it is reasonable to normalize the data by dividing γ_e by the mass, or by the number of components in the projectile. Such an additivity rule, which assumes the atoms interact independently with the surface, is not universally applicable, and depends on the velocity regime and the size of

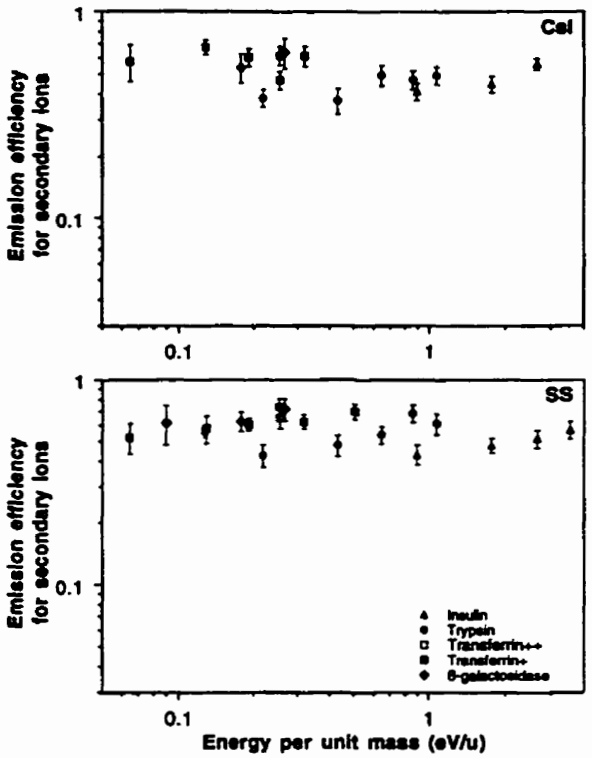

Figure 3-6: Efficiency of secondary ion emission (for ions between 1 and 125u) for various incident projectiles on a CsI surfaces and a stainless steal (SS) surface. The efficiency was corrected for know losses due to grids. The error bars represent statistical uncertainty.

the projectiles [3,12]. It appears to hold for water clusters incident on Cu at low velocities [1], and for peptides incident on microchannel plates at velocities down to 15km/s [22]. Deviations from the additivity rule were reported for water clusters on Al_2O_3 and for peptides at relatively high velocities (>100km/s) on CsI and Al_2O_3 surfaces [23]. Recent measurements for large multiply-charged molecular ion projectiles at velocities above ~30km/s show a linear dependence on mass for a graphite surface but a sublinear dependence (proportional to $M^{0.73}$) for Al_2O_3 [24]. The present data for electron emission (Figure 3-5) fall more or less on a single curve if the derived emission coefficient (γ_e), calculated with Eqn. (3-9), is divided by the mass of the projectile, as shown in Figure 3-7. The degree of fluctuation in these reduced coefficients is rather large, but Figure 3-7 indi-

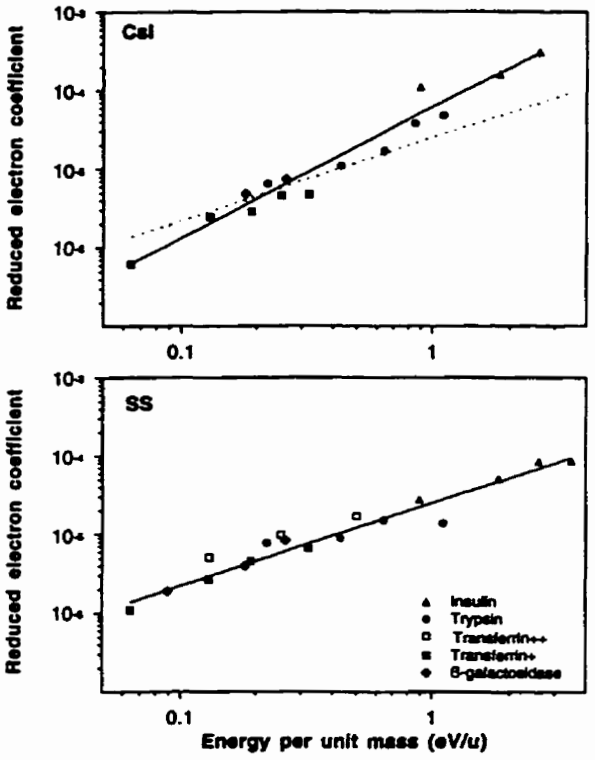

Figure 3-7: Reduced electron yields (γ_e/m) for various projectiles on a CsI surface and a stainless steal (SS) surface. The measured efficiencies were converted to yields γ_e with Eqn. (3-9) and divided by the mass of the projectile. The lines through the data are fits to $\gamma_e = av^b$; where the exponent is 2.1 for the stainless steel target and 3.3 for the CsI target. The fit from the SS data is reproduced as a dashed line on the CsI plot for comparison.

cates the data are at least consistent with a linear mass dependence.

A non-linear yield enhancement has not been reported for electron emission by polyatomic bombardment in this velocity range. The deviations from linearity mentioned above all correspond to yields that are lower than the sum of the expected yields for the constituent atoms. However, for dust particles at velocities as low as 0.1km/s, kinetic emission by the individual atoms is not possible and the electron emission is attributed to a heat spike produced by the impact of the cluster, clearly a collective effect [12]. The detection of electrons in our experiment at velocities down to 3.5km/s (0.06eV/u) similarly suggests a cooperative effect may be present even if comparisons between various large

polyatomic projectiles do not indicate an enhancement. The decrease of the electron yield with decreasing velocity is characteristic of kinetic electron emission, but there is no indication of a threshold, and at the lowest velocity the individual atoms do not have sufficient energy to induce kinetic emission; atoms smaller than O have energy less than 1 eV.

The electron emission data for the individual projectiles (Figure 3-5) fit an exponential dependence on the inverse velocity, $\gamma_e = \gamma_o \exp(-v_c/v)$ [12], but collectively the reduced data (Figure 3-7) are better described by a simple power law. The dependence on velocity in this range appears to be approximately quadratic for the stainless steel surface, and cubic for the CsI surface.

Figure 3-7 indicates that the difference between the secondary electron yield from non-characterized surfaces of stainless steel and CsI surface. As previously reported [8,23,25] CsI gives a significant enhancement in the electron yield compared to stainless steel, when the incident energy per mass unit is >1 eV/u. This is true even after both surfaces have been exposed to atmosphere and are examined at 10^{-6}Torr, although the enhancement decreases with prolonged exposure to atmosphere [8]. The present results also show that the enhancement is reduced at lower velocities, and below about 0.4 eV/u, there appears to be little dependence on the type of conversion surface, although a somewhat higher efficiency is observed for the stainless steel surface. The influence of the velocity on the surface dependence is illustrated clearly in Figure 3-8 which shows a comparison between the spectra obtained from the two surfaces using different primary projectiles with an energy of about 20keV. For cytochrome C at 1.5 eV/u there is a large enhancement (by about a factor of 6) in the intensity of the secondary electron peak from a CsI converter, and there is no noticeable enhancement for albumin $[M+H]^+$ at 0.3 eV/u. This result is reasonable since lower velocity projectiles are likely to be more sensitive to surface contaminants and less sensitive to the nature of the substrate. Measurements of emission efficiency with a CuBe surface were not appreciably different from those obtained with a stainless steel surface in this mass and velocity regime.

The curves obtained in Figure 3-7 are plots of the reduced electron coefficients as a

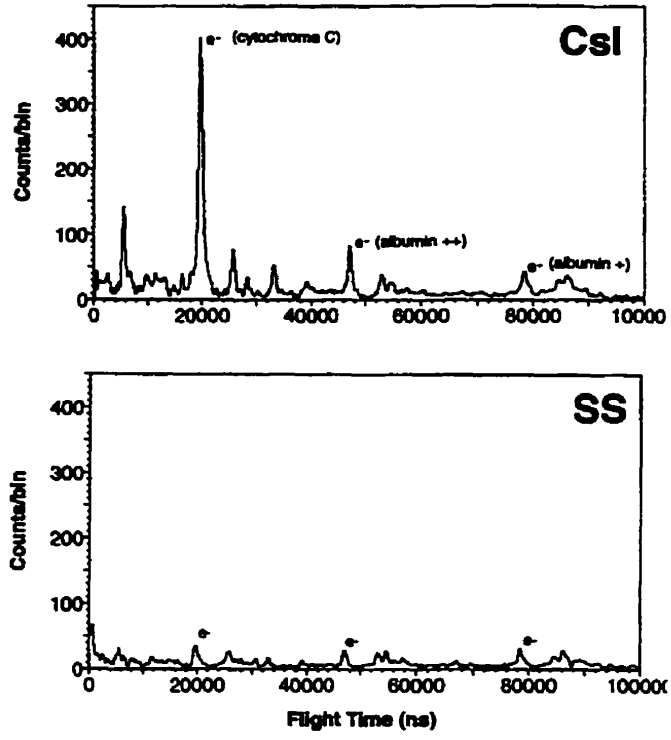

Figure 3-8: TOF spectra of secondary electrons and secondary ions from three projectiles incident on a CsI surface and a stainless steel (SS) surface. The indicated flight time includes the flight time of the incident projectile. The electron peaks from the three projectiles (which have different velocities) are denoted. The clear enhancement observed with a CsI target for high velocity projectiles is absent at lower velocities (higher times).

function of velocity, where both the energy and primary ion mass were varied. However, for a given mass spectrum, all the projectiles of various masses have the same energy. Thus, a more practical curve should indicate the efficiency as a function of mass for a given energy. We have used the data of Figure 3-7 to derive such a plot for several different accelerating voltages in the range typical of MALDI; the results are shown in Figure 3-9. For accelerating voltage at or above 30 kV (the most common value) Figure 3-6 shows that detection based on ion emission gives efficiency near unity for the entire mass range, as mentioned above. Figure 3-9 shows that detection based on electron emission for this voltage is somewhat lower (about 50% for molecular weight of 100 000u) but still clearly

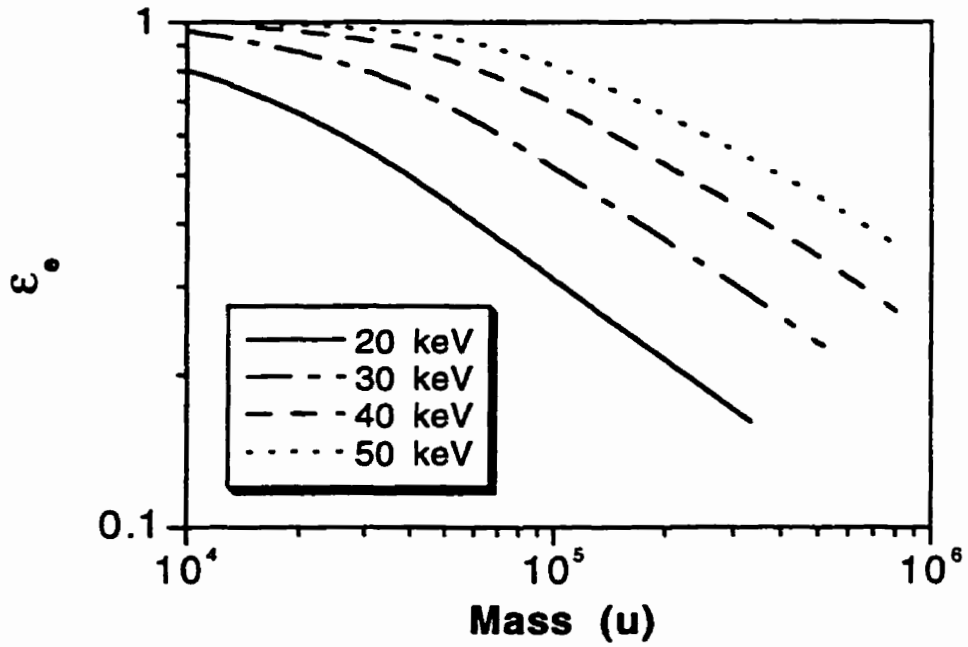

Figure 3-9: Efficiency for electron emission from a CsI surface as a function of projectile mass for various accelerating voltages. The curves are derived from the fit to the data of Figure 3-7.

feasible.

Recently, the Orsay group, by employing single-ion counting, has made measurements of secondary electron emission yields from a CsI surface under impact of large molecular ions at low velocities [26] in a similar mass and velocity range as in this experiment. Figure 3-10 shows the Orsay data superimposed on the plot from Figure 3-7 with the CsI target. The Orsay data are systematically lower by about a factor of 5 at 0.1eV/u and a factor of 2 at 1eV/u. In estimating transmission (detection efficiency), several factors can effect the yields, such as, for example, random correlations (discussed above), impact angle, and the exact nature of impact surface. Thus the difference between the two measurements are not surprising.

3.4 Conclusion

Electron and ion emission were observed from stainless steel and CsI for incident projec-

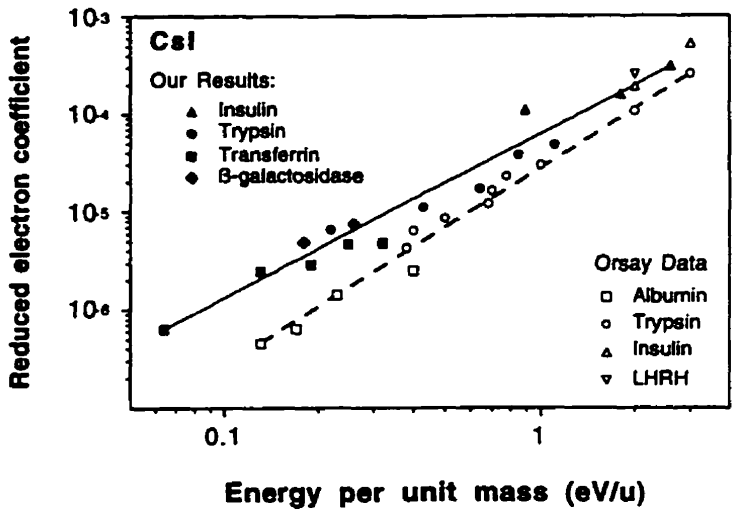

Figure 3-10: Comparison of reduced electron coefficient for this experiment (data from Figure 3-7, CsI target) and recent Orsay data [26].

tile velocities as low as 3.5km/s (0.06eV/u). Using secondary ion emission, the detection efficiency in mass spectrometry of large molecular ions up to at least 300 000u, can be near 100% if the ions are accelerated to 30keV. The efficiency of a detector that relies on secondary electron emission is somewhat lower but still near 30% for this extreme case. For large molecular ions with energy per unit mass less than 0.4eV/u, the detection efficiency is insensitive to the nature of the surface in a modest vacuum ($\sim 10^{-6}$ Torr).

CHAPTER 4

POST SOURCE DECAY

A Method for Metastable-ion Analysis in a Reflecting TOF Instrument with Precursor Ion Selection

This experiment is quite different from those reported in the previous two chapters, being more application-orientated (practical) and less fundamental. Though we are not directly investigating the desorption/ionization process itself, the project is related as we are analysing the fragment ions produced due to the energy transferred from the desorption/ionization event, specifically in MALDI.

Since the start of organic MS, the trend has been to try to desorb and ionize larger and larger *intact* biomolecules. Limiting the pace of success in this goal has been the fragmentation of the biomolecules due to the still relatively harsh desorption/ionization techniques. MALDI has successfully produced intact molecular ions up to mass 300 000Da, however, even with this "soft" ionization process, there is still significant degree of metastable ion fragmentation, which can actually be rather useful. The unimolecular decay of peptides offers a way to obtain sequence and structural information, and in this chapter we are proposing a variation on the standard method for analysing such fragments of molecular ions.

4.1 Introduction

Molecular ion fragmentation in a reflecting TOF instrument (Figure 4-1) can occur any

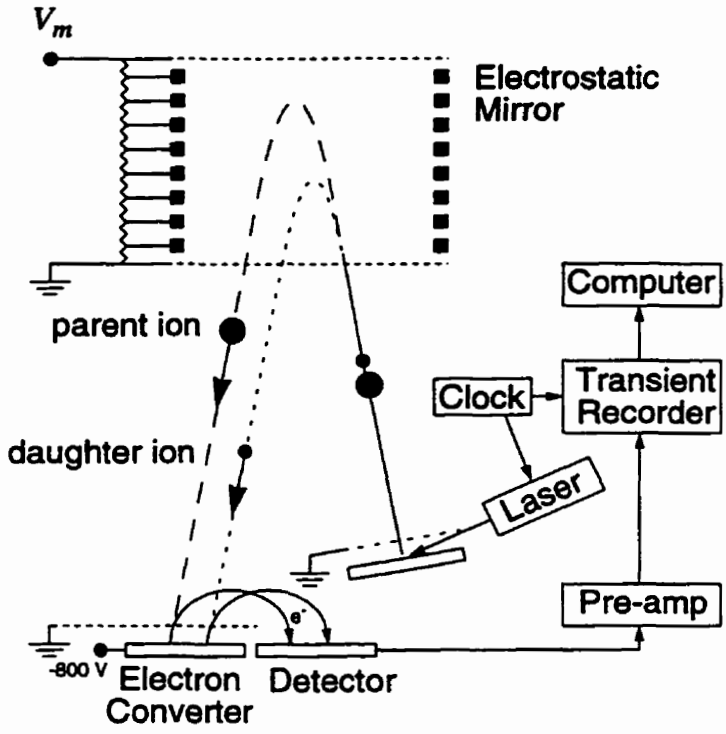

Figure 4-1: Schematic diagram of the reflecting time-of-flight mass spectrometer and data system. See Experimental section on page 65 for details.

time after production and before detection. However, the fragments that appear in the spectrum as separated peaks are those that are produced in the field-free region after the ions have been accelerated out of the ion source and before they enter the mirror. This decay stems primarily from the multiple collisions of analyte ions with matrix molecules during early plume expansion and ion acceleration [1].

Reflecting time-of-flight mass spectrometers provide an elegant method of obtaining daughter-ion spectra from the metastable decay of parent peptides. The idea was first demonstrated in PDMS by LeBeyec *et al* [2] and for SIMS by Tang *et al* [3]. The method was introduced for MALDI by Spengler et al [4,5] who referred to it as "post-source decay" (PSD).

Figure 4-1 shows a schematic diagram of a TOF spectrometer with a single-stage ion mirror. A full description of the instrument is in the Experimental section on page 65.

A normal TOF spectrum is obtained when ions produced at the target by a laser pulse are accelerated to an energy qV_a and follow the long-dashed path to the detector without breaking up. In this case the mass m is related to the measured time t (for a singly charged ion) by the equation

$$\sqrt{m} = a(t - t_o) \tag{4-1}$$

and the constants a and t_o are determined by calibrating with two peaks of know identity. This is the standard calibration equation used in TOF-MS for both linear and reflecting MS instruments.

The mirror provides velocity focusing to reduce the influence of initial velocity on the flight time and is set to provide focusing for ions with a mean energy of qV_a. Variations from the velocity corresponding to this energy are compensated to first order in a single-stage mirror (shown in Figure 4-1) and to second order in a two-stage mirror.

If an ion breaks up in the field-free region before it enters the mirror, the total flight time of the daughter ion will be smaller than that of the parent ion because it has less energy (less mass and approximately the same velocity) and is therefore reflected by the mirror in less time (short-dashed curve in Figure 4-1). For one- or two-stage mirrors, daughter ion peaks with molecular mass m_d near the parent mass m_p have comparable resolution to that of the parent and appear in the spectrum close to the position predicted by the original calibration equation, that is $\sqrt{m_d} \cong a(t_d - t_o)$, where t_d is the measured time-of-flight of the daughter ion. This is because the daughter ion energy is close to the energy for which the mirror is optimized and so it provides compensation for the fraction of energy lost $(m_p - m_d)/m_p$ in the decay, as well as focusing for the energy spread. However, as the mass of the daughter ion decreases, its energy departs further from the optimum, resulting in broader peaks and greater displacement from the mass position predicted by the usual calibration. For this reason, daughter ion spectra obtained with uniform-field mirrors are normally acquired in segments with different mirror voltages.

If the mirror voltage is reduced from V_m (the optimum for the parent ions that do not fragment) to $V'_m = V_m(m_d/m_p)$, then it will be optimized for daughters of mass m_d.

In this case, the mirror provides much better compensation for the energy spread of the daughter and thus much sharper peaks are obtained. The flight time of the daughter ion under these new conditions is the same as the parent ion with the original mirror voltage; the daughter ion now follows the long-dashed line in Figure 4-1. Thus, reducing the mirror voltage restores the resolution, but changes the calibration equation. As above, with this new mirror voltage V'_m , other daughter ions with masses close to m_d will also have comparable resolution to that of the ion of mass m_d and appears in the spectrum close to the position predicted by the new calibration equation, thus allowing mass determination for a segment of daughter ion masses. This procedure of decreasing the mirror voltage to obtain a segment of daughter ion masses requires a different calibration for each new mirror voltage, a calibration which depends on an accurate measurement of the voltage. Furthermore, a rather complicated algorithm is needed to assemble a complete fragment ion mass spectrum.

The effect of decreasing the mirror voltage is illustrated graphically in Figure 4-2. The curves are generated using the condition for minimum flight time, namely $\partial T/\partial v_o = 0$, where T is the total flight time of a parent ion and v_o is the initial velocity such that $v_o = \sqrt{2qV_a/m}$ = constant; in other words, v_o is the velocity of an ion after acceleration with zero initial velocity. See [6] for details of the calculation. For a single-stage mirror, by satisfying this condition, the flight time is independent of axial velocity to first order for parent ions of every mass, that is

$$T = \frac{L}{v_o}\left[2 + \left(\frac{\delta}{v_o}\right)^2 - \left(\frac{\delta}{v_o}\right)^3 + \ldots\right] \qquad (4\text{-}2)$$

where L is the total length of the field-free path and δ is the velocity deviation from v_o. The curves in Figure 4-2 were generated using Eq. (4-2) to second order assuming $L = 0.8\text{m}$ with a parent ion mass of $m_p = 1300\text{u}$. Thus the flight time has a parabolic dependence on the initial velocity deviation and the compensation occurs if the mean velocity is at the minimum of the parabola, that is, $\delta = 0$.

In the example of Figure 4-2, the target accelerating potential is $V_a = 10\text{kV}$, so

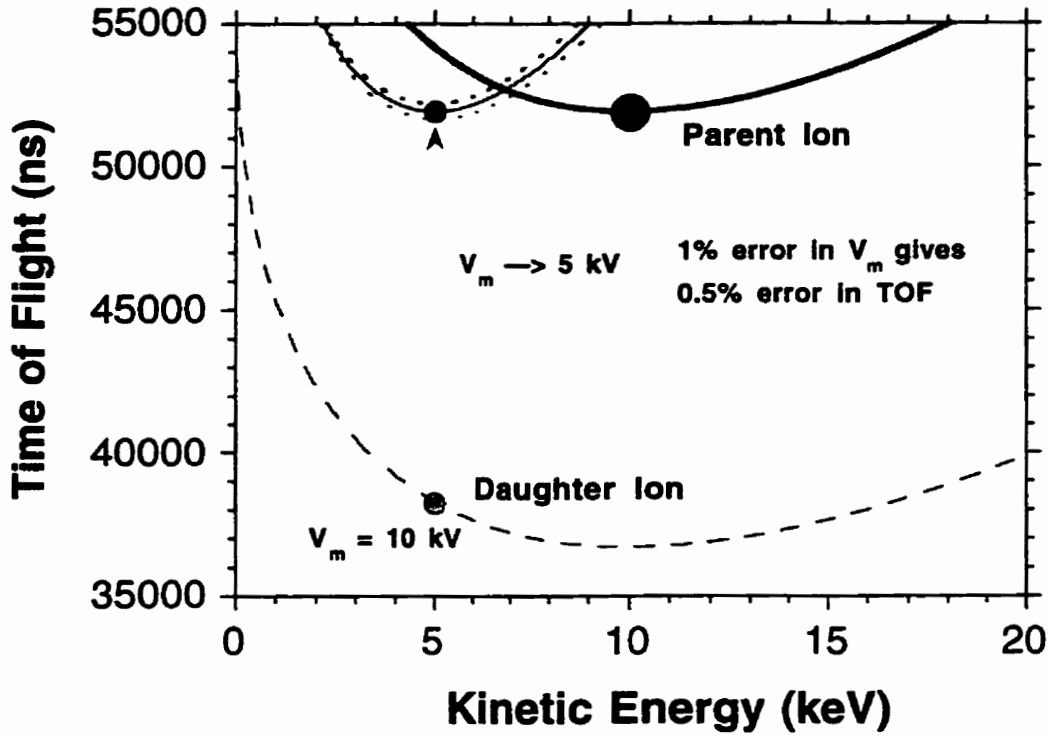

Figure 4-2: Theoretical flight times as a function of ion kinetic energy showing the effect of decreasing the mirror voltage. In this example, the target voltage is $V_a = 10\text{keV}$, and the daughter ion mass is $m_d = m_p/2$. See text for an explanation.

the parent ion acquires the full 10keV, and the mirror is optimized to correct for small variations in the initial velocity of the parent ion. In other words, the flight time is, to first order, insensitive to changes in the initial velocity. Thus the flight time of a 10keV parent ion falls at the minimum of the T versus kinetic energy (KE) curve. If the parent ion decays, say, as in this example, to a daughter ion of mass $m_d = m_p/2$, then the energy of the daughter ion is half the parent ion energy (not taking into account the relatively small amount of energy associated with the decay process) and thus the energy of the daughter ion is not optimum for the mirror. That is, small variations in the velocity of the daughter ion will appreciably effect the flight time. Decreasing the mirror voltage to optimize the

mirror for a 5keV ion, increases the flight time of the daughter ion (as it penetrates deeper into the mirror, as mentioned above) but places it at the bottom of the T versus KE curve and therefore provides focusing. This example also illustrates the sensitivity of the mirror voltage on the time-of-flight; a 1% change in the mirror voltage causes a 0.5% change in the flight time.

We have developed an alternative method which is the same in principle as the one describe above but has some practical advantages. Instead of leaving the target voltage constant, and acquiring spectrum segments for various *reduced* mirror voltages, the mirror voltage is left constant and spectrum segments are acquired for various *increasing* target voltages.

4.2 Proposed Method for Acquiring Daughter Ion Spectra

Under the initial conditions, with the mirror voltage set to V_m and the target set to V_a, the mirror is optimized for the parent ions with energy qV_a. Daughter ions, formed in the field-free region before the mirror, have energy $qV_a(m_d/m_p)$ which in general is rather far from the optimum. However, if the accelerating voltage is increased to the value V_a' given by

$$V_a' = V_a(m_p/m_d) \tag{4-3}$$

then daughters of mass m_d have the optimum energy qV_a for the mirror. This gives the daughter ions the same energy as prompt fragments (ions produced at the target) with the target at is initial voltage setting of V_a. Therefore the relationship between the mass of this particular daughter and its flight time is given by the original calibration giving in Eq. (4-1): $\sqrt{m_d} = a(t_d - t_o)$. Thus, when target voltage is increased from V_a to V_a' to bring the energy of a daughter ion to the optimum for the mirror, its flight time changes, moving the ion to its correct *m/z* value as predicted by the original calibration preformed with the parent ion spectrum. This means that the various segments of the time-of-flight spectra can simply be joined together, end to end, and the original calibration will be valid over the entire composite spectrum.

The effect of increasing the accelerating voltage is illustrated graphically in Figure 4-3. As in Figure 4-2, the curves were generated using Eq. (4-2), however the initial accelerating voltage was $V_a = 5\text{keV}$. The mirror voltage is optimized for parent ions of this energy, but is not for a daughter ion of, say, half the mass (thus, half the energy). By increasing the accelerating potential, in this case, to $V_a = 10\text{keV}$, the energy of the daughter ion is increased to 5keV, and so then the mirror is optimized for this species. This example also illustrates the relative insensitivity of the flight time on the accelerating voltage; a 21% change in the target voltage causes a 0.5% change in the flight time, whereas only a 1% change in the mirror voltag is required to cause the same 0.5% change in the flight time. Thus the flight time is about 20 times more sensitive to variations in the mirror voltage than to variations in the accelerating voltage, under optimum focusing conditions.

Just as when the mirror voltage is reduced, by increasing from V_a to V'_a, all parent ions, as well as daughter ions with masses larger than $m_p(V_a/V'_a)$ will pass through the mirror and not get reflected back because they have too much energy.

For a given segment of daughter ion masses close to m_d for a given increase in target voltage V'_a, the calibration applies exactly only for daughter ion of mass m_d as given in Eq. (4-3). For ions that deviate from the optimum ratio, a correction is still necessary, but this is small, and is applied to an accurately known calibration. The same sort of calibration is required within segments obtained with reduced mirror voltages, but then a new calibration must first be determined, and the correction must be applied to that.

Derivation of the Correction Applied to Each Segment

In a reflecting time-of-flight mass spectrometer with a single-stage ion mirror, for a given accelerating voltage V_a, there is a simple relationship between the total flight time T_d of the daughter ion of mass m_d and the total flight time T_p of its parent of mass m_p [6], which is

$$\frac{T_d}{T_p} = \frac{(m_p + m_d)}{2m_p} \tag{4-4}$$

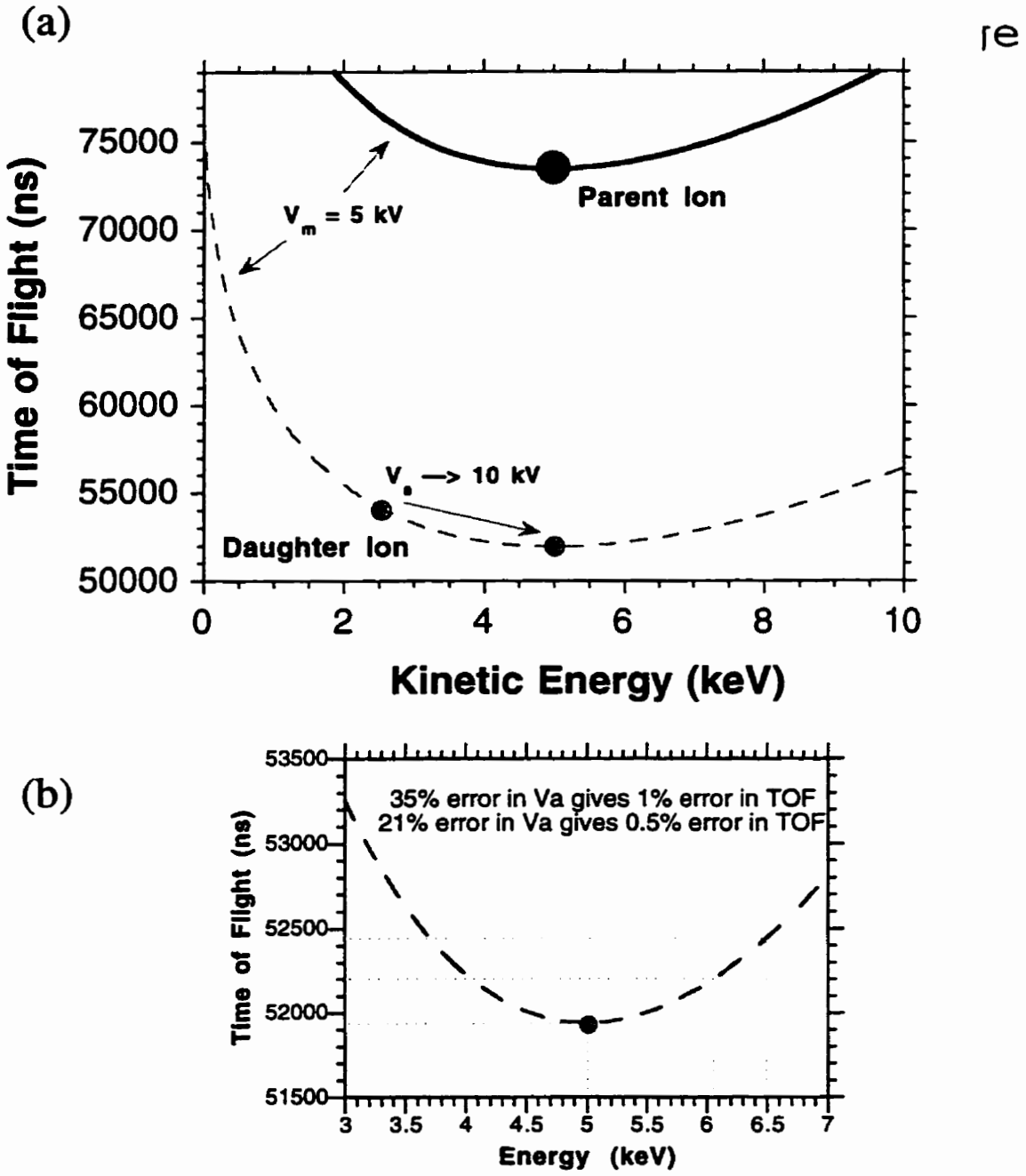

Figure 4-3: (a) Theoretical flight times as a function of ion kinetic energy showing the effect of increasing the target (accelerating) voltage. In this example, the target voltage is V_a = 5keV, and the daughter ion mass is $m_d = m_p/2$. See text for explanation. (b) the effect of small variations in the accelerating voltage on the flight time.

The correction Δm_d needed for the initial accelerating voltage V_a (the first segment of daughter ion peaks) is defined as the difference between the measured mass (as given by the original calibration in Eq. (4-1)) and the actual mass m_d:

$$\Delta m_d = a^2(t_d - t_o)^2 - m_d \tag{4-5}$$

Note that t_d is the measured (or "practical") flight time, and T_d is the true (or actual) flight time such that $T_d = t_d - t_o$, where t_o corresponds to some delay time constant in the electronics; similarly for the parent ion. Eq. (4-5) can be rewritten as

$$\Delta m_d = a^2(t_p - t_o)^2\left[\frac{(t_d - t_o)^2}{(t_p - t_o)^2}\right] - m_d \tag{4-6}$$

Thus, substituting in Eq. (4-4) gives

$$\Delta m_d = a^2(t_p - t_o)^2\left[\frac{(m_p + m_d)^2}{4m_p^2}\right] - m_d \tag{4-7}$$

However, from Eq. (4-1) we have $m_p = a^2(t_p - t_o)^2$, thus Eq. (4-7) becomes

$$\Delta m_d = \left[\frac{(m_p + m_d)^2}{4m_p}\right] - m_d \tag{4-8}$$

Expanding, the correction Δm_d for the initial accelerating voltage V_a (with the mirror optimized for the parent) is given as a quadratic equation in terms of m_d:

$$\Delta m_d = \left(\frac{1}{4m_p}\right)m_d^2 - \frac{1}{2}m_d + \frac{1}{4}m_p \tag{4-9}$$

When the target voltage is increased from V_a to V'_a so that

$$\frac{V'_a}{V_a} = \frac{m_p}{m'_d} \tag{4-10}$$

(as in Eq. (4-3)), the mirror is then optimized for m'_d and then Eq. (4-4) becomes

$$\frac{T_d}{T'_d} = \frac{m'_d - m_d}{2m'_d} \tag{4-11}$$

where T'_d is the flight time for m'_d with target accelerating voltage V'_a. Thus, subse-

quently, the correction Δm_d in Eq. (4-9) becomes

$$\Delta m_d = \left(\frac{1}{4m'_d}\right)m_d^2 - \frac{1}{2}m_d + \frac{1}{4}m'_d \tag{4-12}$$

Finally, substituting Eq. (4-10) into Eq. (4-12) yields

$$\Delta m_d = \left(\frac{V'_a}{4m_p V_a}\right)m_d^2 - \frac{1}{2}m_d + \frac{1}{2}\frac{V_a}{V'_a}m_p \tag{4-13}$$

Thus, for a given segment of daughter ion masses at an increased accelerating voltage V'_a , a daughter ion of mass m_d will be shifted by Δm_d (as defined in Eq. (4-5)) from the predicted mass m given by the original calibration $\sqrt{m} = a(t_d - t_o)$ of the parent ion spectrum; that is

$$\Delta m_d = m - m_d \tag{4-14}$$

A more useful version of Eq. (4-13) is obtained by substituting it into Eq. (4-14) and solving for m_d:

$$m_d = m_p\left(\frac{V_a}{V'_a}\right)\left[2\sqrt{\frac{m}{m_p}\left(\frac{V'_a}{V_a}\right)} - 1\right] \tag{4-15}$$

where the positive root was taken (as $m_d > 0$). The parent ion mass m_p is know from calibrating the parent ion spectrum, the ratio $(V'_a / V_a) \geq 1$ is easily determined for each increased target voltage V'_a and the measured daughter ion masses m within each segment spectrum defined by V'_a can now be used to find the correct mass m_d.

Precursor Ion Selection

To obtain useful metastable decay information from a mixture of peptides, such as, for example, an enzymatic digest of a protein, precursor ion selection is necessary. For this purpose, a Bradbury-Nielsen ion gate [8,9] was designed and built, along with the controlling electronics. Our proposed method of PSD analysis is demonstrated using precursor ion selection for a mixture of four peptides.

4.3 Experimental

A schematic diagram of the instrument is shown in Figure 4-1 on page 56. A pulsed nitrogen laser (ND337: Laser Science, Inc., Cambridge, MA, USA) is triggered by a clock running at about 2Hz (limited by the data handling of the transient recorder) and irradiates a sample through a 50cm focal length lens at about 77° to the normal. The samples are prepared according to the usual procedure for MALDI [10] using α-cyano-4-hydroxycinnamic acid (αCHCA) as the matrix, and deposited on a target substrate. Ions formed by the laser pulse are accelerated by the electric field between the substrate (target) at an electric potential V_a and a grounded grid (90% transmission), which is about 1cm in front of the target, and travel along a straight line until they enter an electrostatic mirror. At the entrance to the mirror there is another grounded grid and the opposite end of the mirror, about 30cm away, is at an electric potential V_m (normally a little greater than V_a). Ions are reflected through about 177° by the mirror and are detected by an ion detector. The total equivalent path length is about 2m. For details on this instrument and the ion optics of the mirror, see [6]. The shown apparatus, excluding the laser and the electronics is contained in a vacuum chamber operating at a pressure of 1μTorr or less.

The ions are detected at an electron converter coated with CsI; secondary electrons produced at the converter by the impact of ions are bent through 180° by a magnetic field to a chevron microchannel plate detector. The signal from the detector is suitably amplified by a preamplifier and recorded by a transient recorder, and transferred to a computer. Signals resulting from ions formed by several successive laser pulses are acquired and may be averaged to improve the signal to noise ratio.

The procedure to acquire a composite spectrum is as follows: An ordinary parent ion mass spectrum is first acquired using relatively low voltages, say $V_a = 5\text{kV}$, with the corresponding optimum value of the mirror voltage V_m (see below). This parent ion spectrum is then calibrated in the usual way. In this experiment, the mass of the parent molecular ion was known and used for calibrating, along with either some known, light weight, prompt fragment or some alkali ion peak.

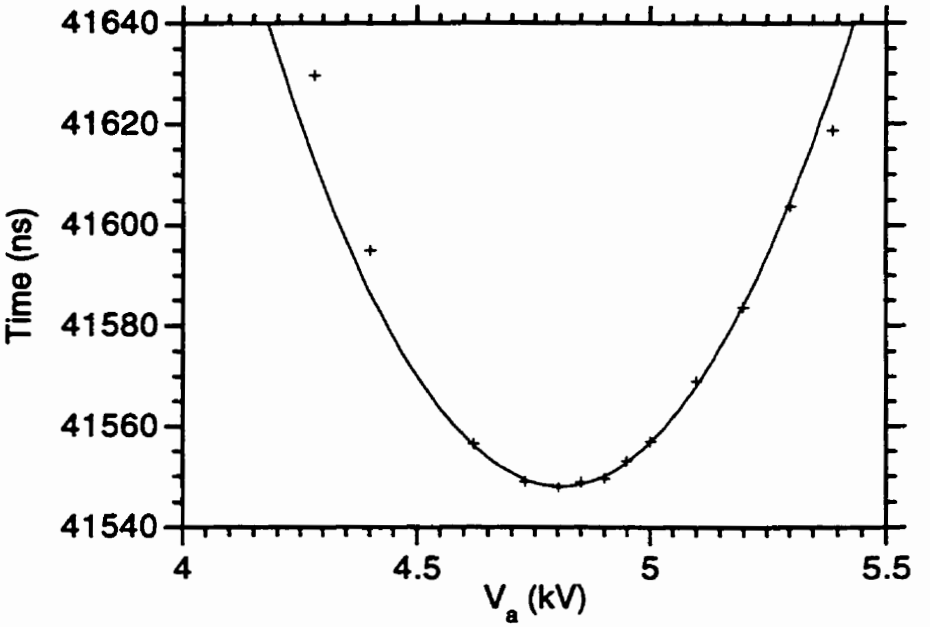

Figure 4-4: Plotting flight time of benzoperyline as a function of accelerating voltage, keeping mirror voltage fixed, thus finding the optimum ion kinetic energy for the ion mirror.

Next, a series of spectra are acquired for various increased values of the accelerating voltage V'_a . For example, good resolution over the entire mass range could be obtained with six spectra, each one run with about a 40% increase in the accelerating voltage over its value in the previous spectrum. The final target voltage would be $V'_a \approx 20\text{kV}$. The section (segment) of each spectrum near the daughter ion for which the mirror voltage is optimum, with masses close to $m_d = m_p(V_a/V'_a)$, is then cut out electronically and combined with similarly selected segments from other spectra for different V'_a .

An example of optimizing the ion mirror for velocity focusing is illustrated in Figure 4-4 using benzoperyline (117Da) as the molecular ion. The mirror voltage was set to $V_m = 5.60\text{kV}$ and then the accelerating voltage was varied, until a minimum in the flight time was found. For benzoperyline this occurred at $V_a = 4.81\text{kV}$. Thus the mirror is optimum for parent ions with $V_a = 4.81\text{kV}$. However, the minimum flight time is not obtained with the same value of V_a for which maximum resolution occurs, as shown in

Figure 4-5. The maximum resolution, in the case of LHRH with V_m = 5.16kV, occurs at about V_a = 5.0kV, 7% larger that where the minimum TOF occurs. This difference exists because variations in δ and variations in V_a contribute differently to the acceleration time. Regardless, for a given V_m, choosing the exact value for V_a for which the parent ion has the optimum energy for focusing is not critical because, as will be seen later, the ratio V_a/V'_a is determined empirically.

Bradbury-Nielsen Ion Gate

The procedure described above can be applied to a mixture of peptides by using precursor ion selection. The ion gate, shown in Figure 4-6, is similar in design to that used in [11]. It is placed at the entrance to the mirror (~50cm after the target) as shown in Figure 4-7(a). The ion gate consists of 50 parallel wires that are 0.1mm in diameter and spaced 1mm apart (90% transmission). The gate is normally closed with ±700V applied to alternate wires that are electrically isolated. The gate has an even number of wires in order to keep the gate electrically neutral on average; otherwise the flight time of the ions would be altered thus spoiling the calibration. Other important design parameters to minimize field penetration into the field-free region of the flight tube are to ensure uniform spacing of the wires and that the wires are in the same plane. From SIMION (a numcerical, ion-trajectory simulator program) calculations, for an ideal Bradbury-Nielsen ion gate, the electric field drops to negligible values at a distance from the plane of the ion gate on the order of the wire spacing.

When the gate is closed the ions passing through the gate are deflected as shown in Figure 4-7(b).The useful fragmentation of the parent ions in PSD occurs, as mentioned above, in the first field-free region between the grounded grid near the target and the grounded grid at the entrance to the mirror. When a parent ion decays in this region all the fragment particles have approximately the same velocity as the original parent (not taking into account the relatively small amount of energy involved with the ragmenting process). Thus, when the ion gate is closed and a parent ion removed from the spectrum, all the

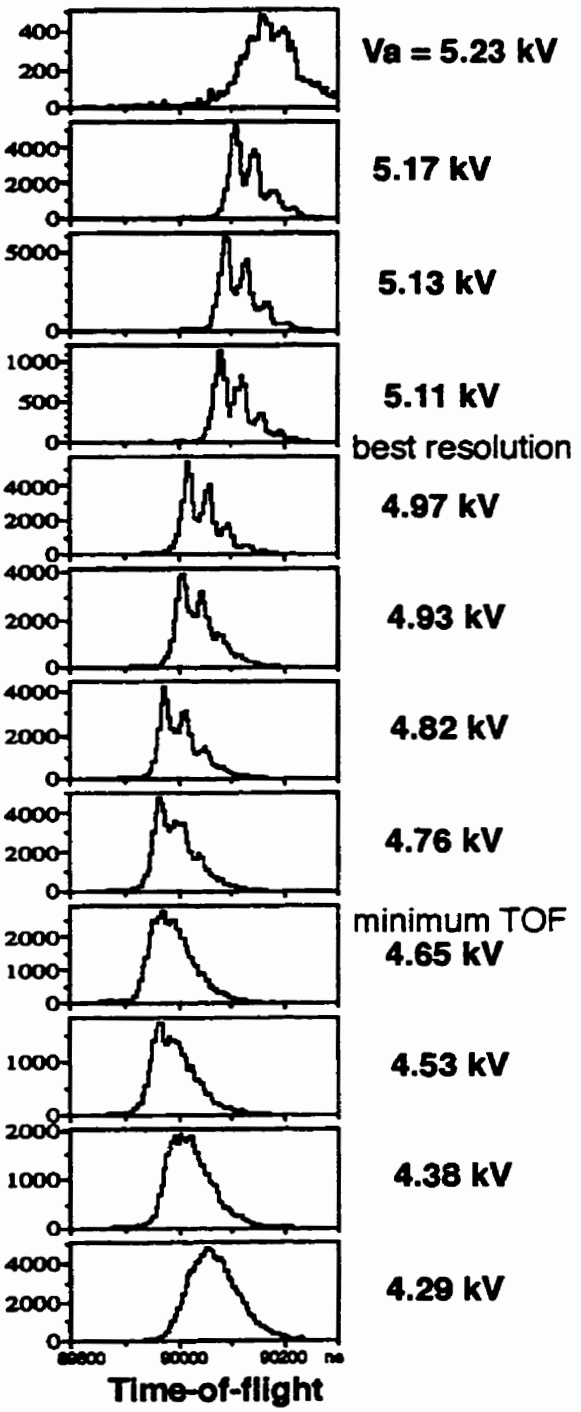

Figure 4-5: Optimizing the mirror with LHRH. Each TOF spectrum is for increasing accelerating voltage with the mirror voltage set at $V_m = 5.16\text{kV}$.

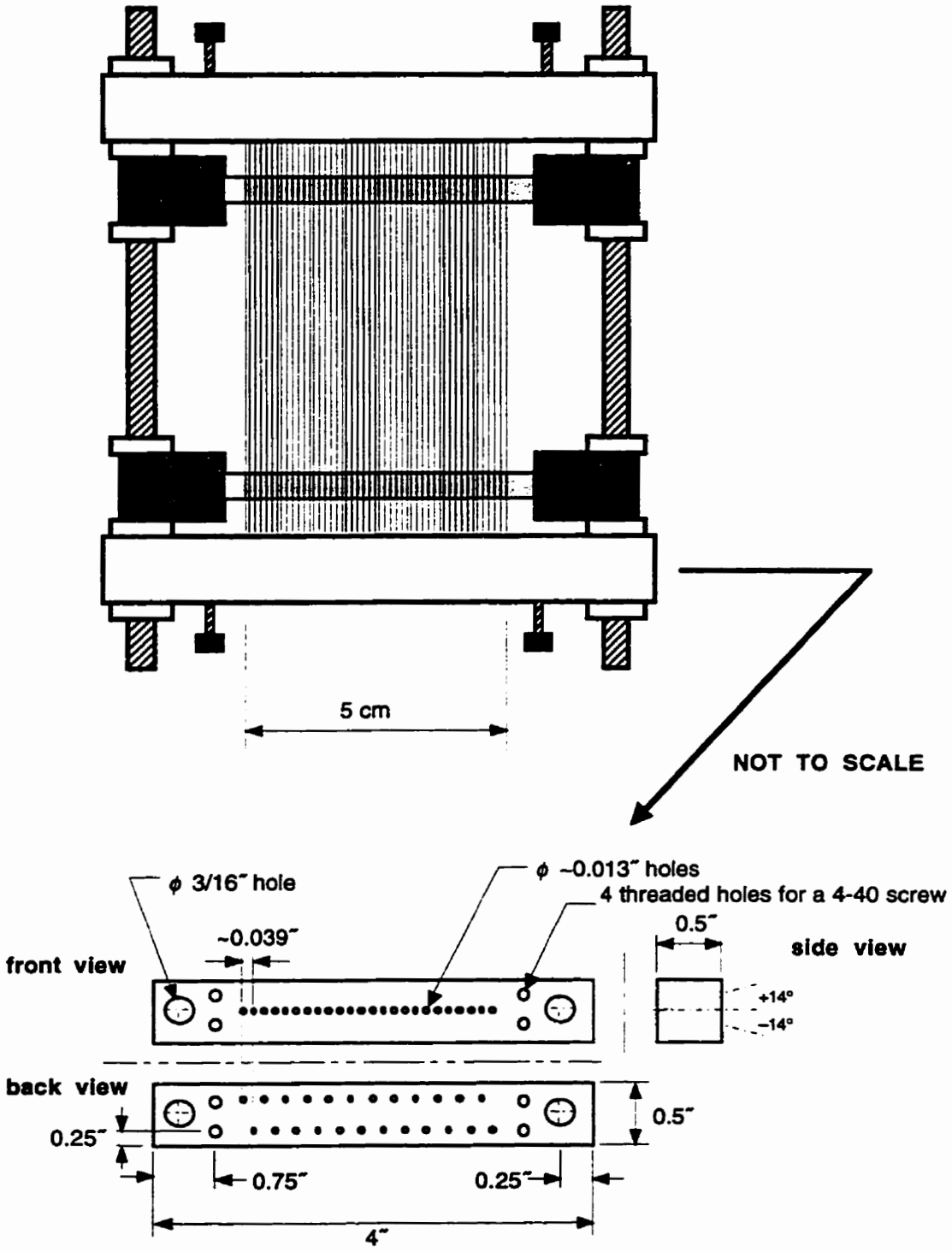

Figure 4-6: Schematic diagram of Bradbury-Nielsen ion gate designed and built.

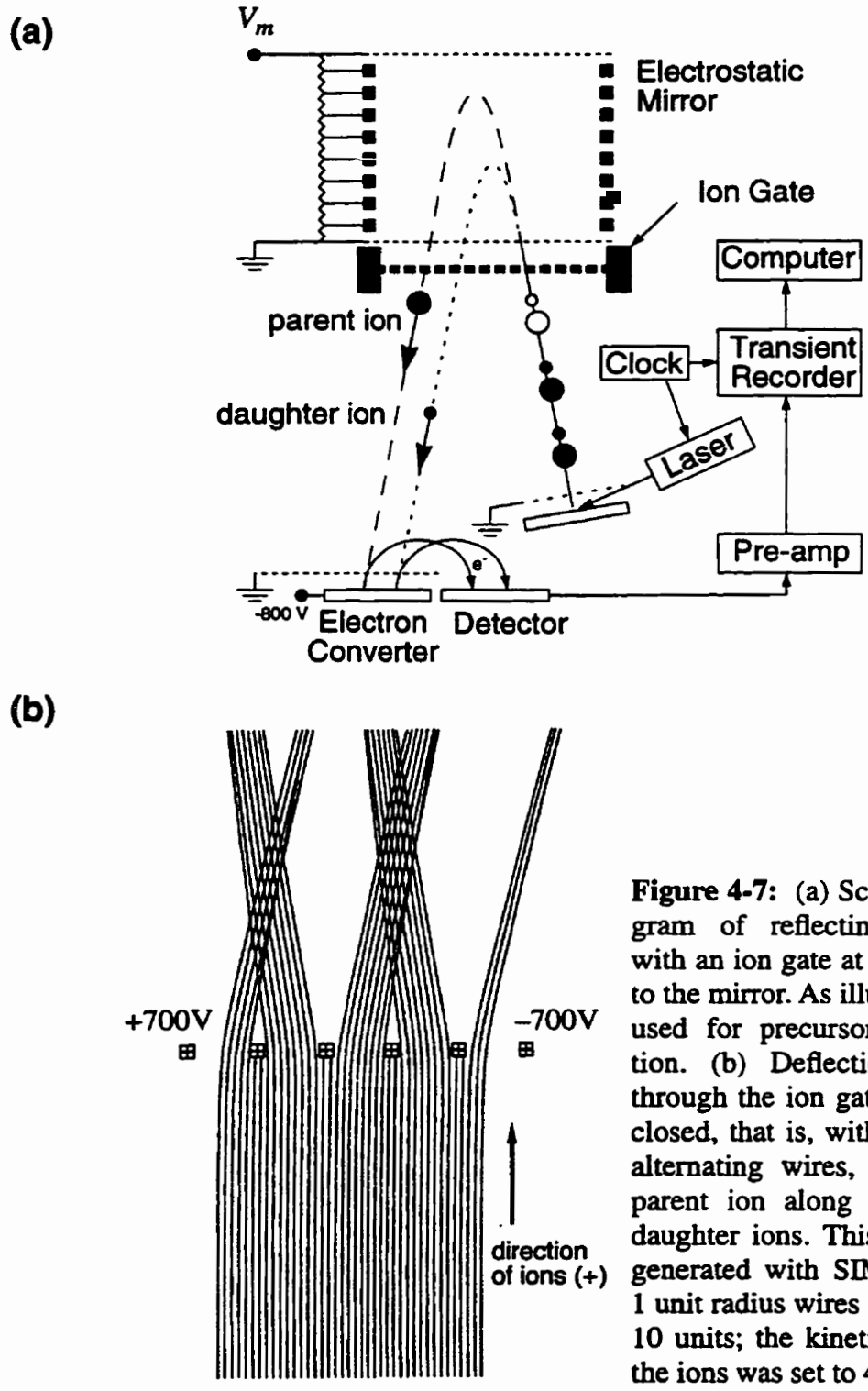

Figure 4-7: (a) Schematic diagram of reflecting TOF-MS with an ion gate at the entrance to the mirror. As illustrated, it is used for precursor ion selection. (b) Deflection of ions through the ion gate when it is closed, that is, with ±700V on alternating wires, removing a parent ion along with *all* its daughter ions. This figure was generated with SIMION using 1 unit radius wires separated by 10 units; the kinetic energy of the ions was set to 4keV.

daughter ions associated with this parent are removed as well, simultaneously.

To detect an ion in the reflecting TOF-MS with an ion gate, as shown in Figure 4-7(a), the gate needs to be pulsed open twice, first to allow the selected parent and all of its daughter ions into the mirror, and then again to allow the reflected ions out of the mirror. For example, to select only the parent ion, the gate must be opened once, say a time t, and again at $t + 2t$ (for a perfectly symmetric geometry) where $2t$ is the time spent in the mirror. See [6] for detailed calculations of flight times using a single-stage ion mirror. Since fragment ions spend less time in the mirror, to allow the passage of a desired precursor parent ion together with metastable fragments, say of some fraction α, of the mass of the parent ion, the gate must be opened once, at a time t, to allow the parent together with all the fragment ions into the mirror, and again at $t + 2t\sqrt{\alpha}$, where the gate is left open until the parent passes through at a later time $t + 2t$.

The usual geometry for precursor ion selection with PSD places the ion gate closer to the ion source where the gate only needs to be open once. The advantage of placing the gate further away from the ion source (at the entrance to the mirror) is that parent ions of different mass have greater spatial separation, thus allowing for improved precursor ion selection.

To use the gate with our proposed method for PSD analysis, as the accelerating voltage is increased, the time that opens, T_g, must decrease as $T_g = T_o\sqrt{V_a/V_a'}$ where T_o is the opening time for V_a.

Electronics for Ion Gate Control

Pulsing the ion gate open and closed is accomplished with two pulsers, one positive and one negative, each with two FET's (field effect transistors) arranged in a push-pull configuration. The two pulsing units, one for the positive set of wires and another for the negative wires, are shown in Figure 4-8 on page 72. To convert a positive or negative 700 V square pulse to a ±700 to ground pulse, as required, the pulsers are floated at ±700 V. Therefore the FET's were triggered by signals carried by optical fibres, which, in turn,

Positive-to-ground Pulser

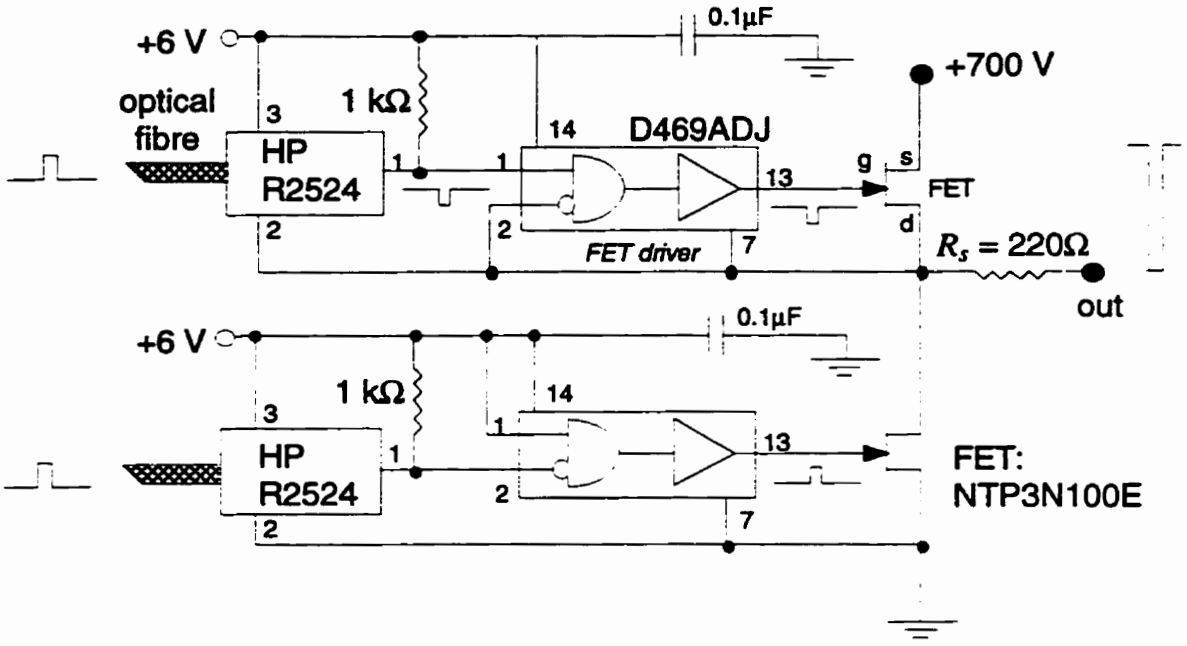

Negative-to-ground Pulser

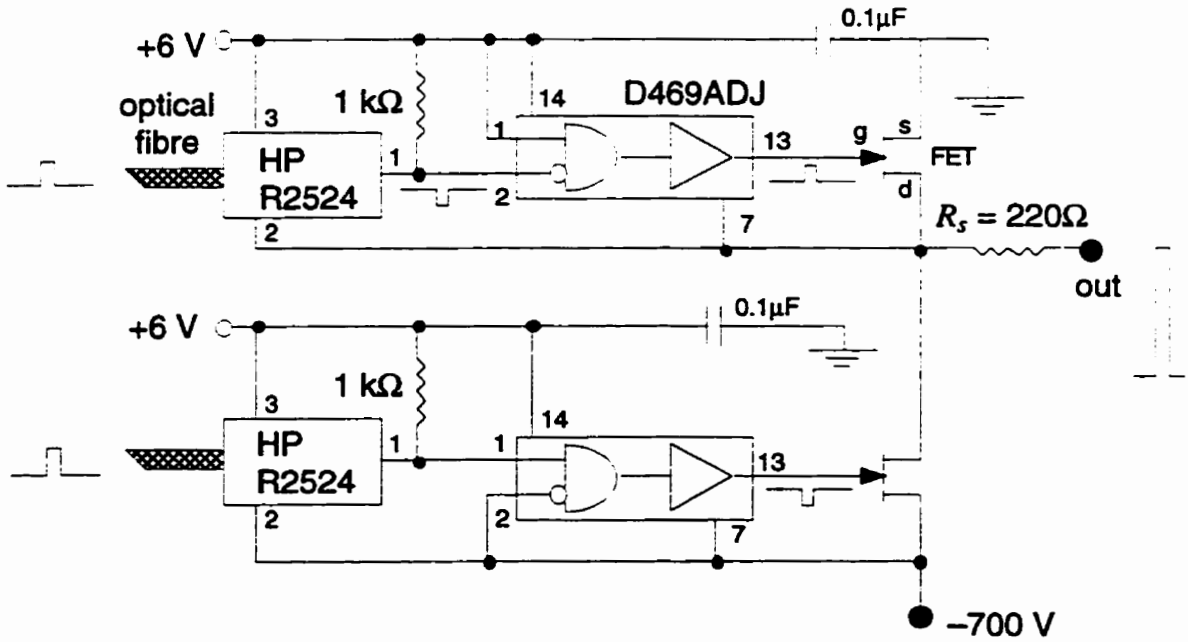

Figure 4-8: Electronic pulsers used to open and close the ion gate. When connected to the gate, opening edge of pulse is ~150ns and closing edge ~350ns.

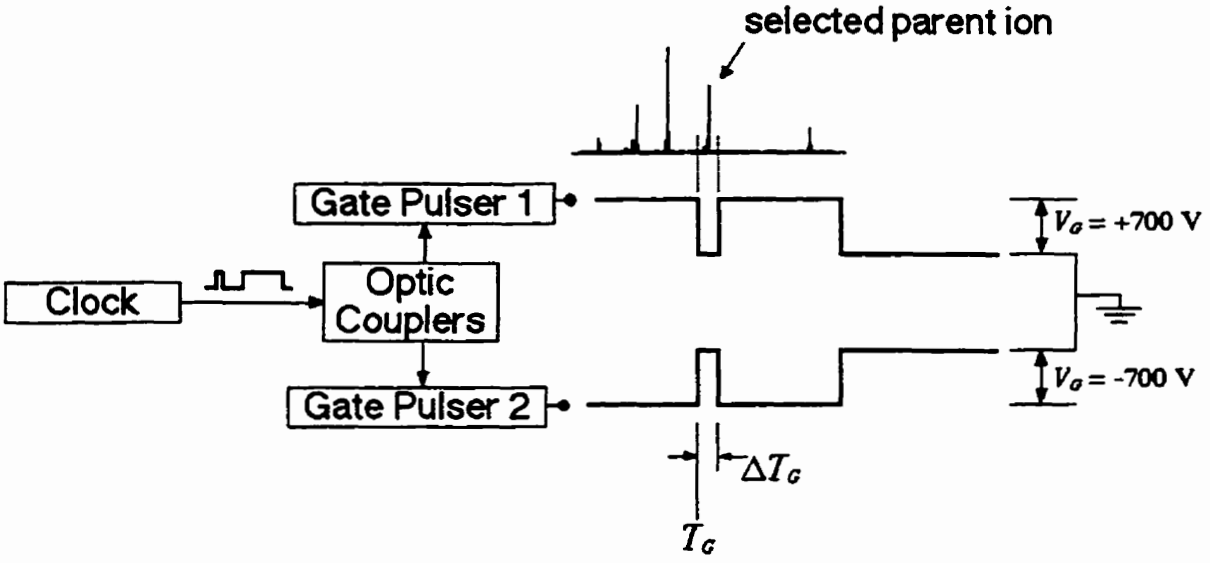

Figure 4-9: Ion gate control for selection a parent ion and its fragment ions.

were coupled to a digital-delay generator (the clock in Figure 4-7a) that controlled the timing of the gate. An example of controlling the gate is shown in Figure 4-9. An example of the selection resolution, which is ~60, is shown in Figure 4-10. The resolution is lower than what is normally quoted for such ion gates (which is around 90 [11,12,13]), however we are operating at much lower accelerating voltages than what is normally used and thus are mainly limited by the time spread of the ion packet (that is, the resolution). Furthermore, with improved electronics (pulse edges faster than a couple hundred nanoseconds) higher resolution would be achieved.

Recently Vestal *et al* [14] developed an ion gate consisting of two Bradbury-Nielsen ion gates in tandom; each gate is similar to the one described here. One advantage of this arrangement is that the opening and closing of the gate can be shared between two separate pulsers and it is much easier to produce a pulse with one sharp edge instead of two. Using this device, a resolution of ~1000 has been demonstrated.

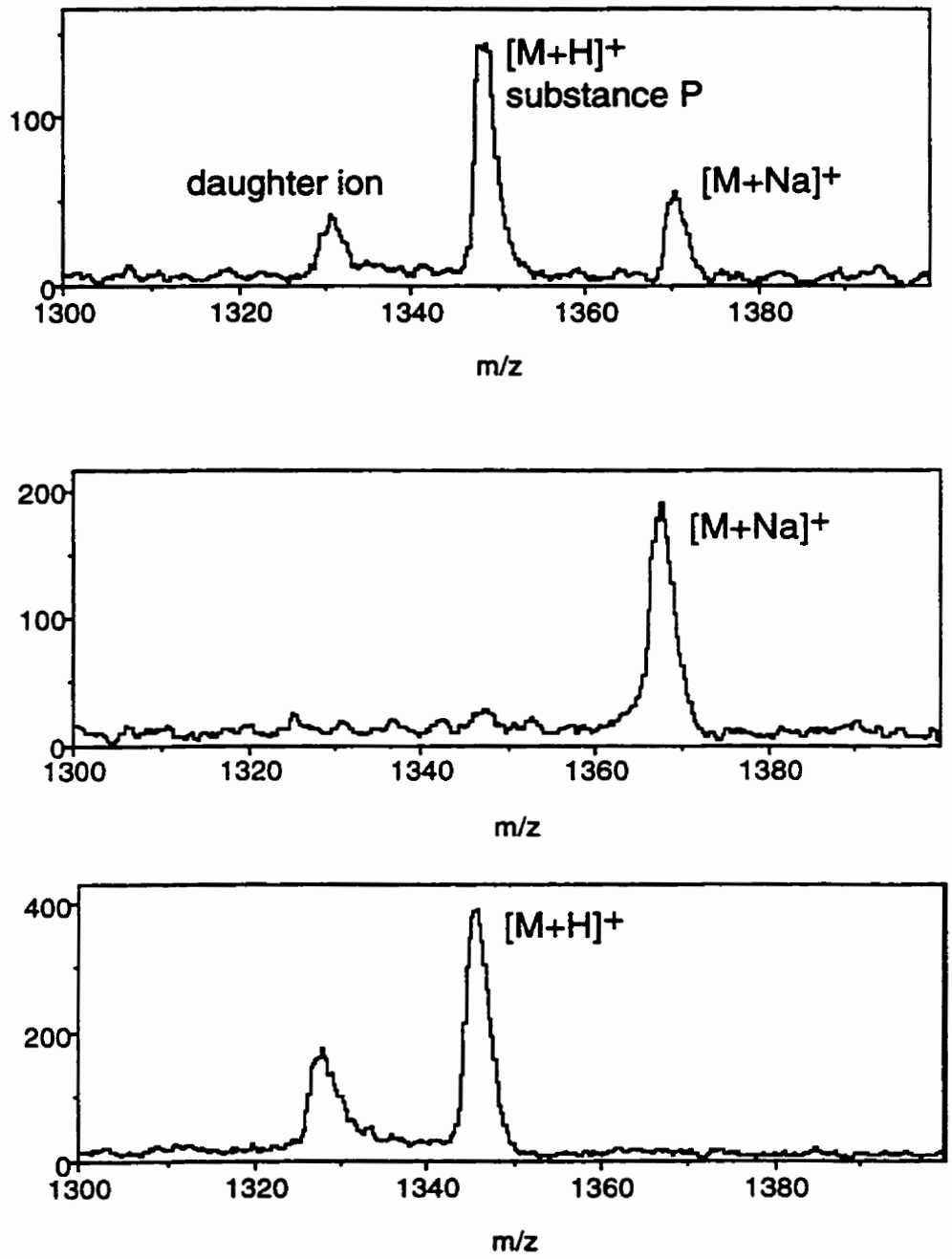

Figure 4-10: Using the ion gate to separate the $[M+H]^+$ for substance P from $[M+Na]^+$, demonstrating a selection resolution of ~60.

4.4 Results & Discussion

An example of our proposed technique for acquiring daughter ion spectra is illustrated in Figure 4-11 using the model case of substance P (1348Da) without using the ion gate for precursor ion selection. These time-of-flight spectra were acquired with a fixed mirror voltage of V_m = 5.60kV and various accelerating voltages V_a' . The top spectrum is the usual parent ion spectrum and is used for calibration. The next five spectra were taken with various increased values of V_a' , bringing different ranges (segments) of daughter ions near the optimum energy for the mirror. The bottom spectrum is the composite spectrum produced by combining the optimum segments from each of the spectra as indicated by the vertical dashed lines. These spectra are represented as integer arrays in computer memory, and the arrays are simply joined together; no further processing is necessary to produce the complete mass spectrum shown at the bottom of Figure 4-11. To a good approximation, for display and qualitative examination purposes, the parent ion calibration applies directly to this composite spectrum.

The resulting composite histogram can be handled in much the same way as an ordinary parent ion spectrum, that is, a linear mass scale can be calculated the same way and masses determined approximately (within a few mass units) using the calibration equation (Eq. (4-1)) directly. However, for a more accurate mass determination, the correction given in Eq. (4-13) (or, more appropriately, Eq. (4-15)) must be applied.

Even with Eq. (4-15) which gives the theoretical mass correction, there is still a systematic error in the correction predicted by this equation, probably because of imperfections in the mirror field. The systematic error can be accounted for by using effective values of the target voltage ratios, $(V_a' / V_a)_{eff}$, for each segment determined using the spectra for a known peptide such as substance P.

In this model case using substance P, mass assignment for each daughter ion was determined using the results of [7] and is compared against Δm_d calculated by Eq. (4-13) for the first four of the five segments in Figure 4-11, using the directly measured values for the ratios V_a' / V_a. This is shown if Figure 4-12. In Figure 4-13, Δm_d from Eq. (4-13) was

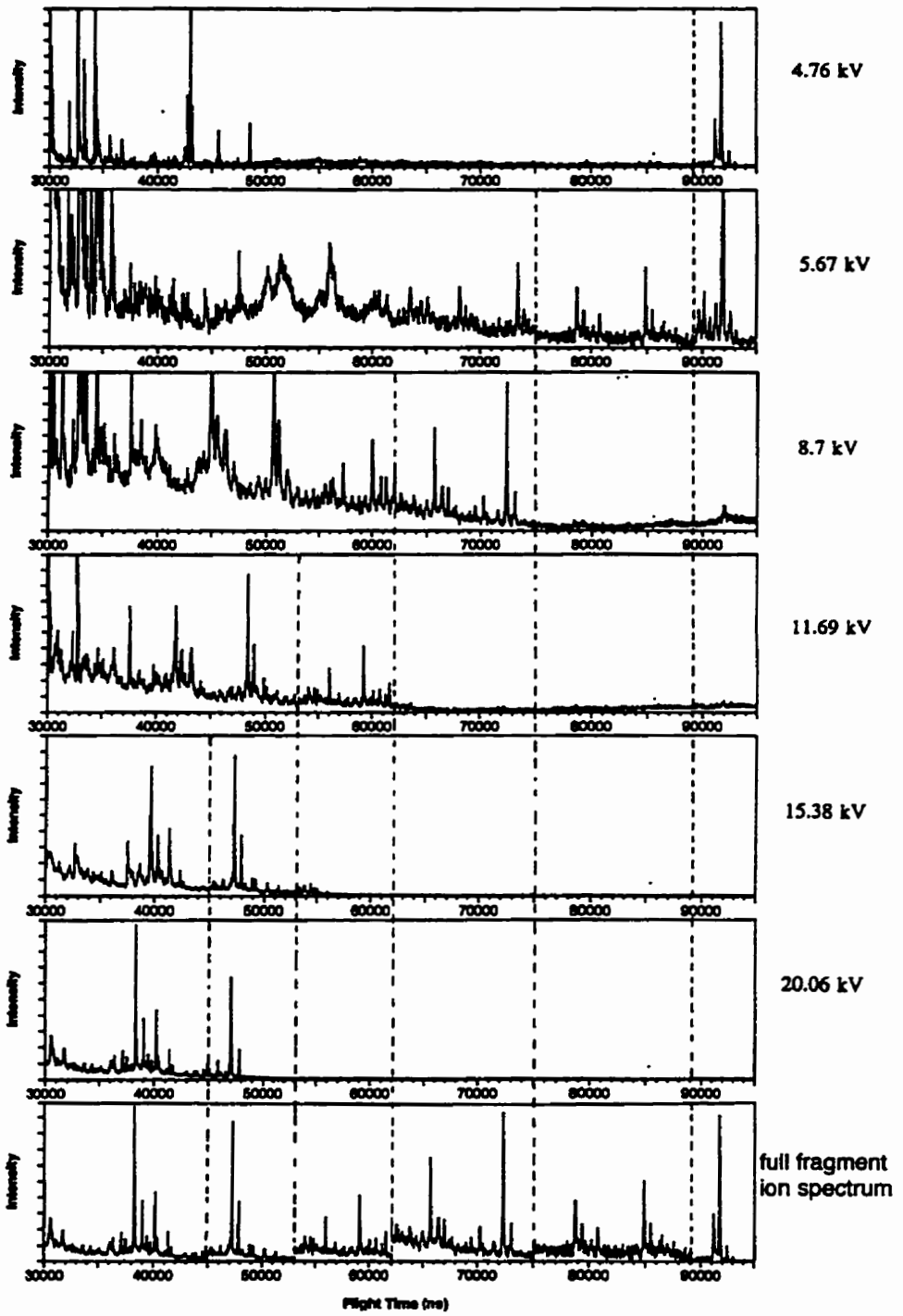

Figure 4-11: An example of our proposed method for accruing daughter ion TOF spectra using substance P (1348Da). Mirror voltage is 5.6keV and the accelerating (target) voltage is indicated for each segment.

$$\Delta m_d = \left(\frac{V'_a}{4m_p V_a}\right) m_d^2 - \frac{1}{2} m_d + \frac{1}{2}\frac{V_a}{V'_a} m_p \quad \text{Eq. (4-13)}$$

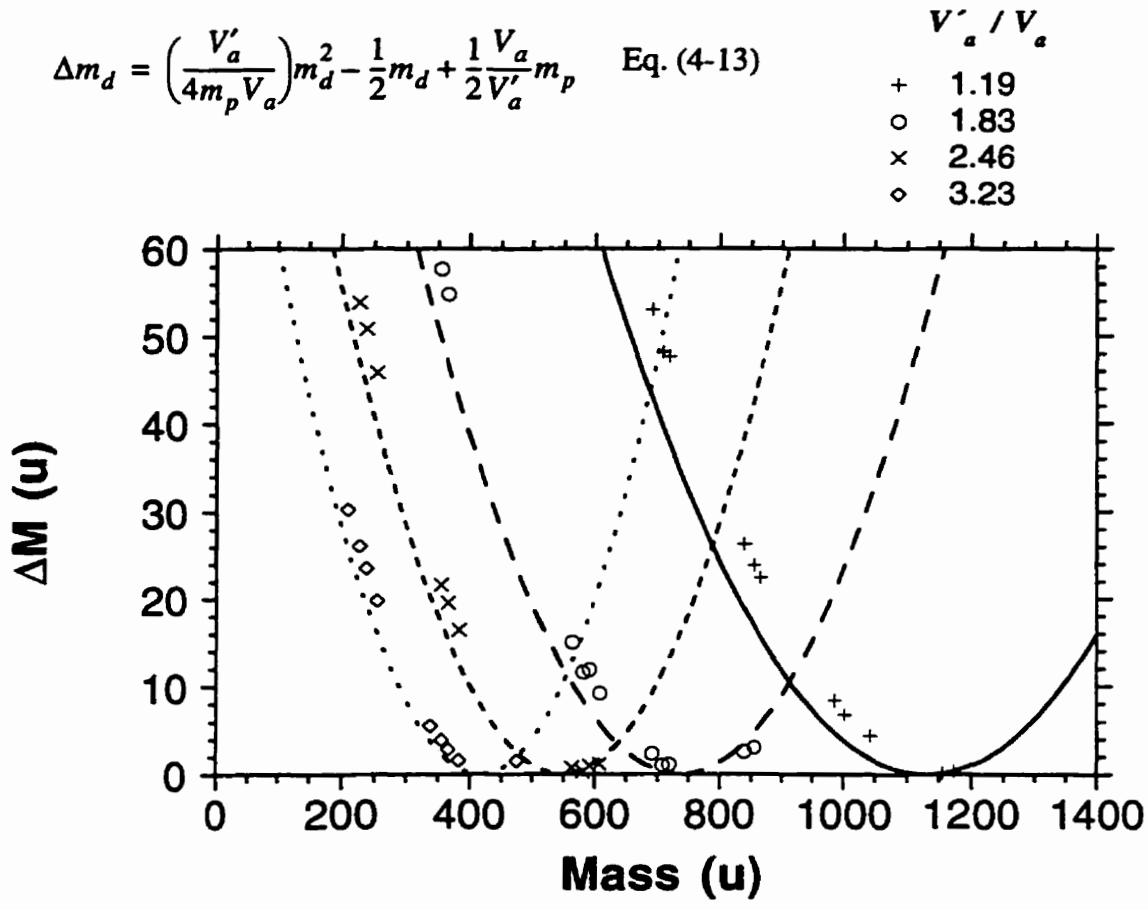

Figure 4-12: Difference between apparent and calculated fragment ion mass Δm_d versus the calculated (theoretical) fragment mass for substance P. The parabolas are the theoretical curves for Δm_d from Eq. (4-13) using the *measured* values for the accelerating potentials V_a and V'_a, where V_a = 4.6kV.

fit to the data with a parabola and then setting the minimum to of this parabola (that is, m_d) to the minimum of Eq. (4-13) (at $\Delta m_d = 0$) to the same value. That is, by adjusting V'_a / V_a, we shift the parabolas in Figure 4-12 so that their minimum values line up with those observed experimentally. There is about a 4% change between measured and effective ratios of V'_a / V_a. Analysing an unknown sample would, in the simplest case, require using the same voltage steps as used in Figure 4-11 and, thus, the same *effective* target voltage ratios $(V'_a / V_a)_{eff}$ in Eq. (4-15). However, as Figure 4-14 shows, a simple empir-

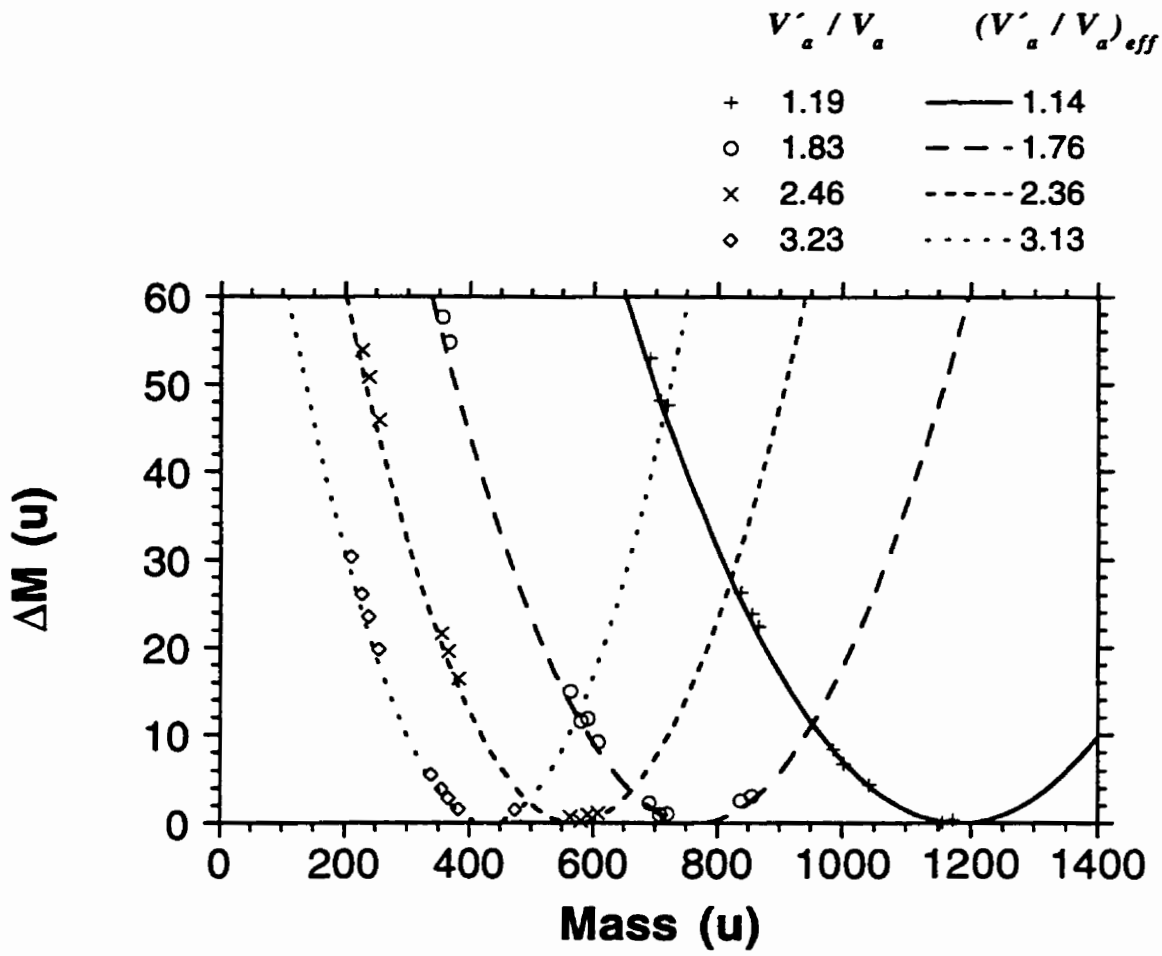

Figure 4-13: Difference between apparent and calculated fragment ion mass Δm_d fitted to the known fragments of substance P versus the calculated (theoretical) fragment mass for substance P. The parabolas are the theoretical curves for Δm_d from Eq. (4-13) using $(V'_a / V_a)_{eff}$ the *effective* values for ratios voltage ratios.

ical relationship was found between the measured target voltage ratios (V'_a / V_a) and the effective ratios $(V'_a / V_a)_{eff}$ determined using substance P. The relationship is

$$(V'_a / V_a)_{eff} = \frac{(V'_a / V_a)_{\text{meas.}}}{1.05 + 0.00695(V'_a / V_a)_{\text{meas.}}} \qquad (4\text{-}16)$$

The empirical correction determined from the substance P spectra can be used for analysis of other peptides. Figure 4-15 shows the daughter ion spectra for bradykinin (1060Da). Applying the correction from Eq. (4-15), using the effective target voltage

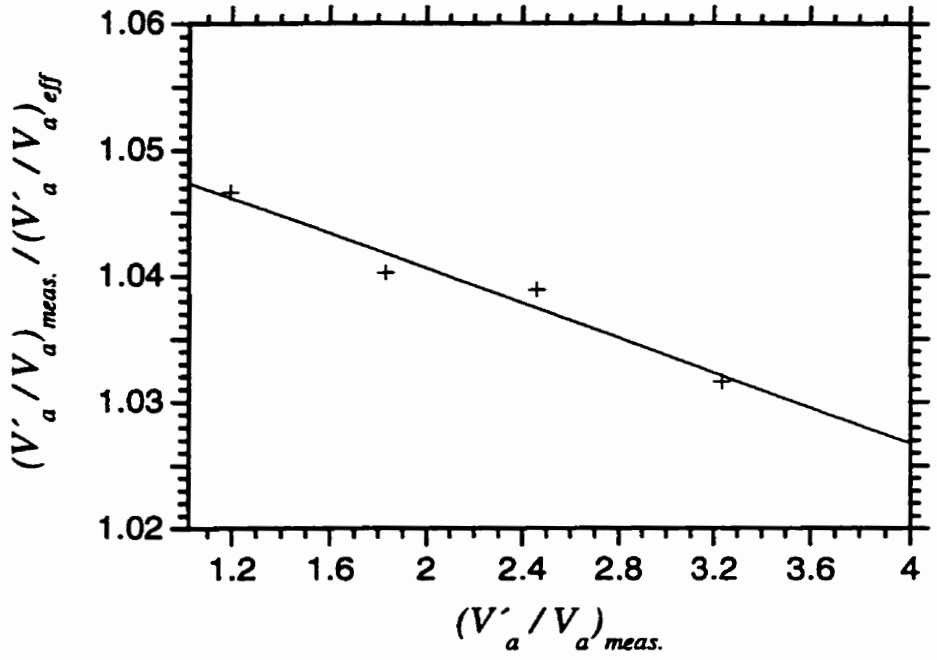

Figure 4-14: A simple empirical relationship between the measured target voltage ratios (V'_a / V_a) and the effective ratios $(V'_a / V_a)_{eff}$ determined using substance P.

ratios $(V'_a / V_a)_{eff}$ determined using Eq. (4-16), the corrected fragment ion masses of bradykinin are on average within ±0.5 Da from the calculated masses. The results for each of the five segments in Figure 4-15 are shown in Table 4-1. In Table 4-1 both the measured and effective ratios of the accelerating voltages are shown along with the corresponding daughter ions measured in each segment. The observed fragments are labelled according to the standard nomenclature of Roepstorff and Fohlmann [15] and of Johnson *et al* [16]. For the masses, the calculated (theoretical) mass of the fragment is given, along with the apparent mass measured directly from the spectrum and the corrected mass using Eq. (4-16) and Eq. (4-15). Finally the difference (error) in the corrected and calculated is shown.

Analysing a Peptide Mixture

To demonstrate the use of the Bradbury-Nielsen ion gate for analysing a mixture, four

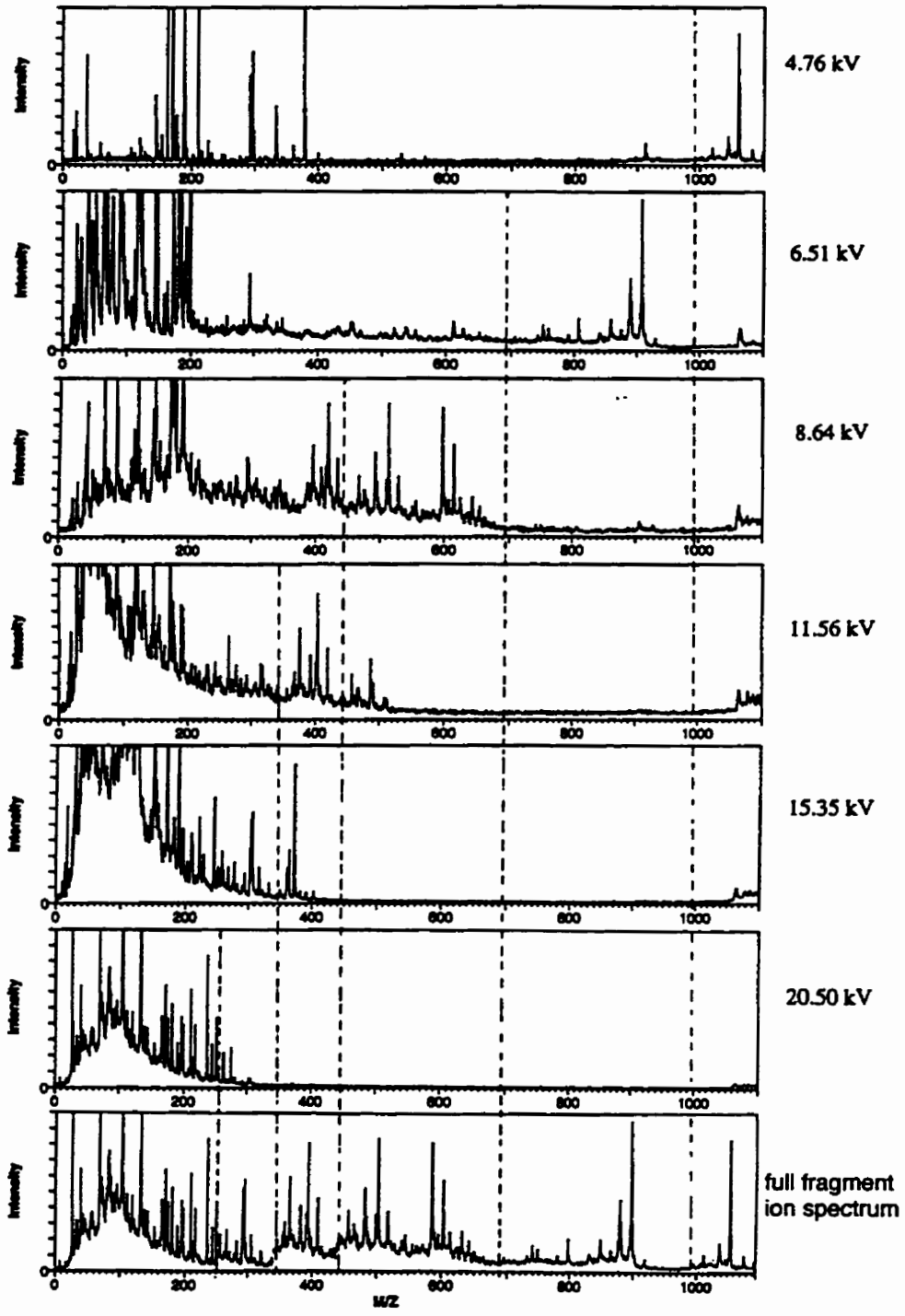

Figure 4-15: Acquiring daughter ion mass spectra for bradykinin (1060Da). Mirror voltage is 5.6keV and the accelerating (target) voltage is indicated for each segment.

	V_a/V_m		Daughter Ion Mass (Da)		Assignment &		Error in Daughter Ion Mass (Da)
	Measured	Effective	Apparent	Corrected	Calculated Mass (Da)		
	1.37	1.31	890.0	888.0	B8	887.0	0.9
	1.37	1.31	859.6	858.8	A8	859.0	-0.3
	1.37	1.31	843.0	842.6	A8-17	842.0	0.6
	1.37	1.31	740.8	739.4	B7	739.8	-0.4
	1.37	1.31	651.1	642.8	B6	642.7	0.1
1	1.37	1.31	635.4	625.2	B6-17	625.7	-0.5
	1.37	1.31	626.6	615.2	A6	614.7	0.5
	1.37	1.31	611.8	598.4	A6-17	597.7	0.7
	1.37	1.31	575.2	555.7	B5	555.6	0.0
	1.37	1.31	561.6	539.5	B5-17	538.6	0.9
	1.37	1.31	538.1	511.0	A5-17	510.6	0.4
	1.82	1.75	643.3	642.7	B6	642.7	0.0
	1.82	1.75	625.0	624.9	B6-17	625.7	-0.8
	1.82	1.75	614.7	614.7	A6	614.7	-0.1
	1.82	1.75	597.7	597.7	A6-17	597.7	-0.0
	1.82	1.75	556.1	555.0	B5	555.6	-0.6
2	1.82	1.75	530.0	527.5	A5	527.7	-0.2
	1.82	1.75	514.1	510.3	A5-17	510.6	-0.3
	1.82	1.75	410.2	391.2	B4-17	391.4	-0.3
	1.82	1.75	387.4	363.1	A4-17	363.4	-0.4
	1.82	1.75	364.8	334.4	B3-17	334.4	-0.0
	1.82	1.75	343.5	306.5	A3-17	306.4	0.1
	2.43	2.35	367.6	363.3	A4-17	363.4	-0.1
	2.43	2.35	318.0	306.4	A3-17	306.4	0.0
	2.43	2.35	276.1	254.7	B2	254.3	0.4
3	3.22	3.14	363.6	363.1	A4-17	363.4	-0.3
	3.22	3.14	306.0	305.2	A3-17	306.4	-1.2
	3.22	3.14	258.3	253.0	B2	254.0	-1.1
	3.22	3.14	245.6	238.3	B2-17	237.3	1.0
	3.22	3.14	222.6	210.6	A2-17	209.3	1.4
	4.36	4.28	253.9	253.9	B2	254.3	-0.4
	4.36	4.28	237.2	237.1	B2-17	237.3	-0.2
4	4.36	4.28	211.2	209.7	A2-17	209.3	0.5
	4.36	4.28	165.4	157.1	B1	157.2	-0.1
	4.36	4.28	143.0	128.7	A1	129.2	-0.5

Table 4-1: Summary of the results for bradykinin. The "Apparent Mass" values are from the original calibration, the "Corrected Mass" was calculated using the theoretical correction given by Eq. (4-15) along with the $(V_a' / V_a)_{eff}$ from Eq. (4-16) and the "Calculated Mass" is determined from amino acid sequence of the peptide.

peptides, bradykinin, LHRH, substance P and renin substrate tetradecapeptide were mixed together and placed on the target. Each peptide was selected for PSD analysis as shown in Figure 4-16. The PSD results for renin substrate selected from this mixture of four peptides are shown in Figure 4-17 and Table 4-2.

An obvious difficulty with this method is that it complicates precursor ion selection, since the gate time needs to be changed for every increment in the accelerating voltage V_a' . Since the selected parent ion is not detected for increased accelerating voltages (as it does not get reflected) and since the gate must be opened (for precursor ion selection) with accuracy of tens of nanoseconds, selection of ions for PSD analysis is difficult if they are separated by less than about 50Da.

Another limitation specific to our geometry but not the method of acquiring segments is in the placement of the ion gate, where it has to be opened twice to allow ions in and out of the mirror. The problem is in opening the gate for the second time for a relatively long duration (tens of μs). The individual electronic pulsing units (positive-to-ground and negative-to-ground) decay to ground at slightly different rates spoiling the symmetry and therefore the gate acquires a slight charge and affects the flight time of all ions. This can be seen by a closer inspection of Figure 4-10 on page 74. Even with a commercial pulser where the edges of the which pulse opens and closes the gates are much improved, there is still a different decay rate to ground, possibly due to slight differences in the loads for the two sets of wires in the ion gate. This problem could be easily fixed by using a much smaller ion gate (about 2.5cm) and placing it away from the mirror, closer to the target so that ions only need to pass though it once (and not twice, as in the current geometry).

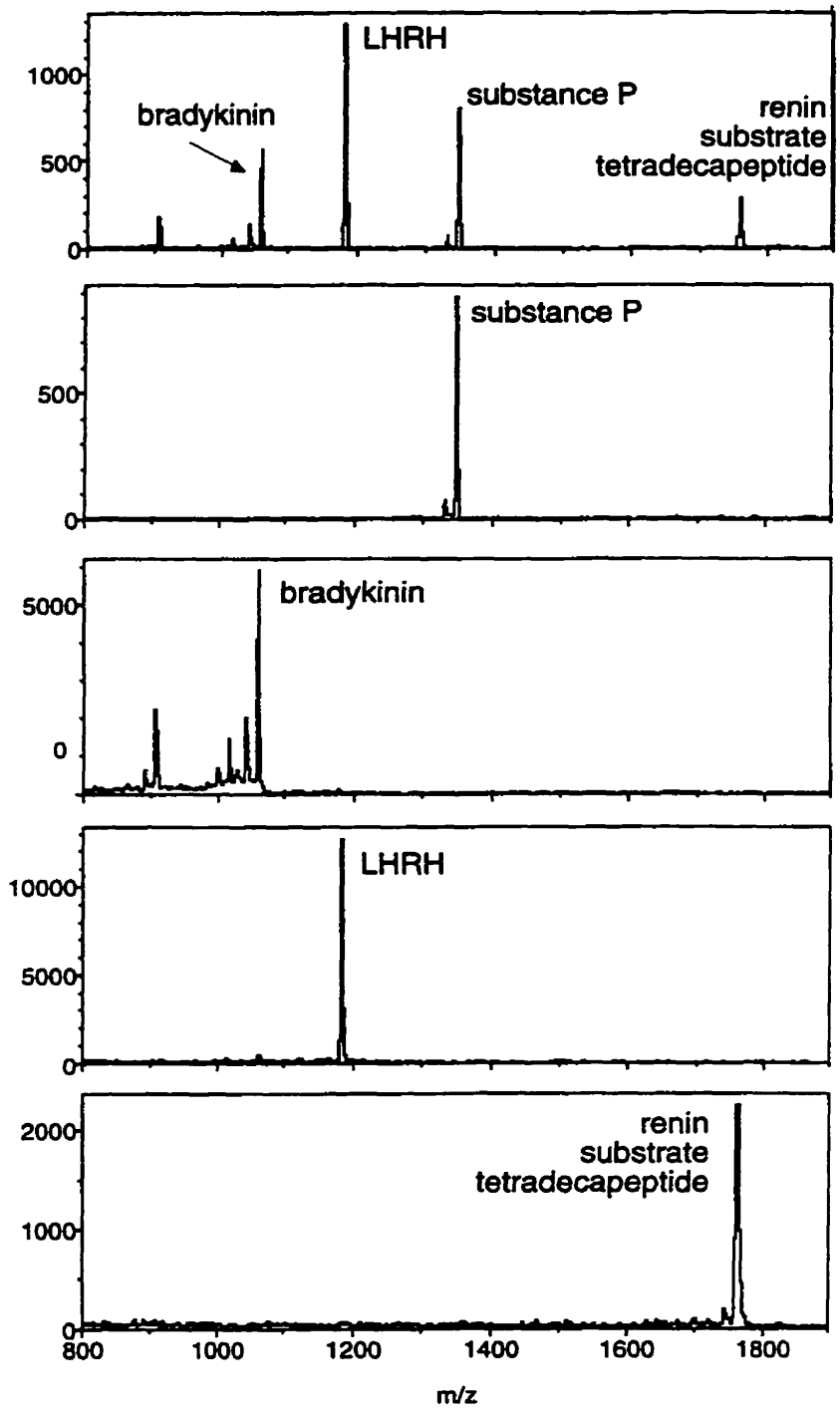

Figure 4-16: Precursor ion selection with a mixture of four peptides.

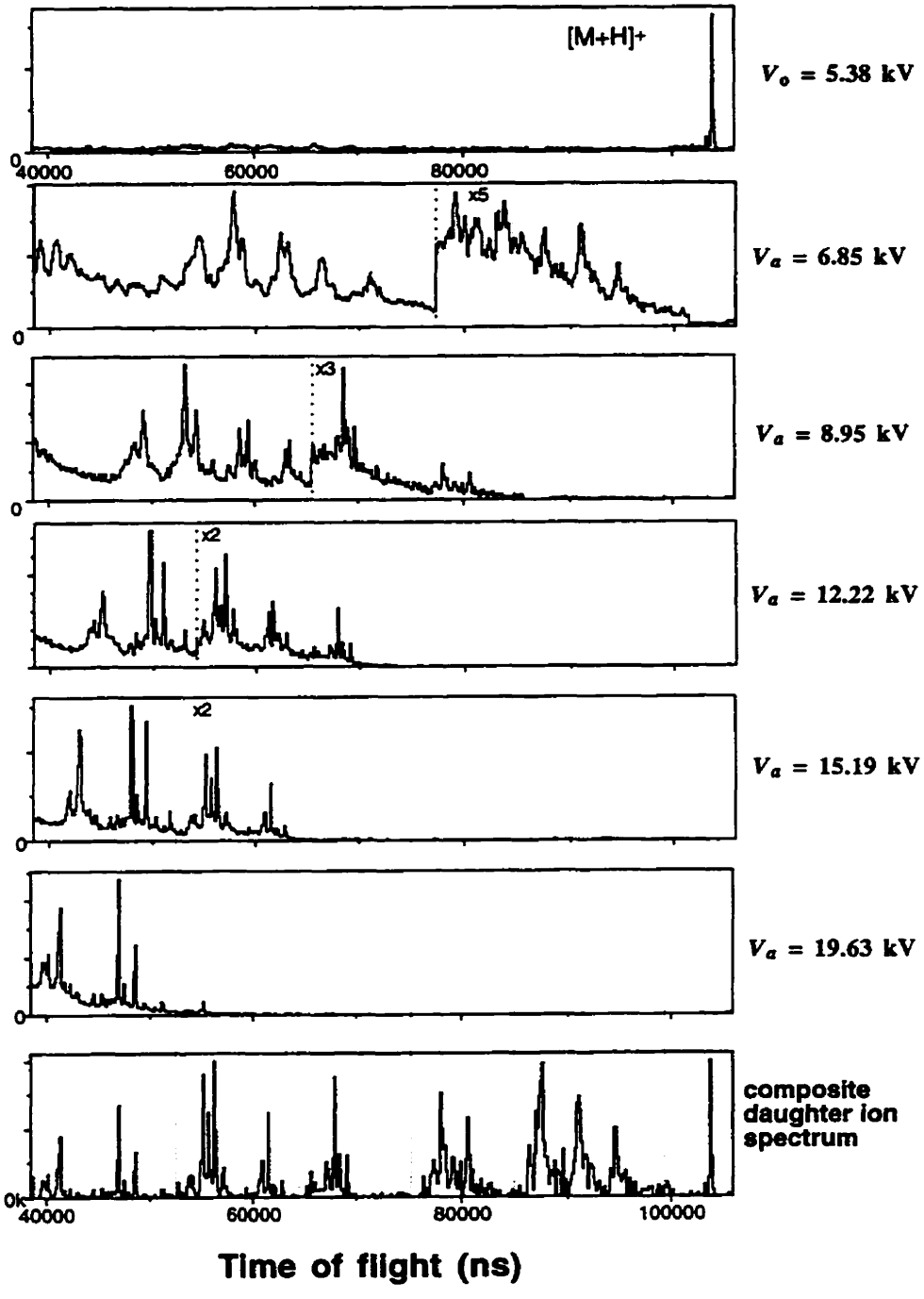

Figure 4-17: PSD analysis of renin substrate selected from a mixture of four peptides.

	V_a/V_m		Daughter Ion Mass (Da)		Assignment & Calculated Mass (Da)		Error in Daughter Ion Mass (Da)
	Measured	Effective	Apparent	Corrected			
	1.22	1.29	1465.1	1463.3	A12	1463.8	-0.5
	1.22	1.29	1253.2	1250.8	A10	1251.5	-0.6
1	1.22	1.29	1148.4	1139.1	A9	1138.3	0.8
	1.22	1.29	1132.6	1121.8	A9-17	1121.3	0.5
	1.22	1.29	1026.0	1001.9	A8	1001.2	0.7
	1.22	1.29	721.8	620.4	A5	619.7	0.6
	2.27	2.38	785.3	784.6	B6	784.9	-0.3
	2.27	2.38	767.4	767.1	B6-17	767.8	-0.7
	2.27	2.38	756.5	756.4	A6	756.9	-0.5
2	2.27	2.38	649.5	646.7	B5	647.7	-1.1
	2.27	2.38	624.1	619.3	A5	619.7	-0.4
	2.27	2.38	548.9	534.9	B4	534.6	0.3
	2.27	2.38	534.7	518.3	B4-17	517.5	0.8
	2.27	2.38	525.0	506.9	A4	506.6	0.3
	2.82	2.93	648.2	647.3	B5	647.7	-0.5
	2.82	2.93	631.6	631.2	B5-17	630.7	0.5
	2.82	2.93	619.7	619.5	A5	619.7	-0.2
	2.82	2.93	535.4	533.5	B4	534.6	-1.0
3	2.82	2.93	519.9	517.0	B4-17	517.5	-0.5
	2.82	2.93	509.4	505.7	A4	506.6	-0.9
	2.82	2.93	379.5	354.3	B3-17	354.4	-0.1
	2.82	2.93	357.9	326.7	A3-17	326.4	0.3
	2.82	2.93	317.2	272.4	B2	272.3	0.1
	2.82	2.93	304.9	255.3	B2-17	255.2	0.1
	3.65	3.65	377.9	371.5	B3	371.4	0.1
	3.65	3.65	363.0	354.5	B3-17	354.4	0.2
	3.65	3.65	353.5	343.5	A3	343.4	0.1
4	3.65	3.65	338.8	326.2	A3-17	326.4	-0.2
	3.65	3.65	294.4	271.3	B2	272.3	-1.0
	3.65	3.65	261.3	227.7	A2-17	227.2	0.4

Table 4-2: PSD results for renin substrate selected from a mixture of four peptides. The "Apparent Mass" values are from the original calibration, the "Corrected Mass" was calculated using the theoretical correction given by Eq. (4-15) along with the $(V_a' / V_a)_{eff}$ from Eq. (4-16) and the "Calculated Mass" is determined from amino acid sequence of the peptide.

4.5 Conclusion

We have developed an alternative method of acquiring PSD spectra which is the same in principle as the usual method but has practical advantages. Instead of leaving the target voltage constant, and acquiring spectrum segments for various *reduced* mirror voltages, the mirror voltage is left constant and spectrum segments are acquired for various *increasing* target voltages. The central advantage results from the fact that the flight time and therefore the calibration depends sensitively on the mirror voltage but only weakly on the target voltage, and therefore accurate measurements of the voltages is not necessary. Further advantages of the proposed method is that a single calibration is approximately applicable over the whole mass range, where only small corrections to this calibration are needed; and a full fragment ion spectrum can be assembled simply by joining end-to-end the time-of-flight histogram segments for each different increased accelerating voltage.

CHAPTER 5

ION YIELD VS LASER FLUENCE

Dependence of Ion Yields on Laser Fluence in Matrix-Assisted Laser Desorption/Ionization

5.1 Introduction

Matrix-assisted laser desorption/ionization (MALDI) was introduced in 1987 [1,2]. Since then, MALDI has become an important tool in the study of large molecules but the physical processes involved in the desorption event are still not well-understood. To help develop a quantitative model it is essential to determine the dependence of the number of desorbed particles on laser fluence, particularly for low fluence in the range of the observed detection threshold. The term "threshold" is commonly used in MALDI to refer to the fluence (energy per unit area per pulse) or irradiance (power density during the pulse) above which a single laser shot produces an observable signal using analog detection methods with a transient recorder. Whether a true threshold in the physical process exists, or whether the observed threshold is simply a result of limitations in the measurement methods has remained uncertain.

If the observed threshold results from the limited signal-to-noise ratio obtained from single laser shots using analog detection methods, then it is difficult to determine whether a true physical threshold for desorption exists at the same or some lower fluence using the same detection method. For this reason, Ens *et al* in Manitoba investigated several properties of MALDI using pulse-counting methods with a time-to-digital converter

[3]. The authors interpreted their results as evidence for a true irradiance threshold near $2 \times 10^6 W/cm^2$. Above this threshold the ion yield was found to have a slope between 4 and 6 on a log-log plot.

The dependence of the ion yield on laser fluence in MALDI was subsequently measured in Münster by Dreisewerd *et al* [4]. The Münster experiment introduced several improvements in the optics compared to the Manitoba experiment: (i) To separate the effects of beam spot-size and laser fluence, they used a fibre-optic to produce a flat-top laser profile, rather than the gaussian or near-gaussian profile obtained with standard optics. Increasing the fluence when the profile is gaussian, as was the case in the Manitoba experiment, will not only result in an increased local irradiance, it will also increase the total area of substantial ion emission. Indeed, a steep dependence of the yield on fluence would be observed from this increase in area alone, if the yield per unit area is a simple step-function at some threshold [5]. (ii) Secondly, the laser energy was monitored for each laser shot, and the measurement was carefully calibrated to get an accurate absolute fluence measurement. (iii) Finally, a much smaller step-size was used for the fluence: 0.1% instead of 8% as was used in the Manitoba experiment.

The Münster results show no evidence for a true fluence threshold. However, in spite of the above improvements in the optics, the measurements were made from single laser shots using analog detection. Thus, although an accurate measure of the absolute fluence was not available for the earlier Manitoba experiment, it is likely that it had probed a lower fluence range by using pulse-counting detection, and the possibility remained that this difference accounted for the observed threshold in the Manitoba results.

In this experiment, continuing measurements started at Münster [6], we combine the improved optical configuration introduced by the Münster group, with pulse-counting detection as well as analog detection in the same instrument to establish the relative fluence in the two types of measurement, and to make more detailed yield measurements in the low fluence range. Both methods of data acquisition have limitations in the usual axial TOF geometry. The analog measurements are limited at low fluence by detector noise and

at high fluence by detector saturation. The pulse-counting measurements are enabled by reducing the ion transmission; they are difficult to interpret because it is difficult to be certain that only individual ions are detected, especially at high fluence. Therefore we have also made measurements in an orthogonal-injection MALDI/TOF instrument with collisional cooling [7]. This new instrument enables pulse-counting over a much wider fluence range, without ambiguity as to the number of ions striking the detector.

5.2 Experimental

This experiment was performed on two different instruments. The first instrument is a standard, linear time-of flight (axial TOF) mass spectrometer where both pulsed-counting and analog measurements were performed. The second instrument is an orthogonal-injection MALDI/TOF with collisional cooling and pulse-counting detection.

5.2.1 Optics

The optical arrangement was the same for all of the experiments. The target was irradiated with a N_2 laser (ND337: Laser Science, Inc., Cambridge, MA, USA) with a wavelength of 337nm and a pulse duration of about 3 ns. To achieve a flat-top distribution of energy on the target, a fiber-optic arrangement was used, similar to the one described and characterized by Dreisewerd *et al* [4]. The laser beam is coupled into a 4 m long, high-temperature fiber (F-MCC-T: Newport, Mississauga, ON, Canada) with a 50mm focal-length lens. The dimensions of the fiber are shown in Figure 5-1. A homogeneous intensity profile at the other fiber end face is formed because of multiple reflections of the laser beam inside the fiber. The surface of the fiber tip is then imaged 1:1 onto the target by two identical planoconvex lenses (f = 15cm) arranged in infinite conjugation.

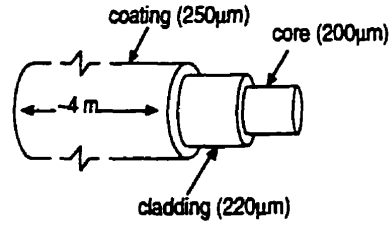

Figure 5-1: Dimensions of fiber optic (NA = 0.22).

Efficient coupling of the laser into the fiber requires a high quality surface at the

fiber tip, and careful positioning of the tip relative to the lens. The fibre was cleaved with a commercial fiber cleaver (CT-02: Fujikura, Japan). This device places the fiber under tension, scribes it with a diamond blade perpendicular to the axis, and then pulls the fiber apart to produce a clean break. Before cleaving, the protective coating around the core is removed with a small wire stripper (103-s: Diamond Xcelite, USA).

The diameter of the focused laser beam spot, d, is given by $d \approx \varphi f$, where φ is the angular divergence of the laser beam (~0.3 mrad) and f is the focal length of lens. For the 50mm focal-length lens coupling the laser beam to the fiber, this gives $d \approx 15\mu m$, considerably smaller than the 200 μm core diameter of the fiber. The end of the fiber is mounted in a chuck and positioned with an x, y, z-adjustable stage just outside the focal point of the lens. Special care has to be taken not to place the fiber tip exactly at the focal point of the lens, to avoid damage to the surface which decreases transmission.

The efficiency of transmitting the laser beam from the fiber to the sample-target is determined mainly by the numerical aperture of the fiber and the size and focal length of the output lens. The numerical aperture is the sine of the half-angle of the fiber acceptance or emission angle. The fiber used in these experiments has a numerical aperture of 0.22, corresponding to an open angle of about 26°. The first output lens has 15 cm focal length and is 2.5cm in diameter. The fraction of the beam area that strikes the lens is therefore only about 13%. For the measurements in the orthogonal TOF, the fiber-end along with the two 15cm lenses arranged in infinite conjugation, are contained within a tube, as shown in Figure 5-2. This allows for convenient focusing of the beam. In either case, the overall transmission of the fiber-optic configuration, taking account of all losses, is about 10%.

The laser beam fluence, defined as energy per unit area per pulse, is controlled by a circular gradient neutral density disk. The fluence is monitored in the axial TOF measurements by placing a quartz beam splitter between the two 15 cm focal-length lenses. In the orthogonal TOF measurements, a reflection from the quartz window (which admits the laser beam into the spectrometer) is used to monitor the fluence. Approximately 7% of the laser beam is reflected onto a pyroelectric detector (420: Eltec Instruments Inc., Daytona

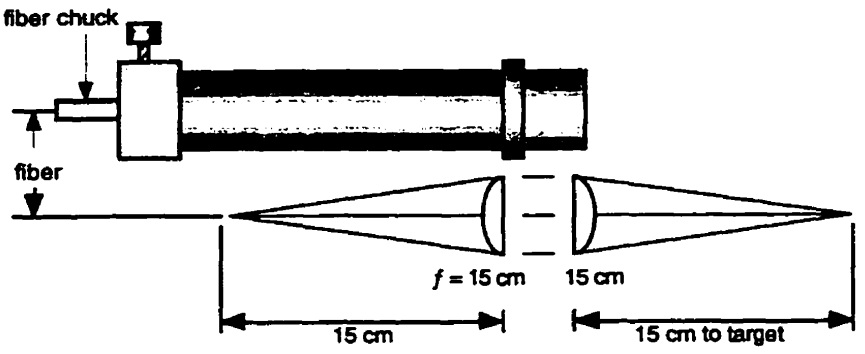

Figure 5-2: Focusing optics for orthogonal TOF-MS.

Beach, FL, USA) connected to a custom preamplifier (provided by the Münster group). The signal from the pyroelectric detector preamplifier is fed into a linear amplifier (1416: Canberra Industries, Meriden, Connecticut, USA) and recorded by the data acquisition system for each laser shot.

Calibration of the pyroelectric detector was done with a commercial energy meter (J3-02: Molectron, USA) placed at a position equivalent to the target relative to the output optics. The absolute fluence measurement remains somewhat uncertain because accuracy of the energy meter is not known, the size of the beam spot was not directly measured (only inferred from the optics) and for the orthogonal TOF, losses resulting from entry into the spectrometer could not be exactly reproduced for the calibration. Therefore, the absolute fluence in the two instrumental geometries, for which different optics were used, should not be directly compared. However, the optics were identical for the pulse-counting and the analog measurements in the axial TOF geometry, so the comparison between these measurements is valid.

The incident laser beam strikes the sample target at an angle θ to the normal, so the spot is slightly elliptical with an increased area $A = \pi r^2 / \cos\theta$, where $r = 100\mu m$ is the fiber radius. In both TOF geometries, the incident angle is about 65° giving an area of about $7.4\times10^{-8} m^2$.

5.2.2 Sample preparation

Sample preparation was similar for all the yield measurements. The pulse-counting experiments require a comparison of ion yields from many different sample spots, so it was essential to obtain uniform sample coverage over a fairly large area. For this reason the fast-drying technique introduced by Vorm *et al* [8] was used. Approximately 40–80µl of analyte solution with concentration ~1 g/l in 0.1% aqueous TFA was mixed with ~1 ml matrix solution with concentration of about 10 g/l in acetone. For the axial TOF experiments, 20µl of this matrix/analyte mixture was deposited on the ~1 cm^2 stainless steel target. About 10 µl of the mixture was deposited on the ~0.5 cm^2 probe tip for measurements in the orthogonal TOF instrument. The acetone evaporates within seconds leaving behind a homogeneous crystallized coating of the matrix/analyte mixture.

5.2.3 Mass Spectrometry

Axial geometry

The linear MALDI/TOF instrument with the usual axial ion-injection geometry is shown in Figure 5-3 (with the data acquisition set up for pulsed-counting detection). The positive ions produced at the target are accelerated by a constant electric field established by the target at 10kV and a grounded 90% transmission grid spaced 10mm apart. A small adjustable aperture, about 53cm in front of the target, controls the number of ions that reach the detector. The aperture consists of a tapered horizontal slit cut into a rotating half-cylinder placed in front of a stationary vertical slit with a width of 5mm. The aperture size can be varied continuously from zero to about 1 cm^2.

The small adjustable aperture is used in the pulse-counting experiment. The purpose of the pulse-counting measurements is to count single ions to improve the sensitivity and linearity of the yield measurements. In the higher fluence range, it is therefore necessary for the pulse-counting measurements to reduce the transmission of the instrument with the adjustable aperture. The aperture size is set, in this case, so that the probability of detecting an ion of a single species is much less than one. For the analog measurements

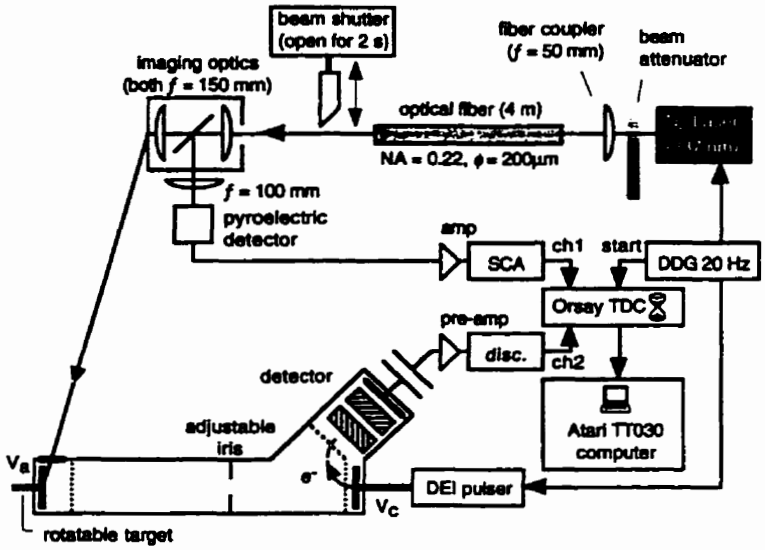

Figure 5-3: Schematic diagram of the axial MALDI/TOF instrument with data acquisition set up for pulse-counting detection.

the aperture is left open.

Each measurement cycle is initiated by a 4-output digital-delay generator (DDG) (9650: EG&G PARC), which triggers the laser and supplies a start signal for the timing measurement. The ions are detected by secondary-electron emission from a conversion plate coated with CsI. The secondary electrons are accelerated between the conversion plate at –600 V and a grounded 95%-transmission grid, and then directed through a circular arc by uniform magnetic field onto microchannel-plate detector which is at 135° relative to the conversion plate. To avoid detector saturation from the abundant low-mass matrix ions, the conversion plate voltage is held at ground for an appropriate time interval (set by the DDG) after each laser shot. Before the molecular ions reach the conversion plate, its voltage is switched to –600 V by a DEI pulser (GRX-1.5K-E: Directed Energy, Inc., Collins, CO, USA). The amplified signals from the microchannel plates are then recorded by the data acquisition system (see below).

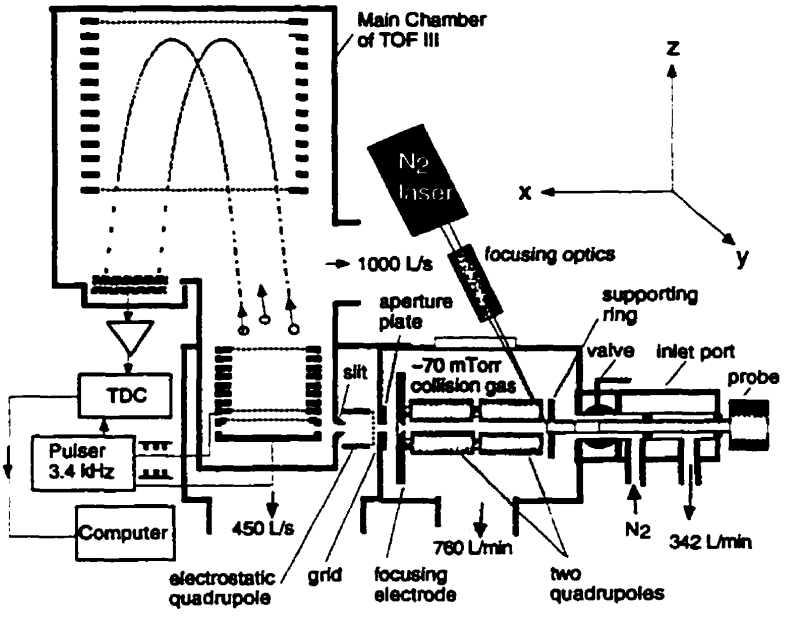

Figure 5-4: Schematic diagram for orthogonal TOF instrument.

Orthogonal geometry

A schematic diagram of the new orthogonal-injection MALDI/TOF instrument is shown in Figure 5-4. In this instrument, the ejected MALDI plume enters an rf-quadrupole ion guide which is filled with nitrogen at a pressure of ~70 mTorr. Collisional cooling in the ion guide produces a beam with a low energy distribution and small cross-section, well-suited for orthogonal injection into a reflecting TOF instrument. Details of this spectrometer and its performance can be found in [7]. For this experiment, the relevant characteristic is that the collisional-cooling spreads the MALDI plume out along the quadrupole axis, which allows many injection pulses to be used for each laser shot. Therefore, pulse-counting detection is not limited to counting at most one ion of a given species per laser shot.

In these experiments, the laser is pulsed at 20 Hz, and ions are injected into the spectrometer at a repetition rate of 3400 Hz. In most cases, even for the highest fluence, on average fewer than one ion of a given species is injected into the spectrometer per injection pulse, so the instrument is well-suited for pulse-counting. Since there are about 170 injection pulses for each laser shot, this arrangement allows pulse-counting to be used

with a 170-fold increase in data-rate over the pulse-counting measurement done in an axial MALDI/TOF instrument. This allows almost the entire fluence range to be examined without artificially reducing the ion transmission, and without ambiguity as to the number of ions striking the detector. Although the ion transmission was not deliberately reduced, it should be mentioned that the overall transmission of the orthogonal injection geometry is small; probably much less than 1%. This low transmission limits the accessible fluence range at the low end.

The ions enter the acceleration column perpendicular to the TOF axis, with about 6eV energy, defined by the potential applied to the aperture plate. They are injected into the TOF spectrometer by pulses applied to the back electrodes of the acceleration column, which then accelerates them to an energy of about 4keV. After acceleration, the ions travel toward an electrostatic ion mirror which reflects them into the microchannel plate detector. At the detector the ions undergo post-acceleration through ~1kV so their total energy when they strike the detector is about 5keV (for the singly-charged ions considered here).

5.2.4 Data Acquisition

Analog measurements

Analog measurements are made only in the axial geometry, and the electronics are shown in Figure 5-5. For these measurements the adjustable aperture is left open ($\sim 1\,cm^2$, and the procedure is similar to the usual analytical application of MALDI; a complete mass spectrum is recorded for each laser shot with a digital oscilloscope (LeCroy 9450AM: LeCroy Corp., NY). The signal from the microchannel-plate detector is fed directly to the input of one channel of the oscilloscope. The amplified signal from the pyroelectric detector is fed into the second channel of the oscilloscope, and the sum of the two transients is transferred to the computer (SuperMac C600 603e/200: Umax) through a GPIB/SCSI interface (IOTech MacSCSI488: IOTech Inc. Cleveland, OH, USA). Thus each transient contains a measure of the laser fluence and the secondary ion yield; the two are well-separated in time so the signals do not interfere.

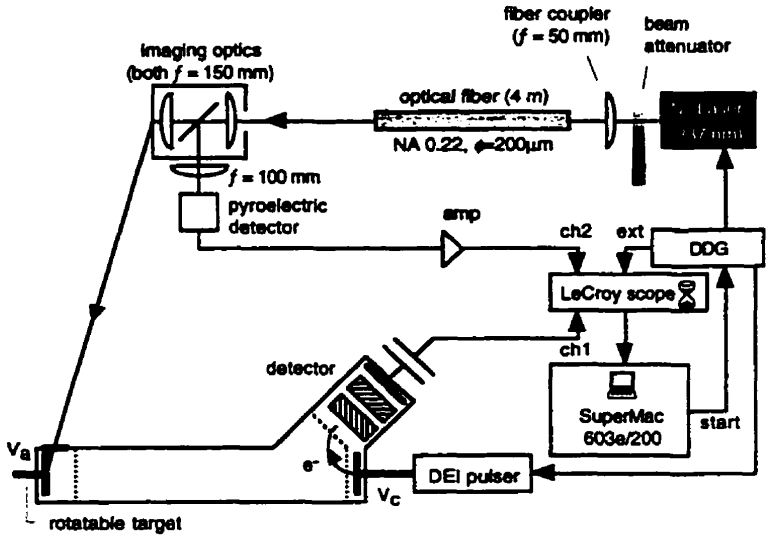

Figure 5-5: Schematic diagram for analog detection set up for the axial MALDI/TOF. Same instrument and optics as the pulse-counting setup shown in.Figure 5-3.

Following the procedure of Dreisewerd *et al* [4], all ion yields were measured from spectra generated from *single* laser shots to ensure precise fluence measurements. To minimize the usual spot-to-spot fluctuations in ion yields, complete yield versus fluence data sets were collected from single spots. There is some depletion of the signal during irradiation, especially after the first few shots. However, by ignoring the first 10 or 20 shots on a spot, and by careful monitoring of the signal at a given fluence, this effect could be made small enough to ignore. Relative yields were obtained from the height of the peak of interest in the digitized transient. Absolute yields are expected to be proportional to these peak-heights, but the proportionality constant, determined by instrument transmission and the detector gain, was not evaluated, so the units are arbitrary.

Pulse-counting measurements

The arrangements for the pulse-counting measurements in the two geometries are shown in Figures 5-3 and 5-4. In both cases, a 255-stop time-to-digital converter (TDC) (CTN-M2: Institut de Physique Nucléaire, Orsay, France) is used instead of a transient recorder

to measure the time between the start signal and the detector pulses, produced, in the ideal case, by individual ions. The repetition rate of the laser is set to its maximum (20Hz) for these measurements. In the axial geometry, the start signal for the TDC is coincident with the laser trigger, and both are supplied by the digital delay generator. In the orthogonal geometry, the start signal corresponds to the injection pulse which is supplied at 3400Hz by the digital delay generator; the laser is triggered internally at 20Hz.

To detect single ions, the microchannel-plate voltage is set so that the signal from individual ions is substantially larger than the noise. The detector signal is amplified with a preamplifier (9301: EG&G ORTEC, Wellesley, MA, USA), and then fed into a constant-fraction discriminator (axial TOF: Philips Scientific 715, Ramsey, NJ, USA; orthogonal TOF: ENERTEC Schlumberger 7174) with the threshold set high enough to eliminate noise (about –59mV). Timing signals from the discriminator are fed into the TDC, connected to a computer which accumulates the time-of-flight histogram. For the axial TOF measurements, an Atari TT030 computer was used with a custom interface, and for the orthogonal TOF measurements, a PowerMac 7300/180 was used connected by a PCI digital I/O card (FPCI-DIO: Fishcamp Engineering, Orcutt, CA, USA).

Yield measurements made using pulse-counting (in both geometries) clearly require accumulation of data from many laser shots. Therefore a protocol was developed to ensure that the laser fluence for a series of laser shots on different target sites was within a selected range. The amplified signal from the pyroelectric detector, which is proportional in amplitude to the laser fluence for each shot, was fed into a single-channel analyser (SCA) (Ortec 455: EG&G ORTEC, Wellesley, MA, USA). The SCA generates an output pulse if the input pulse-amplitude is within a selected range. For these measurements, the SCA was always set to accept laser shots within a 5% fluence window. The output of the SCA is connected to a second channel of the TDC and the data acquisition software is configured to record data from the ion detector only if a pulse from the SCA is detected; that is, only if the corresponding laser shot is within the 5% energy window. Operating at a constant repetition-rate, the laser used for these measurements has approximately 10%

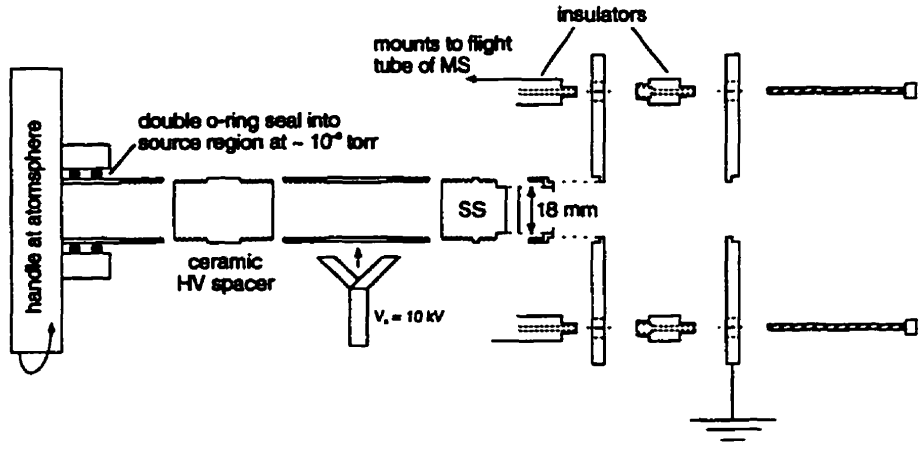

Figure 5-6: Rotatable target used in axial MALDI/TOF instrument.

fluctuations in the energy from shot-to-shot. Thus, the SCA improves the precision in the fluence value for a given yield measurement by a factor of about 2, and perhaps more importantly, ensures that no anomalous laser shots, with significantly higher fluence, contribute to the measured yield.

Each spectrum is the accumulation of data from several different target spots, each spot exposed to the laser for two seconds (~40 laser shots). Since the stability of the laser fluence is better if the laser runs continuously at a constant repetition rate, the two-second exposure was achieved with a custom electronic shutter, consisting of a solenoid switch connected to a standard darkroom timer. To ensure that the laser spot-size remains constant, the optics are left fixed for all measurements, and the target is moved to expose different sample sites. Thus the identical laser focus is used for all the target sites. For both the axial and orthogonal geometries, a rotatable sample probe is used. Figure 5-6 shows the details of the probe used in the axial TOF instrument; in this case the target has to be isolated to 10 kV. In the axial TOF instrument, at most about 50 spots were used per energy window, corresponding to about 2000 laser shots, and to one full rotation of the target. In the orthogonal TOF instrument, the probe was smaller, and at most about 30 spots were used. Fewer target spots were needed for higher fluence since the count rate is higher. After one full rotation of the target, a fresh target-sample was prepared. The spot-to-spot

fluctuations mentioned above tend to average out in this case where data from many spots, and many laser shots, are accumulated. The relative yields are determined by integrating the peak of interest and dividing by the number of laser shots, and are therefore reported as counts per laser shot.

5.3 Results and Interpretation

5.3.1 Measurements in the axial TOF geometry

The measured relative yields for insulin with the matrices αCHCA and sinapinic acid, and for LHRH with the matrix αCHCA, obtained with the axial MALDI/TOF instrument are shown in Figure 5-7. Pulse-counting data are shown for two different aperture sizes to probe different fluence ranges. The data sets are fit to a simple power-law, $Y = kF^m$, where Y is the yield, F is the fluence, and k and m are fit parameters. The open data points at higher fluence, which deviate from the power-law dependence, are excluded from the fit. The slope m for each curve is indicated in the figure.

Interpretation of the analog measurements

The vertical scale for the analog measurements (shown on the right axis) represents the molecular ion peak heights determined from the recorded transient. For a detector with a linear response to the incident ions, these peak heights are proportional to the number of ions produced in "successful" laser shots; that is, shots which produced a transient with a visually identifiable molecular ion peak. The saturation of the curves at high fluence may result from detector saturation, or from saturation of the MALDI process.The slopes of the power-law fits range between about 7 and 10; the observed slopes in (b) and (c) are somewhat higher than in previous measurements [4], possibly because of non-linearity in the detector. We found that the measured slope depends to some extent on the detector gain, indicating a non-linear response. However, this should not significantly affect the evaluation of the observed threshold for analog detection, which was the main purpose of making analog measurements in the same spectrometer.

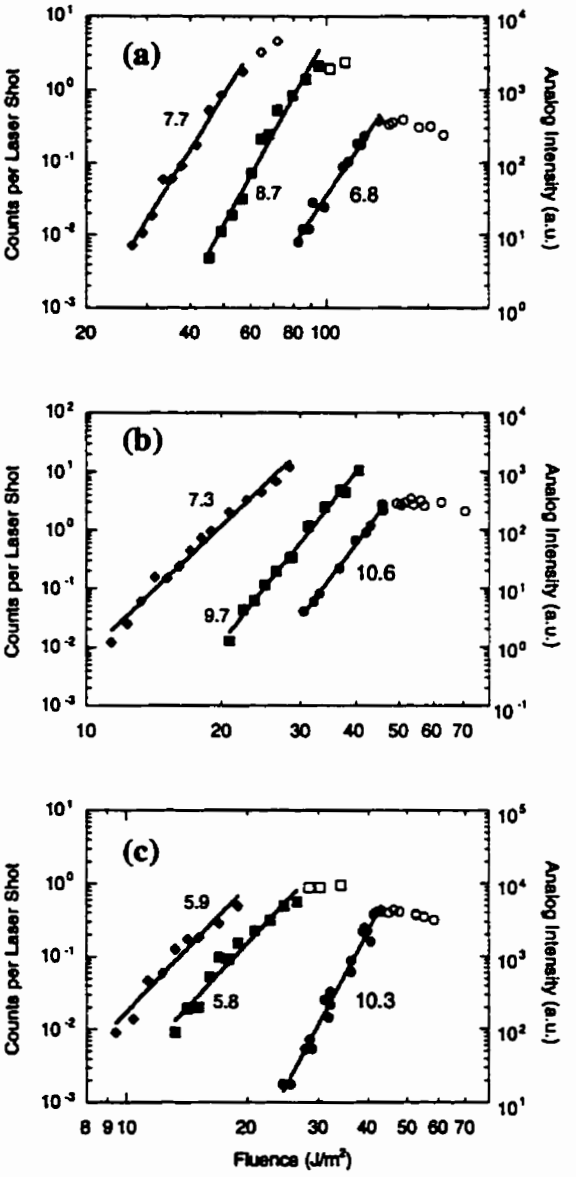

Figure 5-7: Dependence of ion yield versus fluence using conventional MALDI/TOF with (a) insulin and sinapinic acid (b) insulin and αCHCA (c) LHRH and αCHCA. (●) analog measurements; (■) TDC, wide iris; (◆) TDC, small iris. Hollow data points indicate saturation and numbers are the slopes.

Interpretation of the pulse-counting measurements

The vertical scale for the pulse-counting experiment (shown on the left axis) represents the number of pulses counted in the time-window corresponding to the molecular ion, divided by the number of laser shots. Thus the data represent the probability that a molecular ion will be detected for a given laser shot. More than one detected pulse per shot is possible at the higher fluence because the peak width is considerably broader than the dead-time of the counting system; however, saturation of the counting system is evident in this range.

The interpretation of the pulse-counting data from the axial TOF measurements depends to some extent on the fluence and the size of the aperture used. In contrast to the analog measurements, which consider only those laser shots that produce an observable ion signal, the pulse-counting measurements take account of all the laser shots. Individual laser shots may or may not produce a desorption event, but when they do, a large number of molecular ions are ejected; using typical sample preparation methods, $>\sim 1000$ molecular ions are produced [3]. The measured detection probability is therefore determined by the probability of producing a successful desorption event, and the number of ions produced (which determines the probability that at least one ion passes through the aperture and is detected).

These two effects dominate separately for the two aperture settings used to collect the data of Figure 5-7. If each laser pulse produces a desorption event, and if on average fewer than one ion passes through the aperture per laser shot, then the measured probability for detecting an ion is simply proportional to the number of ions desorbed. This is approximately the case for the measurements with the small aperture at higher laser fluence. These results can then be compared directly, apart from a normalization constant, (and to the extent the detector has a linear response in the analog measurements) with the results obtained using analog detection. In two cases (a and b) the slopes are similar.

For low fluence, where the probability for producing a desorption event is substantially less than unity, and for an open aperture ($\sim 1 cm^2$), the interpretation is different. In this case, successful events will be detected with high probability, and the number of ions

per pulse cannot be extracted. The measurements therefore represent the probability of the *production* of a successful desorption event.

The measured slopes for the pulse-counting measurements range between about 6 and 9, somewhat higher than reported by Ens *et al* [3], but consistent with those reported by Dreisewerd *et al* [4]. Interestingly, the slopes measured with the two aperture sizes, representing in one case the average number of ions per desorption event, and in the other the probability for producing a desorption event are rather similar.

The results in the axial geometry show clearly that the pulse-counting experiment examines a fluence range substantially lower than that accessible with analog measurements. However, there is no evidence in any of the curves for a fluence threshold.

5.3.2 Measurements in the orthogonal TOF geometry

The measured relative yields for LHRH with four different matrices, for γ-endorphin with the matrix α-CHCA, and for insulin with sinapinic acid, obtained with the orthogonal-injection MALDI/TOF instrument are shown in Figure 5-8. As above, the data sets are fit to a simple power-law, and the slopes are indicated in the figure. The open data points at higher fluence in A and E, which deviate from the power-law dependence, are excluded from the fit. The measured slopes are between 7 and 9. Only the slopes can be compared directly with the measurements in the axial TOF instrument. The transmission is unknown in both cases so the yields are only relative; the absolute fluence is estimated in both cases, but the uncertainty is rather high.

As described above, the spectra are accumulated with pulse-counting methods in this instrument, but the results are much simpler to interpret than the pulse-counting measurements in the axial TOF instrument, and a wider fluence range can be accessed than in the analog measurements without changing instrumental conditions. Because each MALDI plume is spread out along the quadrupole axis, only a few ions are injected into the TOF instrument in a given measurement cycle, and the probability that more than one ion of a given species are detected is negligible, except at the highest fluence in some

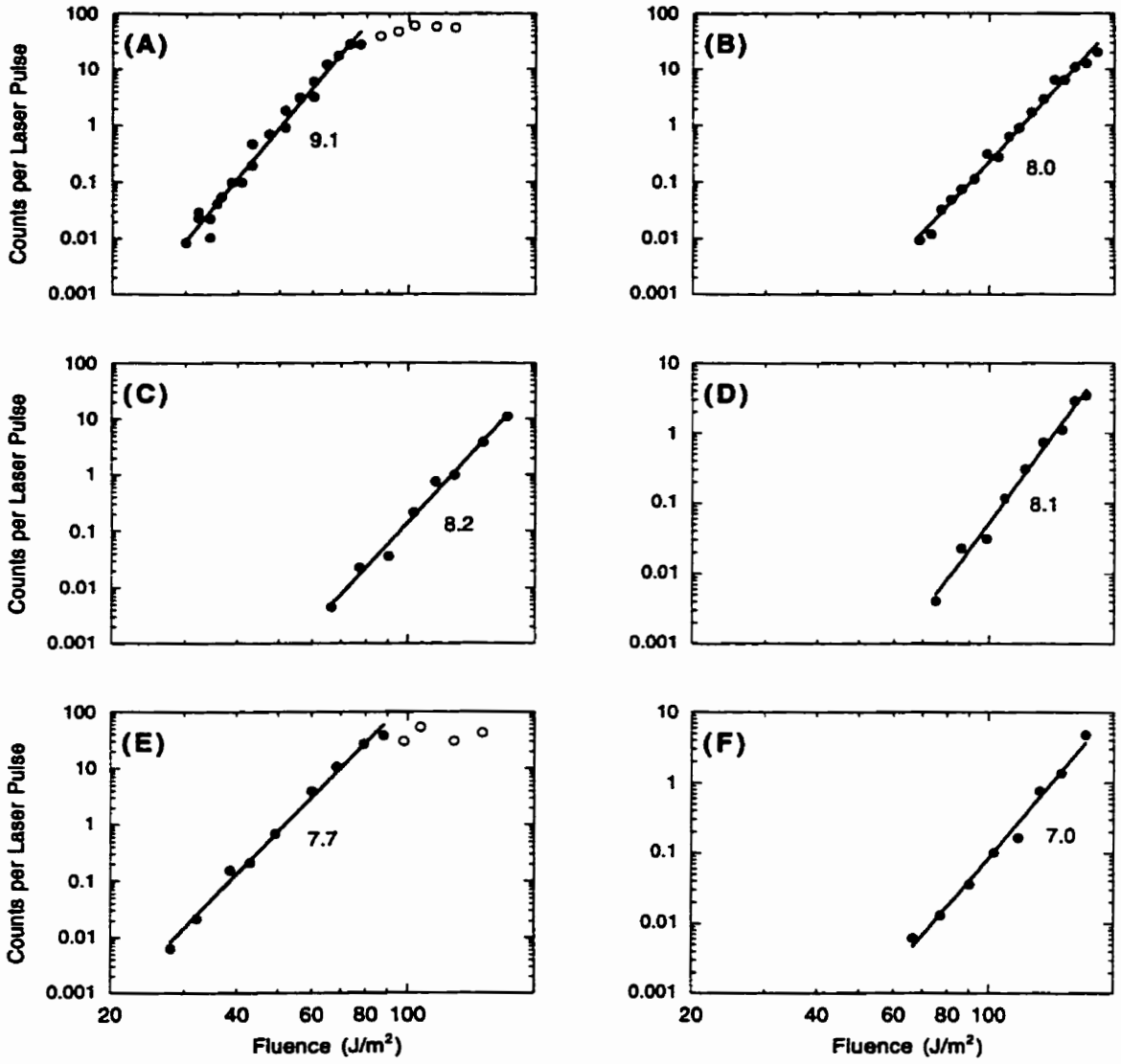

Figure 5-8: Ion yield as a function of laser fluence using an orthogonal-injected MALDI/TOF with collisional cooling. (A) LHRH in αCHCA, (B) LHRH in sinapinic acid, (C) LHRH in 2',6'-dihydroxyacetophenone, (D) LHRH in DHB, (E) γ-endorphin in αCHCA, (E) insulin in sinapinic acid. Hollow data points indicate saturation and numbers are the slopes.

cases. When the count rate for a given species approaches the repetition rate of the injection pulser, then saturation does occur, as in Figure 5-8 A and E. Such saturation of the counting system is readily observed in this instrument because of its high mass resolution. The dead-time of the TDC is sufficient to spoil the isotopic pattern for a given species if multiple ions of that species are detected. In the other cases, where the yield was lower, the full fluence range could be used with a reliably linear detector response. The fluence for these measurements was varied by close to an order of magnitude, corresponding to a range of yields more than 4 orders of magnitude, exceeding all previous measurements.

The measured yields are simply proportional to the average number of intact molecular ions produced per laser pulse. However, as described above, there are two contributions to this average: the probability that a laser shot produces a desorption event, and the number of ions desorbed in a successful event. At low fluence where the probability of desorption is significantly less than one, these contributions cannot be separated using the present data.

5.4 Discussion

The results are consistent with the earlier experiments [3,4] which show a steep power-law dependence of the molecular ion yield on laser fluence. The most reliable measurements indicate a slope on a log-log plot of about 8 depending on the particular analyte-matrix combination. The slope also depends on other details of the measurement. Dreisewerd *et al* showed that the slope decreases for smaller spot sizes [4]. We have found that if the laser is simply focused directly onto the target with a single lens, giving a gaussian distribution, the slope is somewhat lower, consistent with measurements of Ens *et al* [3]. Moreover, the slope was found to depend slightly on the number of shots per spot in the pulse-counting measurements, as shown in Figure 5-9. By changing the shutter time by a factor of 10, there is a ~15% increase in the slope. This reflects the fact that the ion yield from a single spot persists longer for higher fluence, so the higher fluence data points benefit more from the longer exposure.

As expected, pulse-counting measurements can give yields for considerably lower fluence values than are accessible with analog measurements, at least if only single shots are analysed. However, contrary to the previous observations made with pulse-counting [3], these measurements indicate no evidence for a true fluence threshold in the yield. It is of course possible that a threshold exists at lower fluence, but it is clear that the practical threshold normally associated with analog measurements in MALDI is not a physical threshold. It is not surprising that an apparent threshold is associated with MALDI in view of the steep fluence dependence. If at some fluence value, the probability of observing a peak with analog measurements is proportional to the average number of ions per laser shot, then a 30% increase in fluence increases the probability of observation from 10% (near zero) to about 90% (near unity). In practice, such an increase looks like a threshold.

A change in the dependence of the yield on fluence might be expected as the probability for desorption decreases significantly below unity, but such a change is not observed. Surprisingly the dependence on fluence of the probability-of-desorption seems to be the same as the dependence of number of ions desorbed per desorption event. It is possible with the new orthogonal TOF instrument to measure these two effects separately and to sort out the statistics of MALDI desorption; such measurements are planned.

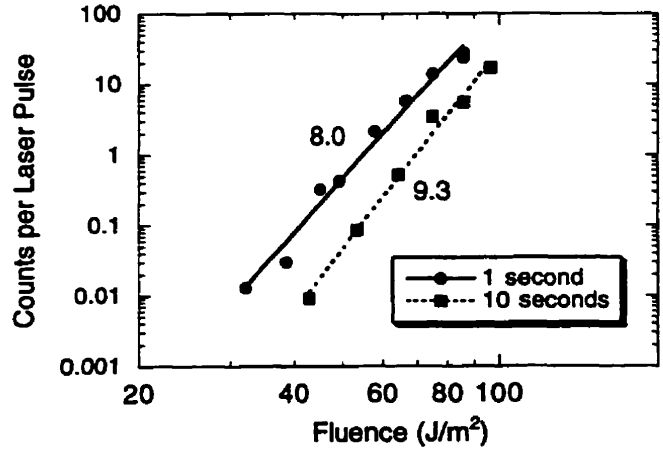

Figure 5-9: The effect of varying the time (number of laser shots at 20Hz) per spot on the target. Target: insulin with αCHCA.

5.5 Conclusions

The average number of molecular ions of peptides desorbed per laser pulse in MALDI has a steep power-law dependence on fluence with a power of between 7 and 9. No evidence was observed for a fluence threshold in the desorption.

CHAPTER 6

CONCLUSION

Some Final Remarks

The general goals of this work have been to develop improved methods of mass spectrometry for applications in the biological sciences. Progress in this field is generally made by empirical experimentation, which is to some extent trial-and-error, but is guided by observed trends and some understanding of the physical processes involved. The work on PSD MALDI in chapter 4 is an example of practical experimentation with the direct goal of developing improved instrumentation.With the exception of this chapter, the objectives of the experiments described in this thesis have been to identify more fundamental trends in the physical processes. Such measurements can give direct indications for improved instrumentation as in the case of the experiments on detection in chapter 3, or they can contribute more indirectly by illuminating the underlying physical processes. Many of the advances in biological mass spectrometry have been in the area of ionization methods, and the experiments on stopping power in chapter 2 and on laser fluence in chapter 5 examine some fundamental aspects of two recently introduced ionization methods.

The experiment described in chapter 2 correlates the desorption of molecular ion yields with the mechanism of energy loss—nuclear or electronic stopping—experienced by keV-energy atomic ions impinging on an organic solid substrate. The conditions are similar to those typical in secondary ion mass spectrometry. The results add to a large body of experimental data for atomic collisions with solid surfaces. Electrospray ionization and MALDI have largely replaced particle-induced desorption as ion sources mass

spectrometry of large molecules. However, there is considerable evidence that an increase in the number of atoms in the projectile can give significant improvement. For example, Mahoney and colleagues at Phrasor Scientific have developed an electrosprayed source of glycerol clusters that yield secondary ion charge distributions lying between those produced in MALDI and in electrospray.

Detection of large molecular ions is a central problem in mass spectrometry and is addressed by the experiment described in chapter 3. As the mass of desorbed molecular ions increases with improved ionization techniques, detection using secondary electron emission, the most common method of detection, becomes less efficient, at least with practical accelerating voltages (~30 to 40 keV). The results from chapter 3, quantifies the electron emission efficiency as well as the secondary ion emission efficiency for large, slow moving molecular ions near the typical detection limits in organic mass spectrometry. This is important information in characterizing the preformance of secondary emission detectors, and thus, offers some insight on how to design new detector geometries. For example, the most efficient method for detecting large molecular ions is the use of secondary ion emission because ions have a higher emmision efficiency than secondary electrons. On the other hand, the experiments indicate what loss in sensitivity can be expected if electron emission is used because of its superior timing characteristics. In addition to any practical information regarding detector characterization or design, this experiment, adds to a rather large body of experimental data on ion-surface collisions, and in particular, on electron emission from bombardment with clusters in the velocity regime near the threshold for kinetic emission.

Chapter 4 introduces an instrumental development in the post-source decay technique, which takes advantage of metastable decay of molecular ions for structural analysis. The proposed alternative method for post-source decay analysis given in this chapter can easily be applied to existing reflecting time-of-flight instruments which are common in chemical/biochemical labs. No hardware modification is need for the proposed method and thus the benefits or practical advantages of the method are easily attainable. The

method, in principle, offers improved mass accuracy and simplified analysis. In the long term, however, both the usual and proposed methods of PSD analysis may be replaced by improved methods of tandem mass spectrometry. For example the quadrupole-TOF geometry which uses orthogonal injection as shown in Figure 5-4, but adds a quadrupole mass filter for parent-ion selection, shows great promise for this type of measurement, both with ESI and MALDI sources.

One of the most common and successful methods for desorbing large, intact molecular ions is matrix-assisted laser desorption/ionization (MALDI). A better understanding of the desorption/ionization mechanism may lead to improved desorption techniques involving different laser wavelengths or different matrices. The results described in chapter 5 show a steep dependence of the ion yield on the laser fluence but show no evidence for a fluence threshold. Thus the possibility to use a very high repetition rate laser (say 100 kHz) with low laser fluence (per shot) is not excluded. The results are consistent with a quasi-thermal description of the desorption processes as discussed by Dreisewed *et al.* [4].

APPENDIX

The total stopping power for amino acid valine was calculated by adding the contributions from each of the atomic constituents of the target. See section 2.3 Stopping Power Calculation on page 24 for more details about the calculations. For valine ($C_5H_{11}NO_2$), the program input data used to calculate $(dE/dx)_n$ and $(dE/dx)_e$ is as follows:

target density (g/cm^3):	1.0	
Z_i	n_i:	
	6	5
	1	11
	7	1
	8	2

The program also reads in (from another text file) an array of atomic weights from $Z = 1$ to 57. The output data of the progam is two text files, one for $(dE/dx)_n$ and another for $(dE/dx)_e$, each containing dE/dx (in eV/Å) versus the atomic weight of the projectile (in u).

C Program Calculating Stopping Power

```
#include<math.h>
#include<stdlib.h>
#include<stdio.h>
#include<string.h>

#define N_PI        57      /* max. no. projectiles (Z = 1 to 57) */
#define N_TARGET    10      /* max. no. of target atomic constituents */

void GetTarget(char *, double *, int *, double *);

main(int argv, char **argc)
{
    FILE *fp, *fp_e, *fp_n;
    char file_n[30];    /* file name for output data: A vs dedx_n */
    char file_e[30];    /* file name for output data: A vs dedx_e */
    char file[30];      /* file name with no "_n" or "_e" extension */
```

```
int i;              /* counter */

double A1[N_PI];    /* atomic masses Z1 = 1 to 57 */
int Z1;             /* atomic number of projectile */

double A2;          /* molecular weight of molecule, e.g. valine */
double n[N_TARGET]; /* no. of each atomic constituent in molecule */
double density;     /* mass density of taget molecule */
int Z2[N_TARGET];   /* atomic numbers for target */
double N[N_TARGET]; /* atomic density of each target atom */

double e;           /* electron charge */
double Na;          /* Avogadro number */
double k;           /* units converstion factor = 9e9 */
double a;           /* screened scattering length */
double ZZ;          /* variable that depends on Z1 and Z2 for dedx_e */
double Ereduced;    /* reduced energy */
double gamma;       /* CM transfromation unit */
double Eincident;   /* incident energy of projectile */
double A, B, C;     /* constants used in reduced nuc stopping power */
double Sn;          /* reduced nuclear stopping power */
double Se;          /* electronic stopping cross section */
double ao, vo;      /* Bohr radius and velocity */
double u;           /* atomic mass unit */

double dedx_n[N_TARGET];    /* atomic nuclear stopping power */
double dedx_total_n;        /* total nuclear stopping power */
double dedx_e[N_TARGET];    /* atomic electronic stopping power */
double dedx_total_e;        /* total electronic stopping power */

printf("\n Stopping Power VS Mass...\n\n");

if(argv!=2)
{
    printf("\n I need a data file for the target molecular ion:");
    printf("\n target density [g/cm^3]");
    printf("\n Z1  n1");
    printf("\n Z2  n2");
    printf("\n etc.\n");
    exit(1);
}
else GetTarget(argc[1], &density, Z2, n);

/* define A1[i] array */
if((fp=fopen("A.dat", "rt"))==NULL)
{
    printf("\nCannot open file A.dat
          (column of atomic wieghts from Z = 1 to 57)\n");
    exit(1);
}
else
{
    for(i=0;i<N_PI;i++) fscanf(fp," %lf", &A1[i]);
```

```
    fclose(fp);
}

/* inialize constants */
k  = 8.988e9;
Na = 6.022e23;
e  = 1.6e-19;
u  = 1.66e-27;
A  = 0.56258;  /* average value from Wilson 1977 */
B  = 1.17760;  /* average value from Wilson 1977 */
C  = 0.62680;  /* average value from Wilson 1977 */
ao = 5.29e-11; /* m */
vo = 2.18e6;   /* m/s */

printf("density (g/cm^3): %.2f\n", density);
printf("incident energy (keV): ");
scanf("%s", file);
Eincident = atof(file);
Eincident *= 1000.0 * e; /* Joules */
strcat(file,"keV");
strcpy(file_n, file);
strcat(file_n,"_n.dat");
strcpy(file_e, file);
strcat(file_e,"_e.dat");
printf("data files: %s and %s\n", file_n, file_e);


A2=0.0;
for(i=0;i<N_TARGET && Z2[i]!=0;i++) A2 += n[i]*A1[(Z2[i] - 1)];
printf("molecular atomic wieght of target: %.2f\n", A2);

/* density (atoms per m^3) for each atomic constituent */
for(i=0;i<N_TARGET && Z2[i]!=0;i++)
    N[i] = density*n[i]*A1[(Z2[i]-1)]*1000000.0*Na/pow(A2,2.0);


/* open output data files */
if((fp_n=fopen(file_n, "wt"))==NULL)
{
    printf("\nCannot open file %s\n", file_n);
    exit(1);
}
if((fp_e=fopen(file_e, "wt"))==NULL)
{
    printf("\nCannot open file %s\n", file_e);
    exit(1);
}

/* calculate dedx for each atomic target */
for(Z1=1; Z1<=N_PI; Z1++)
{
    dedx_total_n = 0.0;
    dedx_total_e = 0.0;
    for(i=0;i<=N_TARGET && Z2[i]!=0.0; i++)
```

```
        {

            /* nuclear stopping */
            a = ao*0.8853/pow((pow((double)Z1,0.5)+
                pow((double)Z2[i],0.5)),0.667);
            gamma = 4.0*A1[(Z1-1)]*A1[(Z2[i]-1)]/
                    pow((A1[(Z1-1)]+A1[(Z2[i]-1)]),2.0);
            Ereduced = a*A1[(Z2[i]-1)]*Eincident/((double)(Z1*Z2[i])*
                       pow(e,2.0)*(A1[(Z1-1)]+A1[(Z2[i]-1)])*k);
            Sn = A*log(B*Ereduced)/(B*Ereduced - 1.0/pow(B*Ereduced,C));
            dedx_n[i] = M_PI*pow(a,2.0)*gamma*N[i]*Eincident/Ereduced * Sn;
            dedx_n[i] *= 1.0e-10/e;  /* eV / Angstroms */
            dedx_total_n += dedx_n[i];

            /* electronic stopping */
            ZZ = pow(pow((double)Z1,0.667)+pow((double)Z2[i],0.667),1.5);
            Se = pow((double)Z1,0.1667)*8.0*M_PI*pow(e,2.0)*k*ao*
                 (double)(Z1*Z2[i])/ZZ * sqrt(2.0*Eincident/(A1[(Z1-1)]*u))/vo;
            dedx_e[i] = N[i]*Se;
            dedx_e[i] *= 1.0e-10/e;  /* eV / Angstroms */
            dedx_total_e += dedx_e[i];
        }
        fprintf(fp_n, "%.5e     %.5e\n", A1[(Z1-1)], dedx_total_n);
        fprintf(fp_e, "%.5e     %.5e\n", A1[(Z1-1)], dedx_total_e);
    }
    fclose(fp);
}


void GetTarget(char *file, double *density, int *Z2, double *n)
{
    int i;
    FILE *fp;

    /* initialize arrays */
    for(i=0;i<N_TARGET;i++)
    {
        Z2[i]=0;
        n[i]=0;
    }
    if((fp=fopen(file, "rt"))==NULL)
    {
        printf("\nCannot open file %s\n", file);
        exit(1);
    }
    fscanf(fp," %lf", density);
    for(i=0;i<N_TARGET;i++)
    {
        if(fscanf(fp," %i %lf", &Z2[i], &n[i])==EOF) break;
    }
    fclose(fp);
}
```

REFERENCES

IN THE BEGINNING

[1] J.J. Thomson, *Philos. Mag. VI,* **24** (1912) 668

[2] F.A. White and G.M Wood, Mass Spectrometry, *Applications in Science and Engineering,* John Wiley & Sons (Chichester, England 1986)

[3] A. Frigerio, *Essential Aspects of Mass Spectrometry,* Spectrum Publications Inc. (Flushing, New York 1974)

[4] D.F. Torgerson, R.P. Skowronski and R.D. Macfarlane, *Biochem. Biophys. Res. Commun.* **60** (1974) 616.

[5] R.D. Macfarlane and D.F. Torgerson, *Science* **191** (1976) 920

[6] R.D. Macfarlane and D.F. Torgerson, *Int. J. Mass Spectrom. Ion Processes* **21** (1976) 81

[7] B.U.R. Sundqvist, P. Roepstorff, J. Fohlman, A. Hedin, P. Håkansson, I. Kamensky, M. Lindberg, M. Salephour and G. Säve, *Science* **226** (1984) 696

[8] G. Jonsson, A. Hedin, P. Hakansson and B.U.R. Sundqvist, *Rapid Commun. Mass Spectrom.* **3** (1989) 190

[9] W.E. Stephens, *Phys. Rev.* **69** (1946) 691

[10] A. Benninghoven, D. Jaspers and W. Sichtermann, *Appl. Phys.* **11** (1976) 35

[11] B.T. Chait and K.G. Standing, *Int. J. Mass Spectrom. Ion Phys.* **40** (1981) 185

[12] W. Ens, K.G. Standing, B.T. Chait, and F.H. Field, *Anal. Chem.* **53** (1981) 1241

[13] W. Ens, P. Hakansson, B.U.R. Sundqvist, *Secondary Ion Mass Spectrometry SIMS VI,* Ed. A.M. Buber, A Benninghoven, H.W. Werner and G. Soldzian (Wiley, Chichester 1988) 623; and unpublished data from the same experiment

[14] M. Barber, R.S. Bordoli, G.J. Elliot, R.D. Sedgwick and A.N. Tyler, *Anal. Chem.* **54** (1982) 645A

[15] D.J. Surman and J.C. Vickerman, *J. Chem. Soc. Chem. Commun.* 1981 (1981) 342

[16] M. Barber, R.S. Bordoli, R.D. Sedgwick and A.N. Tyler, *J. Chem. Soc. Chem. Commun.* 1981 (1981) 325

[17] M. Barber, R.S. Bordoli, G.J. Elliot, R.D. Sedgwick, A.N. Tyler and B.N. Green *J. Chem. Soc. Chem. Commun.* 1982 (1982) 936

[18] A. Dell and H.R. Morris, *Biochem. Biophys. Res Commun.* **106** (1982) 1456

[19] E. Unsold, F. Hillenkamp and R. Nitsche, *Analusis* **4** (1976) 115

[20] R.J. Conzemius and J.M. Capellen, *Int. J. Mass Spectrom. Ion Phys.* **34** (1980) 197

[21] F. Hillenkamp, in *Ion Formation from Organic Solids*, IFOS, Ed. by A. Benighoven, Springer Series in Chem. Phys., **25** (1983) 190–205

[22] F. Hillenkamp, in *Secondary Ion Mass Spectrometry, SIMS V*, Ed. by A. Benighoven, R.J. Colton, D.S. Simmons and H.W. Werner, Springer Series in Chem. Phys. **44** (1986) 471

[23] F. Hillenkamp, M. Karas, R.C. Beavis and B.T. Chait, *Anal. Chem.* **63** (1991) 1193A

[24] M. Karas, B. Bachmann, U. Bahr and F. Hillenkamp, Int. J. Mass Spectrom. Ion Processes 78 (1987) 53

[25] M. Karas and F. Hillenkamp, *Anal. Chem.* **60** (1988) 2299

[26] R.C. Beavis and B.T. Chait, *Rapid Commun. Mass Spectrom.* **3** (1989) 233

[27] R.C. Beavis and B.T. Chait, *Rapid Commun. Mass Spectrom.* **3** (1989) 432

[28] A. Overberg, M. Karas and F. Hillenkamp, *Rapid Commun. Mass Spectrom.* **5** (1991) 128

STOPPING POWER

[1] W. Ens in *Fundamental Processes in Sputtering of Atoms and Molecules* (SPUT92), Ed. P. Sigmund, vol. **43** (Munksgaard, Copenhagen 1993) 155; and references therein

[2] B.U.R. Sundqvist in *Sputtering by Particle Bombardment III*, Ed. R. Behrisch and K. Wittmaack, Topics in Applied Physics, vol. **64** (Springer-Verlag, New York 1991) 257

[3] W. Ens, P. Håkansson, B.U.R. Sundqvist in *Secondary Ion Mass Spectrometery SIMS VI*, Ed. A.M. Huber, A. Benninghoven, H.W. Werner and G. Slodzian (Wiley, Chichester 1988) p. 623; and unpublished data from the same experiment

[4] O. Becker, S. Della-Negra, Y. LeBeyec, and K. Wien, *Nucl. Instrum. Meth.* **B16** (1986) 321

[5] J.E. Hunt, M. Salehpour, D.L. Fishel, and J.C. Tou, *Journal de Physique* **50** (1989) C2-27

[6] K.G. Standing, B.T. Chait, W. Ens, G. McIntosh and R. Beavis, *Nuc. Instrum. Meth.* **198** (1982) 33

[7] A. Albers, K. Wien, P. Dück, W. Treu and H. Voit, *Nucl Instrum. Methods* **198** (1982) 69

[8] E.V. Alonso, R.A. Baragoila, J. Ferron, M.M. Jakas and A. Oliva-Florio, *Phys. Rev.* **B 22** (1980) 80

[9] J. Lindhard, M. Scharff and H.E. Schi{\o}tt, Mat. Fys. Medd., *Dan Vid. Selsk* **33** (1963) no. 14

[10] W.D. Wilson, L.G. Haggmark and J.P. Biersack, *Phys. Rev.* **B 15** (1977) 2458

[11] J. Lindhard and M. Scharff, *Phys. Rev.* **124** (1961) 128

[12] O. Becker, S. Della-Negra, Y. LeBeyec and K. Wien, *Nucl. Instrum. Methods*, **B 16** (1986) 321

[13] B.U.R. Sundqvist, in *Behrisch and Wittmaack* (1991) 257

[14] S. Della-Negra, J. Depauw, H. Joret, Y. LeBeyec and E.A. Schweikert, *Phys. Rev. Lett.* **60** (1988) 948

[15] T.Y. Yen, E. Barofsky and D.F Barofsky, presented at SPUT92 (1992) Copenhagen; T.Y. Yen, Ph.D. Thesis (1992), Oregon State University, Corvalis Oregon

[16] D. Barofsky and Bitensky, *Phys. Rev.* **B56** (1997) 13815

[17] C.T. Reimann, *Mat. Fys. Dan. Vid. Selsk.* **43** (1993) 531

SECONDARY EMISSION

[1] R. J. Beuhler and L. Friedman, *Int. J. Mass Spectrom. Ion Processes* **170** (1980) 309

[2] A. Hedin, P. Håkansson, and B.U.R. Sundqvist, *Int. J. Mass Spectrom. Ion Processes* **75** (1987) 275

[3] R. J. Beuhler, *J. Appl. Phys.* **54** (1983) 4118

[4] B. Spengler, D. Kirsch, R. Kaufmann, M. Karas, F. Hillenkamp, and U. Giessmann, *Rapid Commun. Mass Spectrom.* **4** (1990) 301

[5] J. Martens, W. Ens, K. G. Standing and A. Verentchikov, *Rapid Commun. Mass Spectrom.* **6** (1993) 75

[6] A. Brunelle, P. Chaurand, S. Della-Negra, Y. LeBeyec, and G. B. Baptista. *Int. J. Mass Spectrom. Ion Processes* **126** (1993) 65

[7] H. Haberland and M. Winter, *Rev. Sci. Instrum.* **54** (1983) 764

[8] A Verentchikov, W. Ens, J. Martens, and K. G. Standing, *Int. J. Mass Spectrom. and Ion Processes* **126** (1993) 65

[9] D. Hasselkamp, H. Rothard, K. -O. Groeneveld, J. Kemmler, P. Varga, and H. Winter, *Particle Induced Electron Emission II*, (Springer-Verlag, Heidelberg, 1992) and references therein

[10] R. A. Baragiola, in *Low Energy Ion-Surface Interactions*, Ed. J.W. Rabalais, (Wiley, Chichester, 1994), p. 187, and references therein

[11] G. Lakits and H. Winter, *Nucl. Instrum. and Methods* **B48** (1990) 597

[12] R. A. Baragiola, *Nucl. Instrum. Methods* **B88** (1994) 35, and references therein

[13] A. Baragiola, E. Alonso, J. Ferron and A. Oliva-Florio, *Surface Sci.* **90** (1979) 240

[14] H. Hagstrum, *Phys. Rev.* **96** (1954) 336

[15] U.Arifov, L. Kishinevshii, E. Mukhamadiev and E. Parilis, *Sov. Phys. Tech. Phys.* **18** (1973) 118

[16] H. Hagstrum and G. Becker, *Phys. Rev.* **B8** (1973) 107

[17] R. A. Baragiola, E.V. Alonso, and A. Oliva, *Phys. Rev.* **B19** (1979) 121

[18] L.A. Dietz and J.C. Sheffield, *J. Appl. Phys.* **46** (1975) 4361

[19] P. M. Waters, *Phys. Rev.* **111** (1958)1053

[20] E.V. Alonso, M. Alurralde, and R.A. Baragiola, *Surf. Sci.* **166** (1986) L155

[21] K. Töglhofer, F. Aumayr, H. Kurz, H. Winter, P. Scheier, and T. D. Märk, *Nucl. Instrum. Methods* **B88** (1994) 44

[22] P. W. Geno and R. D. Macfarlane, *Int. J. Mass Spectrom. Ion Processes* **92** (1989) 195

[23] R. Mosshammer and R. Matthäus, *J. Phys.* (Paris) **C2** (1989) 111

[24] J. Axelsson, C.T. Reimann, and B.U.R. Sundqvist, *Nucl. Instrum. Methods* **B88** (1994) 131

[25] S. Della-Negra, M. Dumail and Y. LeBeyec, *Rapid Commun. Mass Spectrom.* **1** (1987) 10

[26] A. Brunelle, P. Chaurand, S. Della-Negra, Y. Le Beyce and E. Parilis, *Rapid Commun. Mass Spectrom.* **11** (1997) 353

POST-SOURCE DECAY

[1] R. Kaufman, D. Kirsch and B. Spengler, *Int. J. Mass Spectrom. Ion Processes* **131** (1994) 355

[2] X. Della-Negra and Y. LeBeyec, *Anal. Chem.* **57** (1985) 2035

[3] X. Tang, W. Ens, F. Mayer and K.G. Standing, *Rapid Comun. Mass Spectrum.* **3** (1989) 443

[4] B. Spengler, D. Kirsch and R. Kaufmann, *J. Phys. Chem.* **96** (1992) 9678

[5] B. Spengler, D. Kirsch, R. Kaufmann and E. Jaeger, *Rapid Commun. Mass Spectrum.* **6** (1992) 105

[6] X. Tang, R. Beavis, W. Ens, F. Lafortune, B. Schueler and K.G. Standing, *Int. J. of Mass Spectrom. Ion Process.* **85** (1988) 43

[7] R. Kaufmann, D. Kirsch and B. Spengler, *Int. J. Mass Spectrom. Ion Process.* **131** (1994) 355

[8] A.M. Cravath, *Phys. Rev.* **33** (1929) 605

[9] N.E. Bradbury and R.A. Nielsen, *Phys. Rev.* **49** (1936) 388

[10] J. Martens, W. Ens, K.G. Standing and A. Verentchikov, *Rapid Commun. Mass Spectrum.* **6** (1992) 147

[11] P.R. Vlasak, D.J. Beussman, M.R. Davenport and C.G. Enke, *Rev. Sci. Instrum.* **61** (1996) 68

[12] C. Hauer, K. Roth, S. Stack, P. Kowalski, D.S. Cornett, M. Park, *Procedings of the 43rd ASMS conference on Mass Spectrometry and Allied Topics*, Atlanta, GA (1995)

[13] Z. Jianru, M. Karas, F. Hillenkamp, *Procedings of the 43rd ASMS conference on Mass Spectrometry and Allied Topics*, Atlanta, GA (1995)

[14] M. Vestal, P. Juhasz, W. Hines S. Martin, *Procedings of the 46th ASMS conference on Mass Spectrometry and Allied Topics*, Orlando, FL (1998)

[15] P. Roepstorff and J. Fohlmann, *Biomed. Mass Spectrom.* **12** (1985) 631

[16] R.S. Johnson, S.A. Martin and K. Biemann, *Int. J. Mass Spectrom. Ion Processes* **86** (1988) 137

ION YIELD VS LASER FLUENCE

[1] M. Karas, D. Bachmann, U. Bahr and F. Hillenkmamp, *Int. J. Mass Spectrom. Ion Processes* **78** (1987) 53; Karas M, Hillenkamp F, *Anal. Chem.* **60** (1988) 2299

[2] K. Tanaka, H. Waki, Y. Ido, S. Akita and Y. Yoshida, *Rapid Commun. Mass Spectrom.* **2** (1988) 151

[3] W. Ens, Y. Mao, F. Mayer and K.G. Standing, *Rapid Commun. Mass Spectrom.* **5** (1991) 117

[4] K. Dreisewed, M. Schürenberg, M. Karas and F. Hillenkamp, *Int J. Mass Spectrom. Ion Processes* **141** (1995) 127

[5] R. Beavis, Organic Mass Spectrom. 27 (1992) 864

[6] W. Ens, M. Schürenberg and F. Hillenkamp, *Proc. 45th ASMS Conf.* (1997) 1099

[7] A. Krutchinsky, A. Loboda, V. Spicer, R. Dworschak, W. Ens and K.G. Standing, *Rapid Commun. Mass Spectrom.* **12** (1998) 508

[8] O. Vorm, P. Roepstorff, M. Mann, *Anal. Chem.* **66** (1994) 3281

IMAGE EVALUATION
TEST TARGET (QA-3)

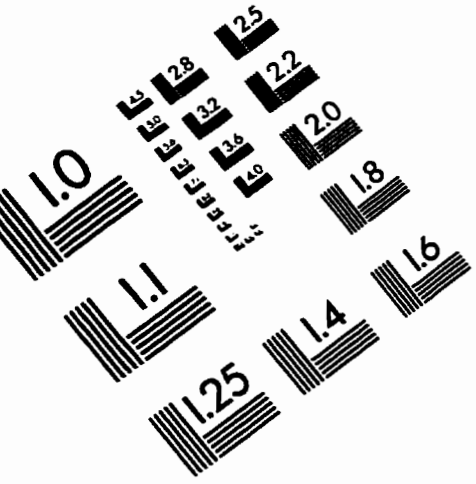

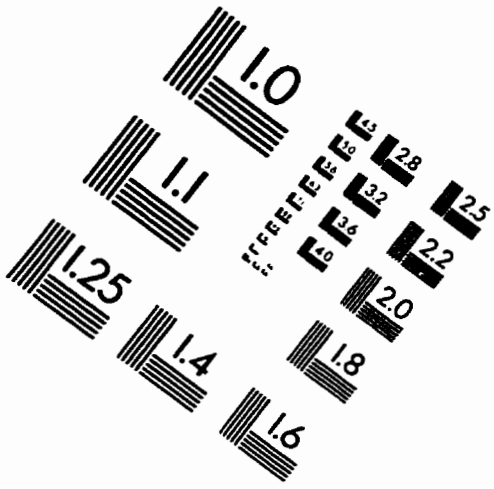

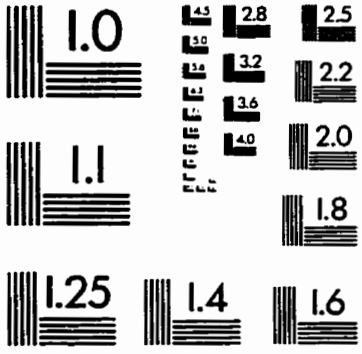

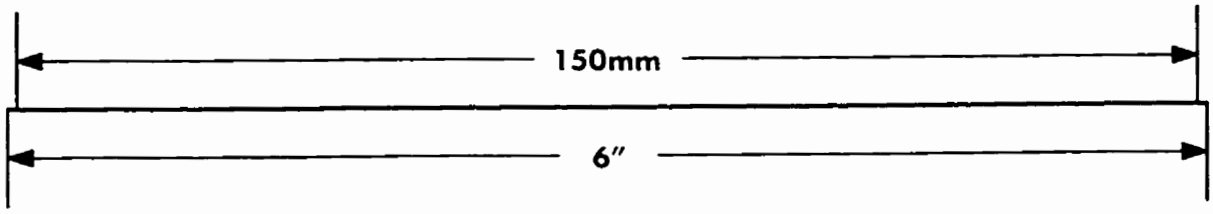

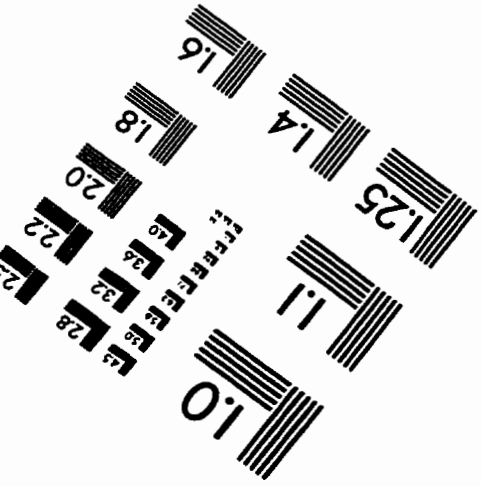

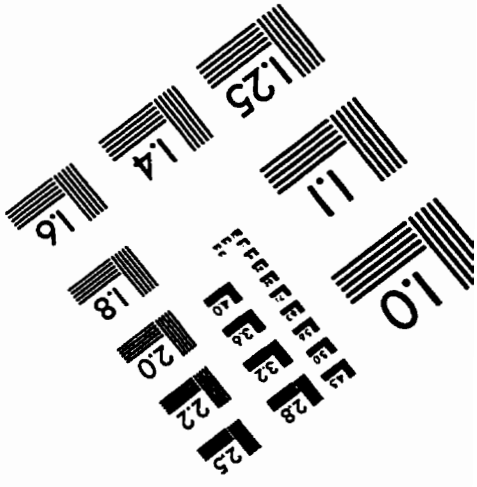

APPLIED IMAGE, Inc
1653 East Main Street
Rochester, NY 14609 USA
Phone: 716/482-0300
Fax: 716/288-5989